Title
Excitability of Sensory Cortex in Mouse Models of Fragile X Syndrome and Autism Spectrum Disorders

Author
Langberg, Tomer

Publication Date
2020

Peer reviewed|Thesis/dissertation

Excitability of Sensory Cortex in Mouse Models of Fragile X Syndrome and Autism Spectrum Disorders

By

Tomer Langberg

A dissertation submitted in partial satisfaction of the

requirements for the degree of

Doctor of Philosophy

in

Molecular and Cell Biology

in the

Graduate Division

of the

University of California, Berkeley

Committee in charge:

Professor Daniel E. Feldman, Chair
Assistant Professor Helen Bateup
Assistant Adjunct Professor Kristofer Bouchard
Professor Richard H. Kramer
Professor Frederic Theunissen

Spring 2020

Abstract

Excitability of Sensory Cortex in Mouse Models of Fragile X Syndrome and Autism Spectrum Disorders

by

Tomer Langberg

Doctor of Philosophy in Molecular and Cell Biology

University of California, Berkeley

Professor Daniel E. Feldman, Chair

Distinct genetic forms of autism are hypothesized to share a common increase in excitation inhibition (E-I) ratio in cerebral cortex, causing hyperexcitability and excess spiking. We provide a systematic test of this hypothesis across 4 mouse models ($Fmr1^{-/y}$, $Cntnap2^{-/-}$, $16p11.2^{del/+}$, $Tsc2^{+/-}$), focusing on somatosensory cortex. All mouse models with autism risk mutations showed reduced feedforward inhibition in layer 2/3 (L2/3) coupled with more modest, variable reductions in feedforward excitation, driving a common increase in E-I conductance ratio. Contrary to the classic, naïve prediction that increased E-I ratio drives spiking hyperexcitability, synaptic conductance modeling suggested that sensory inputs to this circuit would actually evoke stable or reduced firing in L2/3 *in vivo*. Indeed, spiking evoked by single whisker deflections was normal in the two strains whose modeling predicted stable synaptic depolarization ($Cntnap2^{-/-}$, $16p11.2^{del/+}$) and was reduced in the $Fmr1^{-/y}$ mice, also matching that strain's modeling prediction. In addition, spiking of putative inhibitory neurons was reduced in each strain. Thus, increased E-I ratio does not necessarily yield increased spiking responses to simple sensory stimuli.

Stable or reduced spiking was surprising given the dramatically reduced inhibition observed in each strain. Thus, we tested whether the $Fmr1^{-/y}$ mouse exhibits excess spiking in response to multi-whisker sequences, which drive more spiking in S1 compared to single-whisker deflections and may thus engage a different synaptic E-I ratio. Total spiking to whisker sequences, and cross-whisker suppression, were reduced in $Fmr1^{-/y}$ mice. These effects were explained by reduced firing to the anatomically corresponding columnar whisker and increased tuning heterogeneity within each cortical column. This suggests that weak or heterogeneous sensory maps may underlie circuit abnormalities in disorders expressing autism spectrum behaviors.

Table of Contents

Acknowledgements

Thank you, Dan, for your scientific mentorship. Thank you to my previous research mentors, Tom Sutula and Amar Sahay, for continuing to teach me, always supporting me, and best of all keeping in touch. And to Antoine, Nannan, and Kate who have also taught me so much and are simply the best. Thank you to Michelle and Phil, my teammates on the E-I project, and to the rest of the Feldman Lab. Thank you, Amanda, what can I say..an amazing person and friend. And Mr. Joe, the best labmate around and a dear friend. Thank you to my family for making life easy. And Maya and Ella, I love you.

Chapter 1

Introduction

Consequences of genetic mutations can emerge at the neural circuit level to cause neurodevelopmental disorders. But even disorders with known genetic etiology have an unknown neural circuit basis. Fragile X Syndrome, the most common form of intellectual disability, highlights this knowledge gap between genes and circuits (Hagerman et al., 2017). It is caused by silencing of a single gene with well-characterized molecular function, *Fragile X Mental Retardation 1* (*Fmr1*), yet still there is no agreement on its underlying neural circuit pathology. Fragile X Syndrome can also cause autism spectrum behaviors such as sensory hyperarousal and hyperactivity, in addition to seizures. These phenotypes have led to a search for whether *Fmr1* silencing and other genetic risk factors for autism spectrum disorders cause neural circuits to spike more.

This chapter provides background to the current theories of Fragile X Syndrome and Autism Spectrum Disorders pathophysiology, which motivate the experiments in Chapters 3 and 4.

Excitation and Inhibition in Cortex

Excitatory pyramidal neurons and inhibitory GABAergic neurons together form most synapses in the cortex. During typical conditions, the pyramidal neuron's membrane integrates hyperpolarizing synaptic inputs from GABAergic neurons and depolarizing inputs from pyramidal neurons and thalamocortical axons to produce action potentials, or spikes. These opposing inputs to single pyramidal neurons are often strongly coupled at the millisecond timescale across cortex. The probability of depolarizing to spike threshold in response to coupled excitatory and inhibitory synaptic inputs is dictated by their synaptic conductances, along with intrinsic membrane properties that can filter, suppress, or amplify changes in membrane potential. Weak synapses have a conductance closer to zero.

This coordination of synaptic excitation and inhibition is necessary for many cortical circuit computations (Isaacson & Scanziani 2011, Petersen & Crochet 2013). It

is thus not surprising that plasticity at excitatory and inhibitory synapses are co-dependent during neurodevelopment, often to the effect of stabilizing mean firing rates or changing sensory tuning (Hensch 2005, Maffei & Fontanini 2009, House et al., 2011, Vogels et al. 2011). Connectivity of neural circuits facilitates rapid recruitment of inhibition to counterbalance increases in excitation and prevent excess spiking (Pouille et al., 2009, Xue et al., 2014, Moore et al., 2018). Importantly, the developmental assembly of excitatory and inhibitory circuits is under extensive genetic control (eg., Hensch et al., 1998, Lin et al., 2008; and see Sohal & Rubenstein 2019).

It is well-appreciated that inhibition can shunt firing of pyramidal neurons (Fishell & Rudy 2011). Maximizing the firing of fast-spiking parvalbumin-expressing (PV) inhibitory neurons (40% of inhibitory neurons in cortex) through pharmacological or optogenetic manipulation readily eliminates spiking in pyramidal neurons by evoking a near-constant inhibitory conductance. Additional molecularly and physiologically distinct forms of inhibition exist, and each may each serve as a “control knob” for certain cognitive functions by inhibiting separate subcellular processes in pyramidal neurons (Hangya et al., 2014) (eg., dendritic integration [Spruston 2008, Higley 2014]).

Discovery of different inhibitory neuronal subtypes has helped uncover generalizable sets of synaptic connectivity motifs that form during neurodevelopment and perform unique functions (Harris & Mrsic-Flogel 2013, Tremblay et al., 2016). These motifs are repeated across cortical regions representing different sensory, motor, or otherwise cognitive domains. One prominent example is feedforward inhibition mediated by PV interneurons, which restricts spiking induced by afferent feedforward excitatory synapses. Failure for feedforward inhibition to counteract feedforward excitation can result in excess spiking in pyramidal neurons, commonly called *hyperexcitability*. Feedforward inhibition is the principle circuit motif that prevents hyperexcitability associated with seizures, and increasing feedforward inhibition (eg. by $GABA_AR$ agonism) is a common goal of anti-epileptic drugs (Paz & Huguenard 2015). Other motifs include feedback excitation and inhibition, and recurrent excitation (Harris & Mrsic-Flogel 2013).

Hyperexcitable Neural Circuits in Fragile X Syndrome and Autism Spectrum Disorders

Neurodevelopmental disorders such as autism, schizophrenia, and intellectual disability are commonly attributed to a dysfunction of synapses that drives abnormal spiking of neuronal populations in brain regions relevant to the disease phenotypes (Frankle et al., 2003, Bear et al., 2004, Bourgeron 2009). Inhibitory synapses in cortex have been of particular interest due to their functional diversity and control of pyramidal neuron excitability (Oscar Marin 2012), but the most prevailing hypothesis posits more particularly that the ratio of excitatory-to-inhibitory synaptic activity is the critical circuit pathology (Hussman 2001, Rubinstein & Merzenich 2003; for some alternative theories: Bear et al., 2004, Markram et al. 2007, Sinha et al., 2014). While some underlying genetic mutations directly affect expression of synaptic proteins, others would have pleiotropic or “emergent” effects on synapses due to cellular homeostasis (Ramocki & Zoghbi 2008, Nelson & Valakh 2015). Despite the pool of synaptic hypotheses having accumulated thousands of citations, we still do not really know how synapses are affected by gene dosage in neurodevelopmental disorders, how these synaptic changes

affect spiking, and how this change in excitability can explain the behavioral hallmarks of prevalent disorders such as Autism Spectrum Disorders (ASDs) and Fragile X Syndrome (FXS).

Impaired socialization is the largest contributor to the diagnosis and severity of ASDs, and begins to express alongside restricted or repetitive behaviors and interests in the 2nd year of life (American Psychiatric Association, 2013). 90% of ASD patients express abnormal sensory arousal, such as excessive fascination with a sound, indifference to pain or temperature, or adverse responses to innocuous textures (Robertson & Baron-Cohen 2017). ASDs are genetically diverse (Geschwind 2009). Fragile X Syndrome is the most common genetic cause of both ASDs and intellectual disability (Hagerman et al., 2017). Though still accounting for only 5% of ASDs, it is especially valuable for understanding the genetic basis for neural circuit dysfunction in autism since it is caused by silencing of only a single gene (Budimirovic & Kaufmann 2011). Sensory hyperarousal in FXS and increased seizure comorbidity (Lewine et al., 1999, Gilllberg & Billstedt 2000, Hagerman et al. 2017, Hagerman & Stafstrom 2009) in FXS and ASDs are the main evidence for the widely-held hypothesis that these are disorders of hyperexcitability. Still, we lack solid evidence for increased spiking or a clear causative synaptic dysfunction. The cat is still in the bag with this one.

The most common strategy to test for the presence of hyperexcitability and its potential underlying synaptic mechanism in FXS and ASDs is to record and manipulate neural activity in mice, which are commonly derived from transgenic lines with altered expression of single genes implicated in these disorders. The *Fmr1* KO mouse is the most prevalent of these models. While limited in translation, findings from transgenic mice have inspired a model where reduced inhibition drives increased spiking in cortex to cause aberrant disease-related behavior (Hussman 2001). In genetically-typical mice, manipulating synaptic activity to increase spiking in prefrontal cortex disrupts social behavior (Yizhar et al., 2011), increasing synaptic depolarization in somatosensory cortex enhances tactile sensitivity (Sachidhanandam et al., 2013), and inhibiting thalamocortical excitatory synaptic transmission prevents seizures (Paz et al., 2013). Still, evidence for increased spiking in *Fmr1 KO* mice is weak but has been found in the auditory system (Rotschafer & Razak 2013, Garcia-Pino et al. 2017).

Alternatively, reduced inhibition may cause behavioral phenotypes of FXS or ASDs without causing spiking hyperexcitability. Perhaps the strongest evidence for this is the finding that PV interneurons in sensory cortex of *Fmr1* KO mice are hypoactive *in vivo*, and that optogenetically boosting their firing rate can restore a deficit in sensory discrimination that is shared by human FXS patients (Goel et al., 2018). However, spike rates of excitatory neurons were normal in these mice, and the behavioral phenotype was instead attributed to changes in sensory tuning. This may be related to changes in synaptic excitation-to-inhibition ratio (Rubinstein & Merzenich 2003) which were not measured. This highlights the need for a more comprehensive study combining measurements of synaptic excitation and inhibition, spiking hyperexcitability and sensory tuning (eg., this thesis).

Rodent Whisker Somatosensory Cortex

That separate regions of cortex responsible for distinct cognitive and sensory domains share a common set of neural circuit motifs suggests that their neurodevelopment

shares genetic mechanisms. Thus, their circuits should also share some common deficits in response to gene dosage. The whisker region of the rodent somatosensory cortex (S1) is a particularly well-characterized cortical region and has greatly advanced knowledge of developmental plasticity, circuit function, and sensory encoding in general (Feldman & Brecht 2005, Feldmeyer et al., 2013).

Rodents have a stereotyped array of whiskers on each side of the snout that serve as tactile organs when they make active or passive contact onto surrounding objects. Touch signals from each individual whisker relay from the mystacial pad to the brain stem and thalamus. Co-tuned thalamocortical projection neurons then target anatomically clustered neurons in layer 4 of whisker S1. Together, clusters representing each whisker form a topographic map which is isomorphic to the position of whiskers on the mystacial pad. This topography is formed through activity-dependent genetic regulation during development (Inan & Crair 2007).

Feedforward excitation and inhibition propagate tactile information from thalamorecipient layer 4 neurons to superficial and finally deeper layers within radial "cortical columns" where most neurons primarily encode incoming touch from the column's anatomically corresponding whisker. Tactile inputs from different whiskers are synaptically-integrated within cortex through the aforementioned synaptic wiring motifs. Individual neurons often have synaptic responses to deflections of several individual whiskers, and typically fire spikes in response to a subset of those whisker deflections (Simons 1985, Moore & Nelson 1998, Zhu & Connors 1999). Tuning for multiple whiskers might emerge through cross-columnar synapses, or inputs from neurons within a shared column but with "mis-placed" sensory tuning (Clancy et al., 2015). The series of feedforward, feedback, and recurrent projections within a cortical column represents a macroscopic motif of many thousands of neurons that is repeated in different cortical regions. Thus, studying the activation of neurons across layers of a cortical column in response to whisker deflections can reveal broad principles of cortical excitability

At the cellular physiology level, whisker stimuli that evoke subthreshold or suprathreshold responses in a given neuron differ by the strengths and relative timing of the excitatory and inhibitory synaptic conductances they evoke (Moore & Nelson 1998, Wilent & Contreras 2005). The strength of synapses encoding whisker deflections in mature circuits is likely set through long-term depression and long-term potentiation during the critical period of plasticity in neurodevelopment (Crair & Malenka 1995, Feldman et al., 1998, Feldman 2000). Whisker stimuli evoking stronger depolarizing currents evoke more spikes (Zhu & Connors 1998), as do stimuli that evoke a longer time delay between excitatory and inhibitory conductances (longer integration window) (Wilent & Contreras 2005). Neurons with higher spontaneous firing or intrinsic excitability also fire more to sensory inputs (Zhu & Connors 1998). It is in these ways that changes to synaptic excitation and inhibition or intrinsic membrane excitability can cause hyperexcitability or altered tuning to sensory inputs.

This thesis will examine if and how changes to synaptic excitation and inhibition lead to excess spiking in S1 of mouse models of Fragile X Syndrome and Autism Spectrum Disorders. Chapter 2 is a response to published research which will expand our understanding of synaptic excitation and inhibition. Chapter 3 will directly test whether changes to synaptic excitation to inhibition cause excess spiking to deflections

of single whiskers in several autism mouse models. Chapter 4 will test whether excess spiking occurs in the *Fmr1 KO* mouse under different sensory conditions. Finally, in Chapter 5, we will draw some conclusions.

References

Bear, M. F., Huber, K. M., & Warren, S. T. (2004). The mGluR theory of fragile X mental retardation. *Trends in neurosciences*, *27*(7), 370-377.

Bourgeron, T. (2009). A synaptic trek to autism. *Current opinion in neurobiology*, *19*(2), 231-234.

Budimirovic, D. B., & Kaufmann, W. E. (2011). What can we learn about autism from studying fragile X syndrome?. *Developmental neuroscience*, *33*(5), 379-394.

Clancy, K. B., Schnepel, P., Rao, A. T., & Feldman, D. E. (2015). Structure of a single whisker representation in layer 2 of mouse somatosensory cortex. *Journal of Neuroscience*, *35*(9), 3946-3958.

Crair, M. C., & Malenka, R. C. (1995). A critical period for long-term potentiation at thalamocortical synapses. *Nature*, *375*(6529), 325-328.

Edition, F. (2013). Diagnostic and statistical manual of mental disorders. *Am Psychiatric Assoc*.

Feldman, D. E. (2000). Timing-based LTP and LTD at vertical inputs to layer II/III pyramidal cells in rat barrel cortex. *Neuron*, *27*(1), 45-56.

Feldman, D. E., & Brecht, M. (2005). Map plasticity in somatosensory cortex. *Science*, *310*(5749), 810-815.

Feldman, D. E., Nicoll, R. A., Malenka, R. C., & Isaac, J. T. (1998). Long-term depression at thalamocortical synapses in developing rat somatosensory cortex. *Neuron*, *21*(2), 347-357.

Feldmeyer, D., Brecht, M., Helmchen, F., Petersen, C. C., Poulet, J. F., Staiger, J. F., ... & Schwarz, C. (2013). Barrel cortex function. *Progress in neurobiology*, *103*, 3-27.

Fishell, G., & Rudy, B. (2011). Mechanisms of inhibition within the telencephalon:“where the wild things are”. *Annual review of neuroscience*, *34*, 535-567.

Frankle, W. G., Lerma, J., & Laruelle, M. (2003). The synaptic hypothesis of schizophrenia. *Neuron*, *39*(2), 205-216.

Garcia-Pino, E., Gessele, N., & Koch, U. (2017). Enhanced excitatory connectivity and disturbed sound processing in the auditory brainstem of fragile X mice. *Journal of Neuroscience*, *37*(31), 7403-7419.

Geschwind, D. H. (2009). Advances in autism. *Annual review of medicine*, *60*, 367-380.

Gillberg and, C., & Billstedt, E. (2000). Autism and Asperger syndrome: coexistence with other clinical disorders. *Acta Psychiatrica Scandinavica*, *102*(5), 321-330.

Goel, A., Cantu, D. A., Guilfoyle, J., Chaudhari, G. R., Newadkar, A., Todisco, B., ... & Erickson, C. A. (2018). Impaired perceptual learning in a mouse model of Fragile X syndrome is mediated by parvalbumin neuron dysfunction and is reversible. *Nature neuroscience*, *21*(10), 1404-1411.

Hagerman, P. J., & Stafstrom, C. E. (2009). Origins of epilepsy in fragile X syndrome. *Epilepsy Currents*, *9*(4), 108-112.

Hagerman, R. J., Berry-Kravis, E., Hazlett, H. C., Bailey, D. B., Moine, H., Kooy, R. F., ... & Hagerman, P. J. (2017). Fragile X syndrome. *Nature reviews Disease primers*, *3*(1), 1-19.

Hangya, B., Pi, H. J., Kvitsiani, D., Ranade, S. P., & Kepecs, A. (2014). From circuit motifs to computations: mapping the behavioral repertoire of cortical interneurons. *Current opinion in neurobiology*, *26*, 117-124.

Harris, K. D., & Mrsic-Flogel, T. D. (2013). Cortical connectivity and sensory coding. *Nature*, *503*(7474), 51-58.

Hensch, T. K. (2005). Critical period plasticity in local cortical circuits. *Nature Reviews Neuroscience*, *6*(11), 877-888.

Hensch, T. K., Fagiolini, M., Mataga, N., Stryker, M. P., Baekkeskov, S., & Kash, S. F. (1998). Local GABA circuit control of experience-dependent plasticity in developing visual cortex. *Science*, *282*(5393), 1504-1508.

Higley, M. J. (2014). Localized GABAergic inhibition of dendritic Ca 2+ signalling. *Nature Reviews Neuroscience*, *15*(9), 567-572.

House, D. R., Elstrott, J., Koh, E., Chung, J., & Feldman, D. E. (2011). Parallel regulation of feedforward inhibition and excitation during whisker map plasticity. *Neuron*, *72*(5), 819-831.

Hussman, J. P. (2001). Suppressed GABAergic inhibition as a common factor in suspected etiologies of autism. *J Autism Dev Disord*, *31*(2), 247-248.

Inan, M., & Crair, M. C. (2007). Development of cortical maps: perspectives from the barrel cortex. *The Neuroscientist*, *13*(1), 49-61.

Isaacson, J. S., & Scanziani, M. (2011). How inhibition shapes cortical activity. *Neuron*, *72*(2), 231-243.

Lewine, J. D., Andrews, R., Chez, M., Patil, A. A., Devinsky, O., Smith, M., ... & Chong, B. (1999). Magnetoencephalographic patterns of epileptiform activity in children with regressive autism spectrum disorders. *Pediatrics*, *104*(3), 405-418.

Lin, Y., Bloodgood, B. L., Hauser, J. L., Lapan, A. D., Koon, A. C., Kim, T. K., ... & Greenberg, M. E. (2008). Activity-dependent regulation of inhibitory synapse development by Npas4. *Nature*, *455*(7217), 1198-1204.

Maffei, A., & Fontanini, A. (2009). Network homeostasis: a matter of coordination. *Current opinion in neurobiology*, *19*(2), 168-173.

Marín, O. (2012). Interneuron dysfunction in psychiatric disorders. *Nature Reviews Neuroscience*, *13*(2), 107-120.

Markram, H., Rinaldi, T., & Markram, K. (2007). The intense world syndrome-an alternative hypothesis for autism. *Frontiers in neuroscience*, *1*, 6.

Moore, C. I., & Nelson, S. B. (1998). Spatio-temporal subthreshold receptive fields in the vibrissa representation of rat primary somatosensory cortex. *Journal of Neurophysiology*, *80*(6), 2882-2892.

Moore, A. K., Weible, A. P., Balmer, T. S., Trussell, L. O., & Wehr, M. (2018). Rapid rebalancing of excitation and inhibition by cortical circuitry. *Neuron*, *97*(6), 1341-1355.

Nelson, S. B., & Valakh, V. (2015). Excitatory/inhibitory balance and circuit homeostasis in autism spectrum disorders. *Neuron*, *87*(4), 684-698.

Paz, J. T., Davidson, T. J., Frechette, E. S., Delord, B., Parada, I., Peng, K., ... & Huguenard, J. R. (2013). Closed-loop optogenetic control of thalamus as a tool for interrupting seizures after cortical injury. *Nature neuroscience*, *16*(1), 64.

Paz, J. T., & Huguenard, J. R. (2015). Microcircuits and their interactions in epilepsy: is the focus out of focus?. *Nature neuroscience*, *18*(3), 351.

Petersen, C. C., & Crochet, S. (2013). Synaptic computation and sensory processing in neocortical layer 2/3. *Neuron*, *78*(1), 28-48.

Pouille, F., Marin-Burgin, A., Adesnik, H., Atallah, B. V., & Scanziani, M. (2009). Input normalization by global feedforward inhibition expands cortical dynamic range. *Nature neuroscience*, *12*(12), 1577.

Ramocki, M. B., & Zoghbi, H. Y. (2008). Failure of neuronal homeostasis results in common neuropsychiatric phenotypes. *Nature*, *455*(7215), 912-918.

Robertson, C. E., & Baron-Cohen, S. (2017). Sensory perception in autism. *Nature Reviews Neuroscience*, *18*(11), 671.

Rotschafer, S., & Razak, K. (2013). Altered auditory processing in a mouse model of fragile X syndrome. *Brain research*, *1506*, 12-24.

Rubenstein, J. L. R., & Merzenich, M. M. (2003). Model of autism: increased ratio of excitation/inhibition in key neural systems. *Genes, Brain and Behavior*, *2*(5), 255-267.

Sachidhanandam, S., Sreenivasan, V., Kyriakatos, A., Kremer, Y., & Petersen, C. C. (2013). Membrane potential correlates of sensory perception in mouse barrel cortex. *Nature neuroscience*, *16*(11), 1671.

Simons, D. J. (1985). Temporal and spatial integration in the rat SI vibrissa cortex. *Journal of neurophysiology*, *54*(3), 615-635.

Sinha, P., Kjelgaard, M. M., Gandhi, T. K., Tsourides, K., Cardinaux, A. L., Pantazis, D., ... & Held, R. M. (2014). Autism as a disorder of prediction. *Proceedings of the National Academy of Sciences*, *111*(42), 15220-15225.

Sohal, V. S., & Rubenstein, J. L. (2019). Excitation-inhibition balance as a framework for investigating mechanisms in neuropsychiatric disorders. *Molecular psychiatry*, *24*(9), 1248-1257.

Spruston, N. (2008). Pyramidal neurons: dendritic structure and synaptic integration. *Nature Reviews Neuroscience*, *9*(3), 206-221.

Tremblay, R., Lee, S., & Rudy, B. (2016). GABAergic interneurons in the neocortex: from cellular properties to circuits. *Neuron*, *91*(2), 260-292.

Vogels, T. P., Sprekeler, H., Zenke, F., Clopath, C., & Gerstner, W. (2011). Inhibitory plasticity balances excitation and inhibition in sensory pathways and memory networks. *Science*, *334*(6062), 1569-1573.

Wilent, W. B., & Contreras, D. (2005). Dynamics of excitation and inhibition underlying stimulus selectivity in rat somatosensory cortex. *Nature neuroscience*, *8*(10), 1364-1370.

Xue, M., Atallah, B. V., & Scanziani, M. (2014). Equalizing excitation–inhibition ratios across visual cortical neurons. *Nature*, *511*(7511), 596-600.

Yizhar, O., Fenno, L. E., Prigge, M., Schneider, F., Davidson, T. J., O'shea, D. J., ... & Stehfest, K. (2011). Neocortical excitation/inhibition balance in information processing and social dysfunction. *Nature*, *477*(7363), 171-178.

Zhu, J. J., & Connors, B. W. (1999). Intrinsic firing patterns and whisker-evoked synaptic responses of neurons in the rat barrel cortex. *Journal of neurophysiology*, *81*(3), 1171-1183.

Chapter 2

Thalamic Bursts and Single Spikes Evoke Distinct Inhibitory States in the Primary Sensory Cortex

Tomer Langberg

The following is a copy of Langberg (2016). Thalamic Bursts and Single Spikes Evoke Distinct Inhibitory States in the Primary Sensory Cortex. *Journal of Neuroscience, 36(45)*, 11496-11497., a journal club written in response to Hu & Agmon (2016). While only tangentially related to later chapters, it is a hoot of an exercise of the themes brought up in the thesis introduction:

2.1 Main Text

Brain circuits must faithfully transform sensation into the precise firing of neurons in the cortex, several synapses downstream from the periphery. To ensure accurate perception, these circuits exploit the unique firing properties of each component neuronal population. Most sensory information is relayed to the thalamus, whose neurons respond to sensation with single action potentials but can also fire in high-frequency bursts. These thalamic bursts are enigmatic: they are more effective than single action potentials at evoking cortical spiking (Swadlow and Gusev, 2001) but do not occur during typical active sensation (Fanselow et al., 2001). Bursts and single spikes represent distinct functional states (Sherman, 2001), but we do not know whether they activate distinct downstream ensembles. This is important because it may determine how sensations are encoded and cortical plasticity is evoked across behavioral states.

If thalamic bursts and single spikes activate cortical circuits differently, they might do so by differentially activating cortical inhibitory neurons, which strongly control the recruitment of broader cortical circuits (Swadlow, 2003; Gabernet et al., 2005). In

addition to targeting excitatory cortical neurons, the thalamus provides monosynaptic inputs to fast-spiking (FS) and somatostatin-positive (SOM) inhibitory cortical neurons. These inhibitory subclasses have distinct synaptic and intrinsic properties, and participate in distinct microcircuits. In juveniles, single thalamic action potentials reliably evoke short-latency spikes in cortical FS neurons (Cruikshank et al., 2007), but rarely evoke spikes in SOM neurons (Gibson et al., 1999; Cruikshank et al., 2010). FS and SOM neurons exhibit depressing and facilitating postsynaptic responses, respectively, to repetitive input from local excitatory neurons (Reyes et al., 1998). It is thus reasonable that these neurons would exhibit distinct responses to thalamic bursts and single spikes, a subject not yet explored on the single-cell level.

Recently, Hu and Agmon (2016) examined the responses of different cortical neuronal subtypes to single thalamic spikes and bursts with high resolution by simultaneous whole-cell recording of a ventrobasal thalamic neuron with a downstream, monosynaptically connected somatosensory barrel cortex neuron in a slice. Their experiments were conducted in juvenile mouse brains, the age at which thalamic input strongly activates cortical FS, but not SOM, neurons. Cellular targeting was achieved by channelrhodopsin expression exclusively in the ventrobasal thalamus, fluorescently tagged SOM neurons, and waveform characterization of excitatory and FS cells. Strengthening earlier data from Gibson et al. (1999), single presynaptic thalamic action potentials evoked the highest amplitude and shortest latency EPSP in FS cells. The only SOM neuron successfully recorded had the least reliable unitary EPSPs.

How do the postsynaptic responses of these thalamorecipient classes compare when the presynaptic thalamic neuron is bursting rather than firing single spikes? Hu and Agmon (2016) induced bursting with current injection in single thalamic neurons and recorded the resulting EPSPs, which temporally summated to produce a burst EPSP (bEPSP), in each cortical neuron. FS neurons displayed a depressing bEPSP, mirroring their responses to high-frequency local excitation (Reyes et al., 1998). Excitatory cells exhibited a smooth, summating bEPSP without clear peaks corresponding to each presynaptic action potential. The SOM neuron responded with a facilitating bEPSP whose highest amplitude peak was typically the last. Thus, cortical SOM neurons can indeed respond reliably to thalamic input, but only during thalamic bursts.

Hu and Agmon (2016) corroborated these findings by whole-cell recording in barrel cortex while eliciting bursts in single presynaptic cells through minimal photostimulation of the thalamus. All FS neurons exhibited depressing bEPSPs, while SOM neurons had facilitating responses. They also observed that while the timing of initial spikes within a thalamic burst was consistent across trials, the timing of later spikes in a thalamic burst was more variable. This implied that SOM neurons should spike more for thalamic bursts than for single spikes, but the burst-induced spikes should have high temporal jitter. To test this, the authors depolarized the postsynaptic cells to just under spike threshold and assessed spikes elicited by thalamic bursts. They found that FS neurons primarily fired a single action potential during the initial bEPSP peak and that SOM neurons fired with variable latency during later peaks.

The results of the study by Hu and Agmon (2016) revealed unique responses of excitatory, FS, and SOM cortical neurons to thalamic input. Compared with single presynaptic spikes, thalamocortical bursts did not greatly increase the spiking of FS

neurons. Swadlow and Gusev (2001), however, found that bursts in vivo do increase spiking in FS neurons, but as a consequence of presynaptic quiescence preceding the bursts, a condition not analyzed by Hu and Agmon (2016).Excitingly, Hu and Agmon (2016) also revealed that bursts allow single thalamic neurons to drive cortical SOM neurons to spike. This suggests that bursting is the primary thalamic firing mode that recruits the cortical SOM network.

These findings have interesting implications for how short-term synaptic dynamics are specified. Short-term synaptic depression and facilitation are generally attributed to specializations that decrease or increase presynaptic release probability, respectively (Zucker and Regehr, 2002). The observation by Hu and Agmon (2016) that thalamic bursts elicited depression in FS cells and facilitation in SOM cells is identical to FS and SOM synaptic dynamics for unitary inputs from local excitatory neurons (Reyes et al., 1998; Beierlein et al., 2003). This argues that postsynaptic neuronal identity may instruct presynaptic dynamics in a similar way at both thalamic and cortical synapses, perhaps through retrograde signaling mechanisms unique to each postsynaptic cell type. Interestingly, a single thalamic axon branches to synapse onto both excitatory and FS cortical neurons (Gabernet et al., 2005), but these synapses exhibit distinct short-term dynamics (Hu and Agmon, 2016). This indicates that different presynaptic terminals of the same axon can function with distinct release properties. It further suggests that each thalamorecipient neuronal subtype communicates distinctly with the presynaptic axon terminals that provide its thalamic input without affecting terminals of the same axon that synapse onto other cell types. Further work should uncover whether a single thalamic axon can target both FS and SOM cortical neurons and whether these inhibitory neuronal subtypes instruct presynaptic release dynamics at their thalamic inputs.

The results of the study by Hu and Agmon (2016) provide important information about thalamocortical communication, but there are some limitations. While layer 4 is the primary recipient of sensory information from the thalamus, nearly all of the cells that Hu and Agmon (2016) recorded were in layer 5B. The extent to which data can be extrapolated to thalamorecipient layer 4 cells is unclear. Additionally, spiking in excitatory neurons was not evaluated. Their gradually sloping bEPSP combined with short-term depression in strong, FS-mediated feedforward inhibition, however, suggest that burst-induced firing of excitatory neurons is temporally variable like that of SOM cells. In this case, burst-induced spiking in excitatory neurons may not encode sensory input with temporal precision.

If bursting reduces temporal precision, how could it enhance sensory encoding? Nicolelis and Fanselow (2002) proposed that thalamic neurons are primed to encode sensory input 100 ms after bursts because deinactivation of low-threshold calcium currents during afterhyperpolarization increases postsynaptic excitability. Hu and Agmon (2016) speculate that thalamic bursting may also prime excitatory cortical neurons to encode upcoming sensory input, via the following two mechanisms: (1) depression of FS-mediated feedforward proximal inhibition, which increases the integration window of excitatory neurons; and (2) isolation of thalamic inputs by facilitated SOM-mediated distal inhibition. These short-term dynamics are specific to burst-activated synapses and would exclusively affect transmission arriving from the thalamus, and only after its neurons recover from afterhyperpolarization.

The experiments of Hu and Agmon (2016) also suggest a novel way that thalamocortical bursts might contribute to cortical plasticity. Disinhibition of excitatory cells, such as during burst-induced FS depression, is widely thought to promote the induction of long-term synaptic plasticity. Sensory deprivation increases the probability of thalamic bursts (Linden et al., 2009), which may contribute to deprivation-induced cortical plasticity by decreasing FS-mediated inhibition. Interestingly, major structural plasticity is evident in the neonatal cortex and the neonatal thalamus strongly activates cortical SOM neurons (Tuncdemir et al., 2016) and weakly recruits cortical FS neurons (Daw et al., 2007). Considering the postsynaptic dynamics in FS and SOM neurons observed by Hu and Agmon (2016) in juveniles, this suggests that the cortical population recruited by thalamic bursts in juveniles is similar to that recruited by single thalamic spikes in the highly plastic neonatal circuit.

The diversity of neuronal subtypes in the sensory cortex underlies a functionally dynamic circuit that is capable of registering precise sensations and modulating synaptic connections with experience. Hu and Agmon (2016) expand our knowledge of how thalamic states differentially target these neuronal classes. An interplay between thalamic bursts and single spikes is likely necessary to optimize sensory encoding and circuit flexibility. Future work should examine whether these firing patterns have distinct impacts on circuit function downstream of the thalamorecipient neurons and whether these differences impact sensory perception.

2.2 References

Beierlein M, Gibson JR, Connors BW (2003) Two dynamically distinct inhibitory networks in layer 4 of the neocortex. J Neurophysiol 90:2987–3000.

Cruikshank SJ, Lewis TJ, Connors BW (2007) Synaptic basisforintense thalamocortical activation of feedforward inhibitory cells in neocortex. Nat Neurosci 10:462–468.

Cruikshank SJ, Urabe H, Nurmikko AV, Connors BW (2010) Pathway-specific feedforward circuits between thalamus and neocortex revealed by selective optical stimulation of axons. Neuron 65:230 –245.

Daw MI, Ashby MC, Isaac JT (2007) Coordinated developmental recruitment of latent fast spiking interneurons in layer IV barrel cortex. Nat Neurosci 10:453–461.

Fanselow EE, Sameshima K, Baccala LA, Nicolelis MA (2001) Thalamic bursting in rats during different awake behavioral states. Proc Natl Acad Sci U S A 98:15330–15335.

Gabernet L, Jadhav SP, Feldman DE, Carandini M, Scanziani M (2005) Somatosensory integration controlled by dynamic thalamocortical feed-forward inhibition. Neuron 48:315–327.

Gibson JR, Beierlein M, Connors BW (1999) Two networks of electrically coupled inhibitory neurons in neocortex. Nature 402:75–79.

Hu H, Agmon A (2016) Differential excitation of distally versus proximally targeting cortical interneurons by unitary thalamocortical bursts. J Neurosci 36:6906 –6916.

Linden ML, Heynen AJ, Haslinger RH, Bear MF (2009) Thalamic activity that drives visual cortical plasticity. Nat Neurosci 12:390 –392.

Nicolelis MA, Fanselow EE (2002) Thalamocortical optimization of tactile processing according to behavioral state. Nat Neurosci 5:517–523.

Reyes A, Lujan R, Rozov A, Burnashev N, Somogyi P, Sakmann B (1998) Target-cell-specific facilitation and depression in neocortical circuits. Nat Neurosci 1:279–285.

Sherman SM (2001) Tonic and burst firing: dual modes of thalamocortical relay. Trends Neurosci 24:122–126.

Swadlow HA (2003) Fast-spike interneurons and feedforward inhibition in awake sensory neocortex. Cereb Cortex 13:25–32.

Swadlow HA, Gusev AG (2001) The impact of 'bursting' thalamic impulses at a neocortical synapse. Nat Neurosci 4:402–408.

Tuncdemir SN, Wamsley B, Stam FJ, Osakada F, Goulding M, Callaway EM, Rudy B, Fishell G (2016) Early somatostatin interneuron connectivity mediates the maturation of deep layer cortical circuits. Neuron 89:521–535.

Zucker RS, Regehr WG (2002) Short-term synaptic plasticity. Annu Rev Physiol 64: 355–405.

Chapter 3

Increased Excitation-Inhibition Ratio Stabilizes Synapse and Circuit Excitability in Four Autism Mouse Models

Michelle W. Antoine*, Tomer Langberg*, Philipp Schnepel*, Carl Shi+, Jessica Benson+, and Daniel E. Feldman
(Asterisks indicate equal co-first authorship, Plus-signs indicate equal contributing authorship)

The following is a copy of 'Antoine, M. W., Langberg, T., Schnepel, P., & Feldman, D. E. (2019). Increased excitation-inhibition ratio stabilizes synapse and circuit excitability in four autism mouse models. *Neuron*, *101*(4), 648-661.', except for the addition of two authors (CS, JB).

3.1 Summary

Distinct genetic forms of autism are hypothesized to share a common increase in excitation-inhibition (E-I) ratio in cerebral cortex, causing hyperexcitability and excess spiking. We provide a systematic test of this hypothesis across 4 mouse models ($Fmr1^{-/y}$, $Cntnap2^{-/-}$, $16p11.2^{del/+}$, $Tsc2^{+/-}$), focusing on somatosensory cortex. All autism mutants showed reduced feedforward inhibition in layer 2/3 coupled with more modest, variable reduction in feedforward excitation, driving a common increase in E-I conductance ratio. Despite this, feedforward spiking, synaptic depolarization, and spontaneous spiking were largely normal. Modeling revealed that E and I conductance changes in each mutant were quantitatively matched to yield stable, not increased, synaptic depolarization for cells near spike threshold. Correspondingly, whisker-evoked spiking was not increased in vivo despite detectably reduced inhibition. Thus, elevated E-I ratio is a common circuit phenotype but appears to reflect homeostatic stabilization of synaptic drive rather than driving network hyperexcitability in autism.

3.2 Introduction

Autism spectrum disorders (ASD) is a family of neurodevelopmental disorders characterized by social and communication deficits, restricted and repetitive behaviors or interests, and abnormal sensory responses (Geschwind 2009). ASD is highly genetically heterogeneous, with greater than 100 identified risk genes with diverse functions in transcriptional regulation, protein synthesis and degradation, synapse function, and synaptic plasticity. Whether genetically distinct forms of ASD share a common dysfunction at the neural circuit level remains unclear.

One long-standing model is that genetically distinct forms of ASD share a common increase in synaptic excitation to inhibition (E-I) ratio in cerebral cortex, which drives hyperexcitability, excess spiking, and increased noise in cortical circuits. This is hypothesized to cause the cognitive and behavioral symptoms of autism (Nelson and Valakh, 2015, Rubenstein and Merzenich, 2003). Prior synaptic physiology studies using transgenic mouse models of ASD provide mixed support for this E-I ratio hypothesis. Many report reduced inhibition (Chao et al., 2010; Gibson et al., 2008; Han et al., 2012; Liang et al., 2015; Mao et al., 2015; Wallace et al., 2012), often coupled with a smaller decrease in synaptic excitation. However, others report a greater decrease in excitation than inhibition (Dani et al., 2005, Delattre et al., 2013, Unichenko et al., 2018, Wood and Shepherd, 2010) or increased inhibition (Harrington et al., 2016, Tabuchi et al., 2007). Variation across studies in brain area, cell type, ASD genotype, and physiological methods complicates identification of common synaptic and local circuit defects in ASD.

Critically, whether increased E-I ratio yields hyperexcitable cortical networks in ASD remains unclear. From basic biophysics, increased E-I conductance ratio does not necessarily drive stronger synaptic depolarization or spike probability. Some ASD mouse models show increased pyramidal (PYR) firing rate in some cortical areas in vivo (Peixoto et al., 2016, Rotschafer and Razak, 2013, Zhang et al., 2014), but most show no or modest changes (Dolen et al., 2007, Goncalves et al., 2013, He et al., 2017, O'Donnell et al., 2017, Wallace et al., 2017) or even reduced PYR firing (Banerjee et al., 2016, Durand et al., 2012, Garcia- Junco-Clemente et al., 2013, Unichenko et al., 2018), even when inhibitory neuron spiking is reduced (Berzhanskaya et al., 2016; Goel et al., 2018). In humans, increased network excitability is suggested by increased seizure prevalence in some forms of ASD, but seizures only occur in a subset of patients and electroencephalogram (EEG) may be normal during ASD symptoms (Samra et al., 2017, Tuchman et al., 2010). Many ASD mouse mutants show clear behavioral phenotypes in the absence of spontaneous seizures or abnormal EEG (Dhamne et al., 2017, Goorden et al., 2007, Pen˜ agarikano et al., 2011). Thus, whether E-I ratio is systematically altered across genetically distinct forms of autism, and whether this drives excess spiking in cortical circuits, remain unclear. Optogenetic manipulations of E-I ratio and spiking in prefrontal cortex induce and ameliorate social behavioral deficits, but this doesn't mean that elevated E-I ratio or excess spiking is the endogenous cause of social impairment in ASD mice (Yizhar et al., 2011, Selimbeyoglu et al., 2017).

We tested for common circuit defects in somatosensory cortex (S1) of four genetically distinct, well-validated mouse models of ASD (Fmr1$^{-/y}$, Cntnap2$^{-/-}$,

16p11.2$^{del/+}$, Tsc2$^{+/-}$). S1 is a reasonable focus because tactile disturbances are common in ASD (Robertson and Baron-Cohen, 2017), and S1 excitatory and inhibitory circuits are well characterized. We studied the feedforward circuit from layer (L) 4 to L2/3 pyramidal (PYR) cells, which is the first step in intracortical sensory processing. L4-L2/3 feedforward excitation and inhibition are integrated by PYR cells to evoke sparse spiking. This feedforward inhibition is mediated by parvalbumin (PV) interneurons, which are implicated in ASD. We systematically tested each ASD mutant in vitro and in vivo for abnormal synaptic excitation and inhibition in L2/3 PYR cells, abnormal network spiking, and impaired sensory coding. Fmr1$^{-/y}$ mice have impaired inhibition in L4 (Gibson et al., 2008), and Cntnap2$^{-/-}$ mice have fewer PV interneurons (Vogt et al., 2018), but E-I ratio phenotypes in L2/3 are unknown in any of these mutants. Thus, these four mutants provide a strong test for general applicability of the E-I ratio hypothesis.

We found that all ASD mutants exhibited decreased inhibition and more weakly decreased excitation, yielding increased E-I conductance ratio. However, contrary to the E-I ratio hypothesis, synaptic conductance modeling showed that these E-I changes were quantitatively matched to preserve peak synaptic depolarization, not increase it. Accordingly, peak synaptic depolarization and spiking were remarkably normal in ASD mutants, in vivo and in vitro. Thus, increased E-I ratio appears to be a compensatory mechanism that stabilizes synaptic depolarization and spiking excitability, rather than causing circuit hyperexcitability, in these ASD genotypes.

3.3 Results

L4-L2/3 Synaptic Currents and E-I Conductance Ratio

We tested for abnormal synaptic currents in S1 slices from juvenile Fmr1$^{-/y}$, Cntnap2$^{-/-}$, 16p11.2 del/+ and Tsc2+/- mice and age-matched wild-type (WT) controls. We first measured L4- evoked feedforward excitatory and inhibitory currents (EPSCs and IPSCs) converging onto single L2/3 PYR cells (Figure 1A). EPSCs and IPSCs were separated in whole-cell voltage clamp by holding at -72 and 0 mV, the reversal potentials for excitation and GABA-A inhibition. L4-evoked IPSCs were blocked by NBQX and D-APV (to 2.7 ± 1.6% of control, n = 3 cells), and thus represent disynaptic feedforward inhibition. For each PYR cell, we found the minimum L4 stimulation intensity required to evoke a detectable EPSC, denoted Eθ, and measured input-output curves for EPSCs and IPSCs at 1.0–1.5 3 Eθ. For analysis, currents were integrated over 20 ms, matching the timescale of L2/3 sensory integration in vivo (McGuire et al., 2016). Stimulation at Eq generally evoked small EPSCs and IPSCs. Increasing stimulus intensity recruited disproportionately larger IPSCs, so that inhibition dominated at ≥1.2 x Eθ, as in prior studies (House et al., 2011). Example cells for all genotypes are shown in Figure 1B.

Fmr1-/y mutants had smaller EPSCs than Fmr1$^{+/y}$ WTs (Figure 1C; n = 17, 18 cells, p = 0.0001, two-factor ANOVA on log-transformed data). Mouse N's and ages for slice physiology measurements are in Table S1. IPSCs were also reduced strongly in Fmr1$^{-/y}$ mutants (p = 0.0001). E-I ratio, calculated as E/(E+I) in each PYR cell, was increased in Fmr1$^{-/y}$ mice, demonstrating that IPCSs were reduced

preferentially (p = 0.0001). E/(E+I) equals the fraction of excitatory to total synaptic conductance, and is termed E-I conductance ratio. Cntnap2$^{-/-}$ mutants showed a similar phenotype relative to Cntnap2$^{+/+}$ littermates, with even more prominent loss of inhibition (Figure 1D, n = 12, 12 cells, p = 0.0001). All individual cells are shown in Figure S1. Identical results were obtained when peak current amplitude was analyzed (Figure S2).

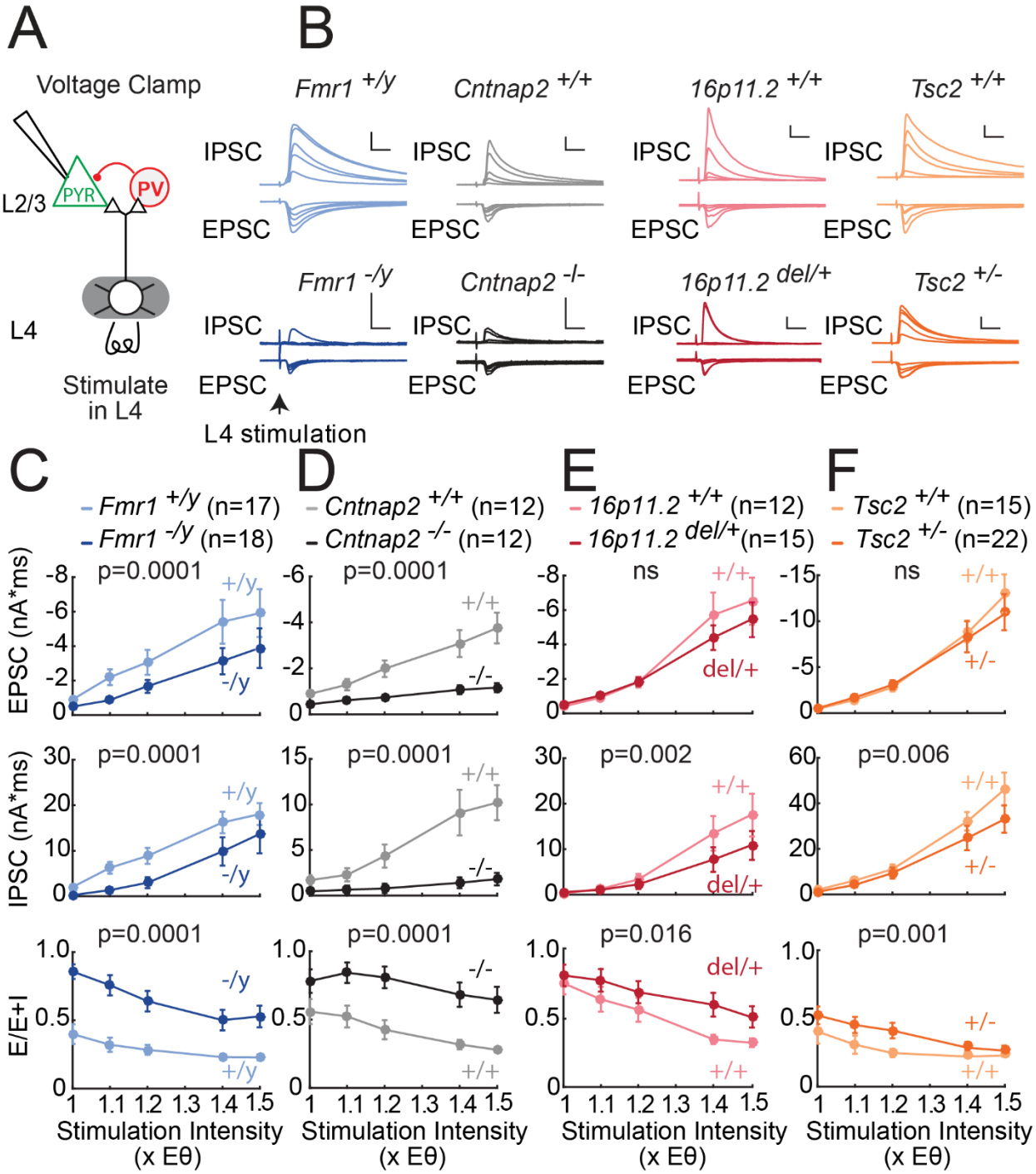

Figure 1. Deficits in Feedforward Excitatory and Inhibitory Synaptic Currents in L2/3 PYR Cells in Four ASD Mouse Lines (A) Experimental setup to measure L4-L2/3 feedforward EPSCs and IPSCs in S1 slices. (B) L4-evoked EPSCs and IPSCs at 1.0, 1.1, 1.2, 1.4, and 1.5 × Eθ from 8 example L2/3 PYR cells from ASD mutant mice and corresponding WTs. Scale bars, 10 ms, 500 pA. (C–F) Mean input-output curves for EPSCs (top), IPSCs (middle), and E-I conductance ratio calculated as E/(E+I) (bottom), for Fmr1 (C), Cntnap2 (D), 16p11.2 (E) and Tsc2 (F) genotypes. Plots show mean ± SEM across cells. P values are for genotype factor in a 2-way ANOVA on log-transformed data. N, number of cells.

16p11.2$^{del/+}$ and Tsc2$^{+/-}$ mice showed similar phenotypes, though more modest in magnitude (Figures 1E and 1F). IPSCs were reduced in both mutants (16p11.2$^{del/+}$ versus 16p11.2$^{+/+}$: n = 15, 12 cells, p = 0.002; Tsc2$^{+/-}$ versus Tsc2$^{+/+}$: n = 22, 15 cells, p = 0.006), but feedforward EPSCs were not significantly reduced (16p11.2; p = 0.36; Tsc2: p = 0.17). This led to modestly increased E-I conductance ratios for both mutants (16p11.2: p = 0.016, Tsc2: p = 0.001). Overall, in Fmr1$^{-/y}$, Cntnap2$^{-/-}$, 16p11.2$^{del/+}$ and Tsc2$^{+/-}$ mice, the area under the mean input-output curve for EPSCs was 0.57, 0.36, 0.86, and 0.92 of WT, respectively; for IPSCs it was 0.55, 0.18, 0.63, and 0.74 of WT; and for E-I ratio was 2.24, 1.79, 1.29, and 1.37 of WT. Mutant and WT PYR cells did not differ in baseline recording or stimulation parameters or in EPSC or IPSC kinetics including latency and EPSC-IPSC delay (Table S2; Figure S1). Thus, these 4 genetically distinct ASD mutants exhibited a common impairment in feedforward IPSCs, variably coupled to a loss of feedforward EPSCs, yielding a common increase in E-I conductance ratio. This result occurred despite strain differences in WT currents, which likely reflect genetic background effects.

Spontaneous miniature excitatory postsynaptic currents and miniature inhibitory postsynaptic currents (mEPSCs and mIPSCs) in L2/3 PYR cells also showed a preferential reduction in mIPSC activity compared to mEPSC activity, observed in 3 of the 4 ASD mutants (Figure S3). This suggests a broad reduction in inhibitory synapse number or function.

Spiking Excitability in the L2/3 Network

Does increased E-I ratio drive stronger synaptic responses and more spiking in L2/3, as commonly predicted from the E-I ratio hypothesis? To test this, we first measured spontaneous spiking in L2/3 PYR neurons in slices in a low-divalent Active Ringers solution, which promotes spontaneous network activity. Cell-attached recording was used to preserve the intracellular milieu. Many L2/3 PYR cells showed spontaneous firing, which was abolished by APV+NBQX (100 mM and 10 mM; n = 7 cells), showing it was driven by network synaptic activity (Figures 2A and 2B). We compared the distribution of L2/3 PYR firing rates in each mutant genotype versus corresponding WT (Figure 2C; n = 45-66 cells each). Surprisingly, Fmr1$^{-/y}$, 16p11.2$^{del/+}$, and Tsc2$^{+/-}$ mutants showed normal firing rates relative to WT, and only Cntnap2-/- showed excess spiking (p = 0.033, KS test).

To understand why firing rate was largely normal in ASD mutants, we measured L4-evoked postsynaptic potentials (PSPs) and spiking in L2/3 PYR neurons. Recordings were made from a baseline Vm of -50 mV (i.e., in the just subthreshold regime most

relevant to natural, synaptically evoked spiking). For each cell, we first determined Eq in voltage clamp, then switched to current clamp, depolarized to -50 ± 1.3 mV, and measured single-stimulus L4-evoked PSPs and spikes at 1.4 x Eθ. L4-evoked spiking was rare (6.9%of all sweeps, 25.4% of all cells), and PSPs were quantified from spike edited sweeps. Example L4-evoked PSPs are shown in Figure 2D. Strikingly, no mutant genotype showed a PSP peak (maximum depolarization) greater than WT (Figure 2E). Instead, PSP peak was unchanged from WT (Fmr1+/y versus Fmr1-/y: 5.3 ± 1.0 versus 3.6 ± 1.0 mV, n = 17, 11 cells, p = 0.31, Mann-Whitney test; Cntnap2s$^{+/+}$ versus Cntnap2$^{-/-}$: 5.5 ± 0.9 versus 4.0 ± 1.0 mV, n = 13, 13 cells, p = 0.15; 16p11.2$^{+/+}$ versus 16p11.2$^{del/+}$: 4.5 ± 1.0 versus 4.1 ± 0.7 mV, n = 13, 18 cells, p = 0.88; Tsc2$^{+/+}$ versus Tsc2$^{+/-}$: 4.1 ± 0.8 versus 5.4 ± 1.2 mV, n = 19, 10 cells, p = 0.07). The mean number of L4 evoked spikes was normal in ASD mutants, with only Tsc2$^{+/-}$ showing a non-significant trend for more spikes (Figure 2F; Table S3). The fraction of cells that exhibited L4-evoked spiking was also unchanged (Table S3). PSP duration was variably affected, increasing only in Tsc2+/- (p = 0.003, t test).

We applied L4 stimulus trains (5 pulses at 20 Hz) to test whether temporal summation is enhanced to drive stronger PSPs. The peak amplitude of each PSP (relative to pre-train baseline) was not altered in Fmr1$^{-/y}$, 16p11.2$^{del/+}$, or Tsc2$^{+/-}$, and it was actually weakened in Cntnap2$^{-/-}$ late in the train (2-way ANOVA, p = 0.0015). Thus, trains did not elicit excess synaptic depolarization (Figure S4). Train-evoked spiking was normal for Fmr1$^{-/y}$, Cntnap2$^{-/-}$, and 16p11.2$^{del/+}$, but it was increased in Tsc2$^{+/-}$ (Figure S4). Thus, despite strong preferential loss of L4-evoked IPSCs, L4-evoked synaptic depolarization was largely normal across ASD mutants, and modest increases in spontaneous network spiking (Cntnap2$^{-/-}$) or train-evoked spiking (Tsc2$^{+/-}$) were not caused by increased L4-L2/3 PSPs.

We also examined intrinsic excitability, which can be abnormal in some ASD models independent of synaptic phenotypes (Deng et al., 2013). L2/3 PYR cells showed normal passive properties at rest, including V_{rest}, R_{input}, membrane time constant (t_{mem}), and spike threshold and rheobase (Table S3). Intrinsic spiking excitability was variably affected across mutants, with no consistent phenotype (Figure S3).

Effects of Increased E-I Ratio Evaluated Using Synaptic Conductance Model

To understand how reduced inhibitory currents and increased E-I ratio could yield stable PSPs and evoked spiking, we modeled how L4-evoked excitatory and inhibitory synaptic conductances (G_{ex} and G_{in}) generate PSPs in L2/3 PYR cells. For each neuron in Figure 1, we converted the EPSC and IPSC measured at 1.4 x Eθ into G_{ex} and G_{in} waveforms, and then used a standard, passive parallel conductance model (Wehr and Zador, 2003) to predict the PSP that these conductances would elicit (Figures 3A and 3B). PSPs were modeled from a starting Vm of -50 mV to assess synaptic drive just below spike threshold. Model capacitance and resting conductance were from measured values for each genotype (Table S2). The model had no free parameters.

First, we evaluated whether, in the context of general weakening of synaptic conductances (Figure 1), the standard claim is true that a stable G_{ex}:G_{in} ratio preserves net synaptic depolarization (PSP peak), while increasing G_{ex}:G_{in} ratio increases PSP peak. Modeling showed this is incorrect. Instead, equal weakening of G_{ex} and G_{in}

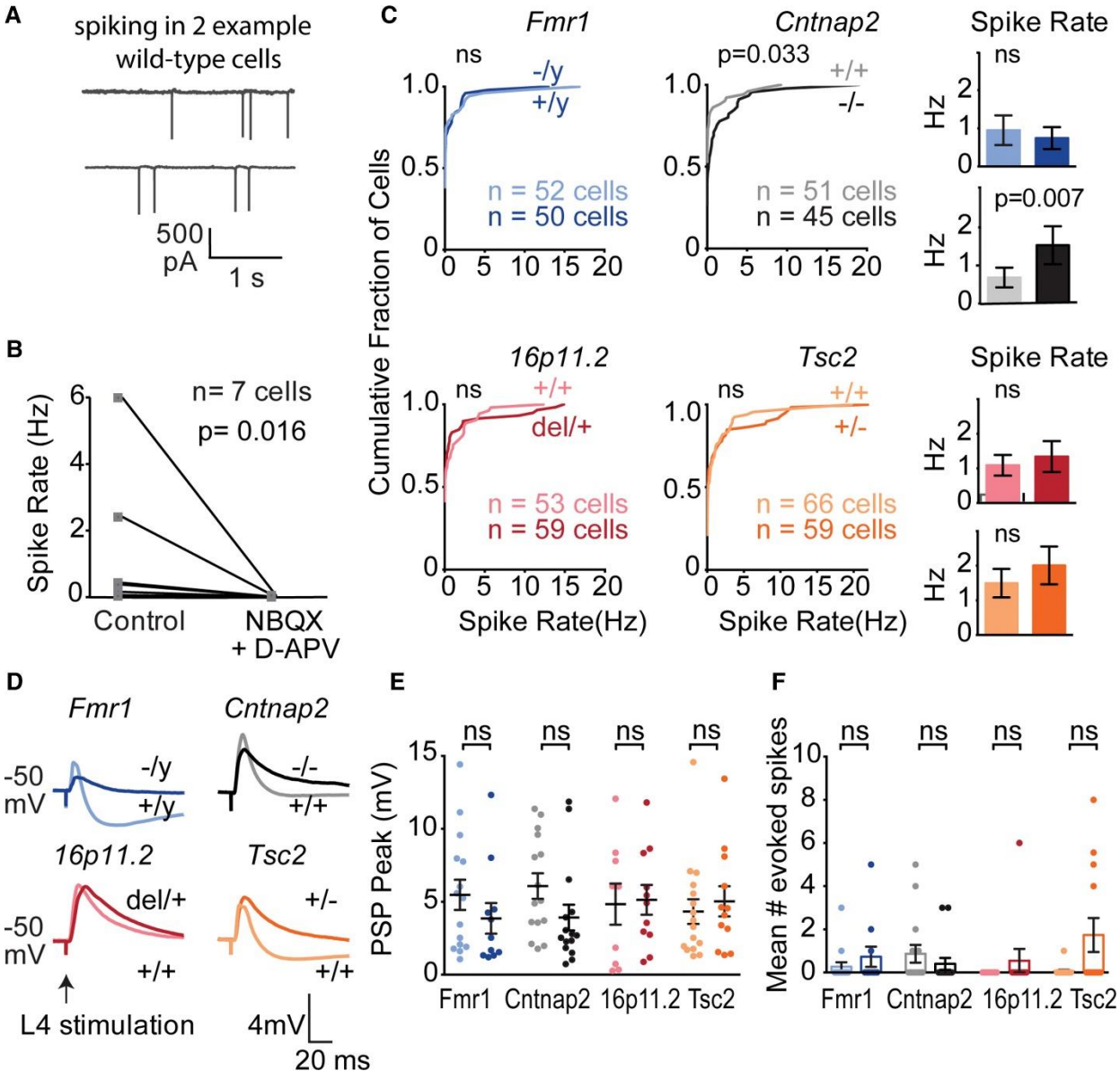

Figure 2. Spiking of L2/3 PYR Cells in S1 Slices (A) Spontaneous spiking in active Ringer's for two example L2/3 PYR cells in cell-attached mode. (B) Spontaneous spiking is abolished by glutamate blockers (n = 7 L2/3 PYR cells in 4 C57BL/6 mice). P value from Wilcoxon matched-pairs signed rank test. (C) Distribution of spontaneous firing rate in active slices in each genotype. Histograms show mean ± SEM of the same data. Differences in firing rate distributions and mean firing rate (histograms) were assessed by KS test and Mann-Whitney test, α = 0.05, respectively. (D) L4-evoked PSPs recorded in L2/3 PYR cells at 1.4 x Eθ from baseline Vm of −50 mV, with NMDA currents intact. One example cell from each genotype is shown. (E) L4-evoked PSP peak amplitude for all cells. Darker colors are ASD mutants. Each dot is one cell. Bars show mean ± SEM 10-19 cells per genotype. (F) Mean number of L4-evoked

spikes per sweep, per cell. Each dot is a cell. Bars show mean ± SEM. Significance in (E) and (F) was assessed by Mann-Whitney test, α = 0.05.

reduces PSP peak, and further weakening of G_{in} restores it (example cell, Figure 3C). The underlying principle is shown by a simulation in which we calculated the effect of differently scaled G_{ex} and G_{in} combinations on PSP peak for each Cntnap2 WT cell (Figure 3D). We predicted the PSP for each cell from its measured (unscaled) G_{ex} and Gin waveforms and for combinations of G_{ex} and G_{in} scaled by factors of [0, 0.1, 0.2, ... 1.2]. PSP peak for the unscaled G_{ex} and G_{in} combination was defined as $PSP_{unscaled}$. PSP peak for all scaled Gex and Gin combinations was expressed as $PSP_{diff} = PSP_{scaled} - PSP_{unscaled}$. Averaging across WT cells revealed a smooth contour of G_{ex}/G_{in} scaling combinations that predict no change in PSP peak ($PSP_{diff} = 0$), which we term the "PSP stability contour" (Figure 3D, thick contour). This contour is above the diagonal when overall synaptic conductance weakens, indicating that G_{in} must decrease more than G_{ex} to maintain a constant PSP peak. Intuitively, the preferential reduction of G_{in} on this contour depolarizes net synaptic reversal potential and increases driving force to precisely compensate for the loss in overall synaptic conductance.

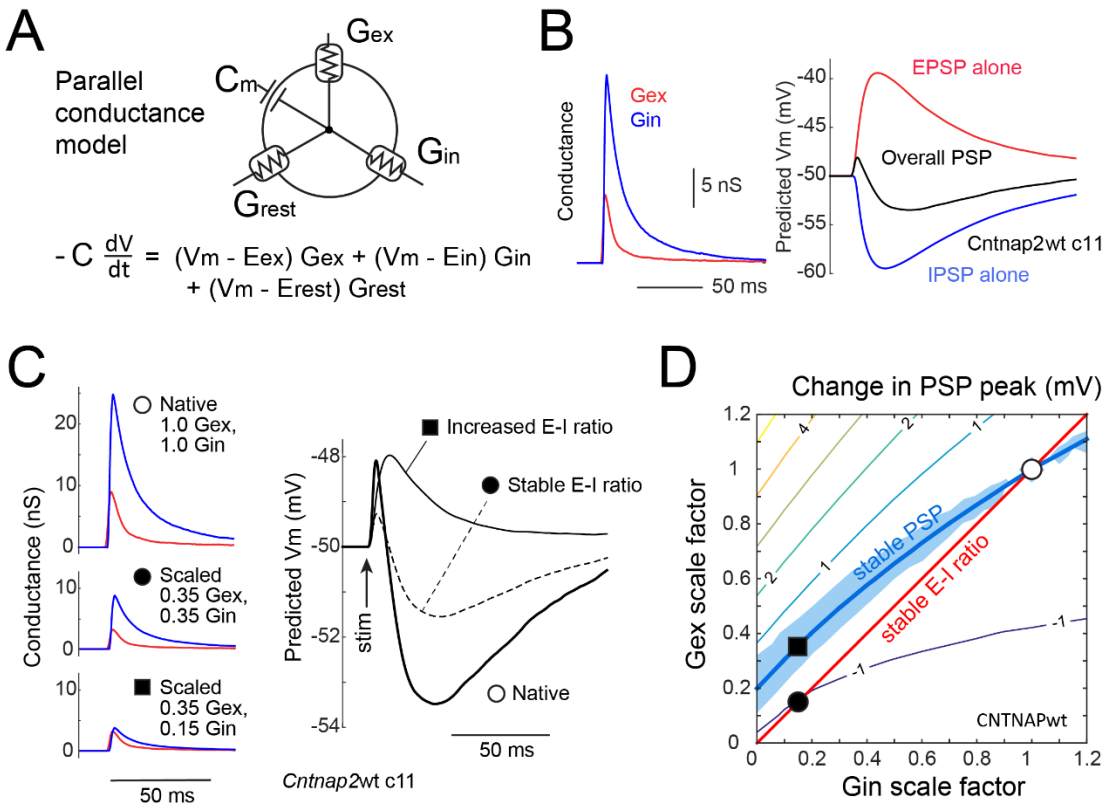

Figure 3. Relationship between E-I Conductance Ratio and PSP Peak for Cells near Spike Threshold (A) Schematic of parallel conductance model. (B) G_{ex} and G_{in} waveforms for an example WT cell, and predicted EPSP (from G_{ex} alone), IPSP (from G_{in} alone), and total PSP (from G_{ex} and G_{in} together) at baseline

V_m = −50 mV. (C) Conductance waveforms and predicted PSPs for one cell, for measured G_{ex} and G_{in} waveforms at 1.4 x Eθ (open circle), after equal scaling to 0.35 of original (•), and further reduction in G_{in} to 0.15 of original that increases E-I conductance ratio (■). (D) Contour plot of mean predicted change in overall PSP peak for different combinations of G_{ex} and G_{in} scaling, for all *Cntnap2*$^{+/+}$ cells. Thick contour shows G_{ex}/G_{in} combinations that predict no change in PSP peak (PSP_{diff} = 0) from unscaled G_{ex}/G_{in}. Blue region shows no significant change in PSP peak ($p > 0.05$, bootstrap). Positive contour values denote increased predicted PSP peak. Open circle is average G_{ex} and G_{in} in WT cells. • and ■ are from (C).

Next, we predicted PSPs from G_{ex} and G_{in} measured in ASD mutants. The mean EPSP peak predicted from G_{ex} alone was 2.0–4.3 mV smaller in ASD mutants than WTs (Figure 4A). This was significant in Cntnap2$^{-/-}$, Fmr1$^{-/y}$, and Tsc2$^{+/-}$ (2.4 ± 0.4, 6.3 ± 1.3, 13.3 ± 2.1 mV) versus WT (6.8 ± 1.2, 9.5 ± 1.8, 15.9 ± 1.7 mV, all $p < 0.037$, KS test), but was only a trend in 16p11.2$^{del/+}$ (9.0 ± 1.2 versus 11.0 ± 2.0 mV for WT). Similarly, the mean IPSP peak from G_{in} alone was predicted to be 1.9– 4.3 mV lower in ASD mutants (Figure 4A). This was significant in Cntnap2$^{-/-}$, Fmr1$^{-/y}$, and Tsc2$^{+/-}$ (1.1 ± 0.4, 4.6 ± 1.2, 8.6 ± 1.1 mV) relative to WTs (5.4 ± 1.0, 7.9 ± 0.8, 11.9 ± 0.8 mV, all $p < 0.024$ KS test) but was a trend in 16p11.2$^{del/+}$ (4.5 ± 1.0 versus 6.4 ± 1.2 mV, $p = 0.19$). Thus, reduced EPSCs and IPSCs in autism mutants predict smaller EPSPs and IPSPs near spike threshold. Combined G_{ex} and G_{in} waveforms generally predicted EPSP-IPSP sequences (Figure 4B). Peak of this overall PSP was identical between autism genotypes (Cntnap2$^{-/-}$ 1.6 ± 0.4 mV, Fmr1$^{-/y}$ 1.9 ± 0.3, 16p11.2$^{del/+}$ 4.1 ± 0.7, Tsc2$^{+/-}$ 3.7 ± 0.8) and WTs (Cntnap2$^{+/+}$1.5 ± 0.3, Fmr1$^{+/y}$ 2.1 ± 0.6, 16p11.2$^{+/+}$ 3.6 ± 0.5, Tsc2$^{+/+}$ 2.2 ± 0.4 mV, all $p > 0.1$, KS test). Across genotypes, the average difference in PSP peak was only 0.5 mV, even though the late IPSP was generally reduced (Figures 4A–4C). Thus, EPSP and IPSP reductions counteract one another to stabilize PSP peak. To test this idea more thoroughly, we determined the PSP stability contour at 1.4 x Eθ for WTs of each genotype. Then, we plotted the mean change in G_{ex} and G_{in} magnitude observed in mutants at 1.4 x Eθ (values from Figure 1, plotted as filled circles in Figure 4D). These points fell on or within 0.5 mV of the PSP stability contour from WTs. Thus, the reductions in G_{ex} and G_{in} in autism mutants are quantitatively matched to preserve synaptically-evoked peak ΔV_m, not to increase it.

We validated model predictions by recording L4-evoked PSPs in L2/3 PYR cells from -50 mV baseline V_m, this time with APV present to match conditions in the parallel conductance model, which lacks voltage-dependent NMDA currents. Stimulation was at 1.4 3 Eθ. Results were identical to the model predictions: PSP peak was unaffected, though the late IPSP was reduced in most mutants (Figures 4E, 4F, and S5). The only exception was a moderate but non-significant trend toward reduced PSP peak in Fmr1$^{-/y}$, replicating the model results (Figures 4E and 4F).

To extend these predictions over the physiological range of baseline V_m, we also modeled PSPs elicited from -70 mV. This model predicted weaker overall PSPs in mutants relative to WT for Cntnap2 and Fmr1 ($p < 0.027$, KS test) but not 16p11.2 and Tsc2. This is expected, because low driving force on inhibition at V_{rest} means that PSPs will track G_{ex}, which is reduced in Cntnap2 and Fmr1 (Figure S5). Overall, the observed increase in E-I conductance ratio in these 4 ASD mutants predicts

stable PSP amplitude for cells near spike threshold, and reduced PSP amplitude near V_{rest}. The only exception was a non-significant trend toward reduced, not increased, PSP amplitude in Fmr1$^{-/y}$ mice near spike threshold (Figures 4E and 4F).

L2/3 Network Activity and Sensory Coding In Vivo

The results above suggest that despite substantial loss of inhibition, L2/3 spike rate may be relatively unchanged or even reduced in vivo. To test this, we recorded single units with laminar polytrodes in L4 and L2/3 of S1 in adult urethane-anesthetized mice (P42-92, mean P62), and measured spiking in response to calibrated whisker deflections. We tested Cntnap2$^{-/-}$, Fmr1$^{-/y}$, and 16p11$^{del/+}$ mice and corresponding WTs (Figure 5). Recordings were made in C1-2 and D1-2 whisker columns, identified by post hoc histological staining or multiunit tuning in L4. We interleaved deflections of 9 single whiskers to map whisker receptive fields, plus deflections of the columnar whisker at multiple velocities tomeasure a velocity response curve (VRC) that parameterizes the gain and sensitivity of whisker-evoked spiking (Figures 5A and 5B). Individual units were classified as fast-spiking (FS; putative PV interneurons) or regular-spiking (RS; putative excitatory neurons) using a spike width criterion. This criterion was validated in separate experiments in which we recorded with the same electrodes in PV-Cre::ChR2 mice, and optogenetically identified spike waveforms of PV neurons from short-latency responses to blue laser flashes (Figure 5C).

We first tested whether reduced inhibition in L2/3 of ASD mutants was reflected in FS unit spiking. Spontaneous spiking of L2/3 FS units was significantly reduced in Fmr1$^{-/y}$ mice and showed non-significant trends toward reduction in other ASD mutants (Figure 5D) (bootstrapped median firing rate [Hz]: Fmr1$^{+/y}$ 0.76, Fmr1$^{-/y}$ 0.40, p = 0.04; Cntnap2$^{+/+}$ 0.99, Cntnap2$^{-/-}$ 0.77, p = 0.83; 16p11.2$^{+/+}$ 1.20, 16p11.2$^{del/+}$ 0.50, p = 0.08, permutation test). Mouse and unit N's are in Table S4. Whisker-evoked spiking of L2/3 FS units was measured in the VRC, which reflects feedforward activation of FS inhibitory circuits. For each genotype, population VRC data was fit with a sigmoid to quantify response threshold (the deflection velocity that evokes half-maximal response), sensitivity and maximal evoked firing rate (Figure 5E). All three ASD mutant genotypes showed significant decreases in whisker-evoked firing rate for L2/3 FS units (Figure 5E, dashed lines, p<<0.001, permutation test). This was also apparent in the median response across units (Figure 5E, solid lines), and in total whisker-evoked spikes across all velocities (median spike count: Fmr1$^{+/y}$ 36.03, Fmr1$^{-/y}$ 11.92, p = 0.002; Cntnap2$^{+/+}$ 102.72, Cntnap2$^{-/-}$ 33.04, p = 0.126; 16p11.2$^{+/+}$ 43.52, 16p11.2$^{del/+}$ 19.13, p = 0.05, permutation test). Response thresholds were not altered. This common reduction in whisker-evoked spiking of L2/3 FS neurons suggests that feedforward inhibition is reduced in vivo.

To test whether L2/3 PYR activity was abnormal, we analyzed L2/3 RS units. Spontaneous L2/3 RS spiking was normal in ASD mutants relative to WTs (Figure 6A; bootstrapped median [Hz]: Fmr1$^{+/y}$ 0.58, Fmr1$^{-/y}$ 0.32, p = 0.055; Cntnap2$^{+/+}$ 0.30, Cntnap2$^{-/-}$ 0.41, p = 0.17; 16p11.2$^{+/+}$ 0.50,16p11.2$^{del/+}$ 0.61, p = 0.85, permutation test). Whisker-evoked spiking across all units in the VRC was normal in Cntnap2$^{-/-}$ and 16p11.2$^{del/+}$ mice and was actually reduced in Fmr1$^{-/y}$ mice relative to WT (Figure 6B, p < 0.0001, t test). VRC response threshold was unchanged in ASD mutants (not shown). Total whisker-evoked spikes across the VRC was not altered in any ASD mutant

(median spike count: $Fmr1^{+/y}$ 20.14, $Fmr1^{-/y}$ 10.26, p = 0.12; $Cntnap2^{+/+}$ 11.27, $Cntnap2^{-/-}$ 12.09, p = 0.16; $16p11.2^{+/+}$ 25.44, $16p11.2^{del/+}$ 30.145, p = 0.85, permutation test). The fraction of L2/3 RS units that were whisker-responsive was also normal (Fmr1+/y 0.39, $Fmr1^{-/y}$ 0.53, p = 0.10; $Cntnap2^{+/+}$ 0.26, $Cntnap2^{-/-}$ 0.39, p = 0.24; $16p11.2^{+/+}$ 0.46, $16p11.2^{del/+}$ 0.59, p = 0.19, c2 test) (Figure 6C), as was the mean spiking response to each unit's preferred (best) whisker (Figure 6D). Thus, whisker-evoked population firing rate in L2/3 RS cells was normal, not elevated, in $Cntnap2^{-/-}$ and 16p11.2del/+ mice and was actually reduced in $Fmr1^{-/y}$ mice despite strongly reduced inhibition in these genotypes.

For one genotype (Fmr1), we verified the in vivo L2/3 RS spiking results in juveniles (P18-22). L2/3 RS units in Fmr1-/y mice (39 units, 4 mice) had normal spontaneous firing and reduced whisker-evoked spiking in the VRC relative to Fmr1+/y mice (37 units, 3 mice) (Figures 7A and 7B). Few L2/3 FS units were detected at this age. Thus, L2/3 RS spiking activity in Fmr1-/y is reduced both at P60 and P20.

Sensory Tuning and Firing Correlations

Inhibition regulates spike timing and sensory tuning, in addition to firing rate (Gabernet et al., 2005, Wehr and Zador, 2003). We tested whether L2/3 RS units in adult mice showed deficits in these sensory coding properties, which could add noise to circuits. We found essentially no deficits in spike latency (not shown), jitter (Figure 6E), or tuning sharpness (Figure 6F) in any ASD genotype. $Fmr1^{-/y}$ mice show spatially broader cortical activation to single-whisker stimulation, implying a blurred whisker map (Juczewski et al., 2016, Zhang et al., 2014). Consistent with map blurring, we found that the fraction of whisker-responsive L2/3 RS units that were tuned to the columnar whisker was lower in $Fmr1^{-/y}$ mice ($Fmr1^{+/y}$ 0.53, $Fmr1^{-/y}$ 0.24, p = 0.024, chi^2 test) (Figure 6G). This effect was also observed as a decrease in pairwise tuning similarity (signal correlation) between simultaneously recorded L2/3 RS neurons (Figure 6H). Neither $Cntnap2^{-/-}$ nor $16p11.2^{del/+}$ mutants shared these phenotypes. Thus, sensory tuning was remarkably normal in ASD mutants, except for a blurring of the whisker map in $Fmr1^{-/y}$.

Inhibition also regulates local cortical firing correlations, which can impact population coding. We calculated trial-by-trial spike count correlations (noise correlations) for pairs of simultaneously recorded L2/3 PYR cells (median 6 pairs per mouse) as well as raw firing synchrony, calculated as mean correlation at 0 ± 10 ms time lag from the spike cross-correlogram. Fmr1-/y mice showed significantly reduced noise correlations relative to $Fmr1^{+/y}$ controls, but $Cntnap2^{-/-}$ and $16p11.2^{del/+}$ showed no change (Figure 6I). $Fmr1^{-/y}$ and $Cntnap2^{-/-}$ mice showed a similar tendency for reduced firing synchrony versus WTs, but this was significant only for $Fmr1^{-/y}$ mice ($Fmr1^{+/y}$ versus $Fmr1^{-/y}$, p = 0.00027; $Cntnap2^{+/+}$ versus $Cntnap2^{-/-}$, p = 0.07; $16p11.2^{+/+}$ versus $16p11.2^{del/+}$, p = 0.49, permutation test) (Figure 6J). Thus, firing correlations were

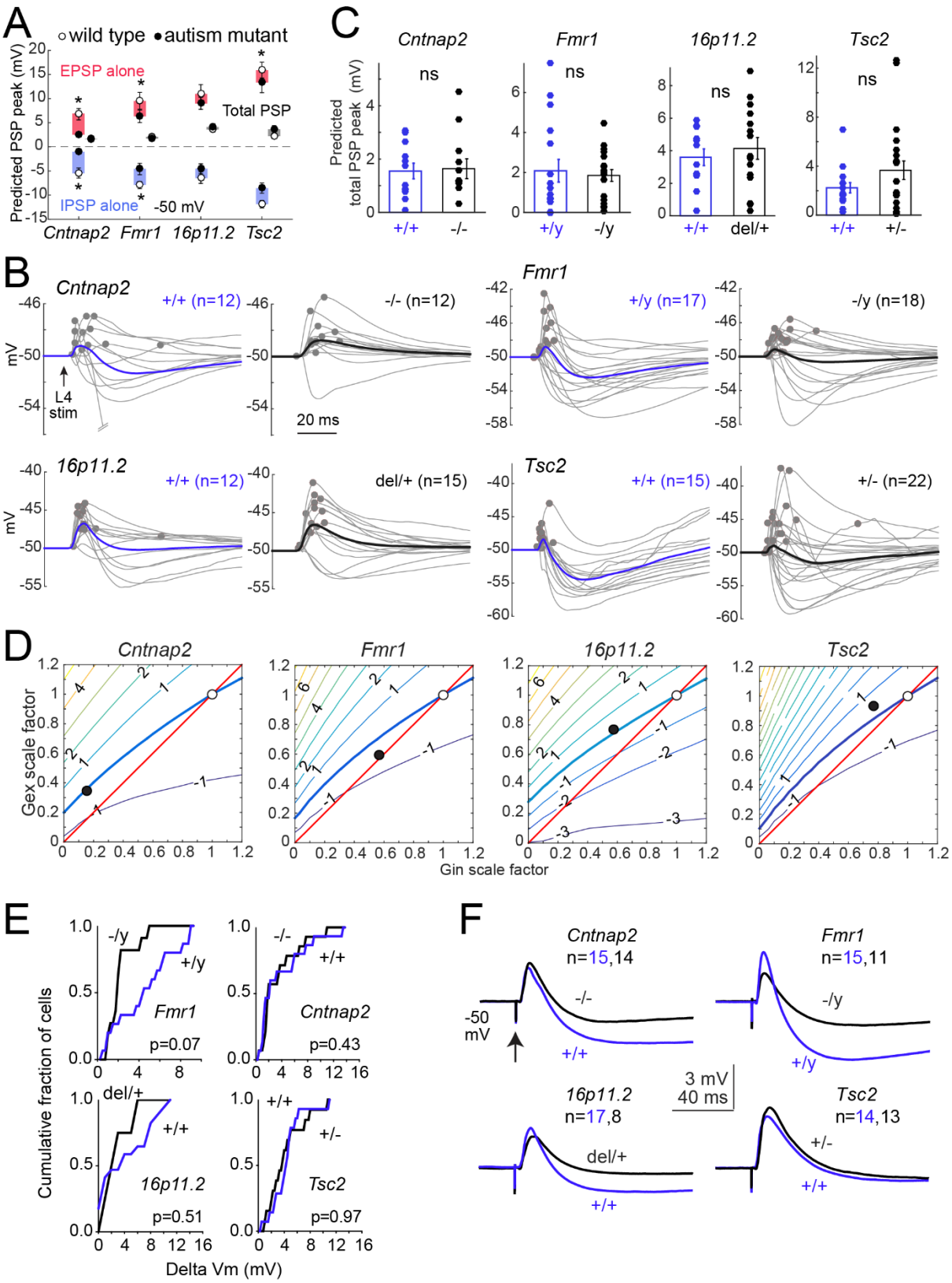

Figure 4. E-I Conductance Changes in ASD Mutants Predict Stable PSPs (A) Mean predicted EPSP, IPSP, and total PSP peak for each genotype at baseline

Vm = −50 mV, for Gex and Gin recorded at 1.4 × Eθ. Symbols are mean ± SEM across cells. N for each genotype is in (C). Stars, $p < 0.05$, KS test. (B) PSP waveforms predicted from the measured Gex and Gin in each WT and mutant cell. Dots show PSP peak. Bold, mean predicted PSP across cells. (C) Distribution of peak PSP for each genotype. Bars are mean ± SEM ns, not significant by KS test. (D) Contour plots show PSP stability contour (thick curve) for all WT cells of each genotype. ❍, average Gex and Gin of WT cells [(1,1) by definition]. •, average Gex and Gin measured in mutant cells, as fraction of WT. In all mutants, this lies within 0.5 mV of the PSP stability contour. (E) Cumulative histograms of measured L4-evoked PSP peak across cells in each genotype from baseline Vm of −50 mV, at 1.4 × Eθ, with APV in bath. There were no significant differences between any ASD mutant and its WT. Statistics are by KS test, α = 0.05. (F) Mean PSP waveforms for the experiment in (E).

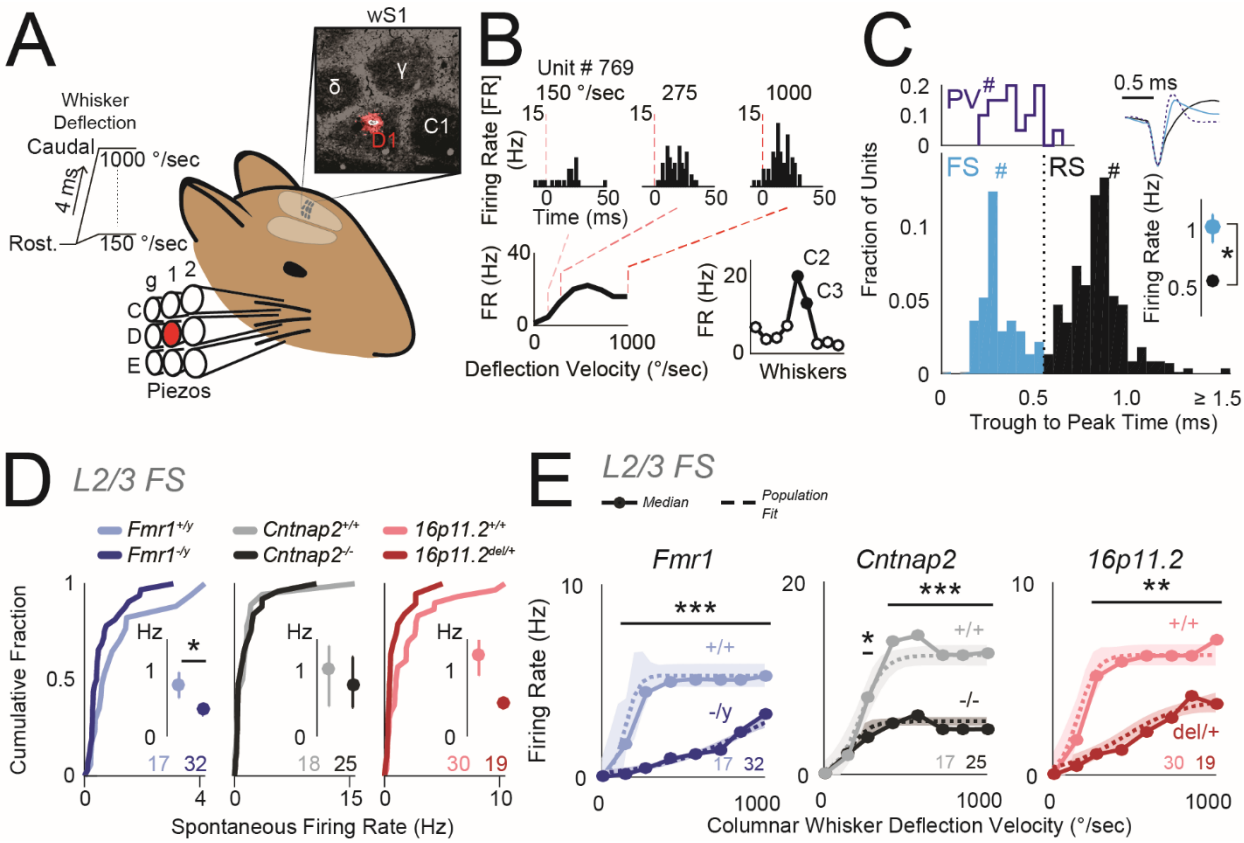

Figure 5. Reduced Columnar Whisker-Evoked Firing of Inhibitory FS Units in L2/3 *In Vivo* (A) Schematic for *in vivo* recording experiments. Deflections were delivered to 9 whiskers centered on the whisker corresponding to the recorded column in S1. Inset, D1 recording site localized by DiI labeling in cytochrome oxidase stained section of L4. (B) Example L2/3 unit recorded in the C2 column showing responses to columnar whisker deflections at 3 velocities. Bottom, Velocity response curve (VRC; left) and whisker tuning curve (right) for this unit.

Filled symbols, significant response. (C) Top left: trough-to-peak times for optogenetically-tagged PV neurons in PV-Cre::ChR2 mice. Bottom: trough-to-peak times for units from ASD mutant and WT mice. Dotted line, FS-RS threshold. Hashes mark the example waveforms (upper right). Right: bootstrapped median firing rate for FS and RS units. Error bars are 68% CI. n = FS: [285, 69] (units, mice), RS: [546,69]. $^{*}p < 0.001$, permutation test. (D) Spontaneous firing rate for L2/3 FS units, shown as cumulative distributions. Insets: bootstrapped medians. Error bars are 68% CI. Numbers are units per genotype. $^{*}p = 0.04$, permutation test. (E) Velocity response curves for the L2/3 FS unit population, calculated after subtraction of spontaneous rate for each unit. Circles: bootstrapped population median firing rate. Dashed curve is sigmoid fit to population data. Shaded region is 68% CI. Numbers are units per genotype. $^{*}p = 0.03$, $^{**}p \ll 0.001$, $^{***}p \ll 0.0001$, t test.

decreased or unchanged in ASD mutants.

Sensory-Evoked Spiking in L4

Sensory gain between L4 and L2/3 in vivo may parallel the functional strength of L4-L2/3 feedforward PSPs in vitro. To test this, we measured spiking of L4 RS units in vivo, typically recorded after L2/3 in the same penetrations. Spontaneous activity of L4 RS units was normal across all ASD mutant genotypes. Whisker-evoked spiking in the VRC for L4 RS units was normal for Fmr1-/y and 16p11.2del/+ mice (Figure S6). This suggests that the effective sensory gain between L4 and L2/3 was reduced in Fmr1-/y, and was normal in 16p11.2$^{del/+}$, matching the L4-L2/3 synaptic phenotypes in these mutants. Cntnap2-/- L4 RS units had abnormally low whisker-evoked spiking (Figure S6, $p < 0.007$, t test) suggesting that sensory gain between L4 and L2/3 was increased in Cntnap2$^{-/-}$, perhaps related to the increased network excitability observed in active slices (Figure 2).

Spiking In Vivo in L2/3 of Awake Fmr1 Mice

Finally, we tested for excess spiking of L2/3 RS units in awake mice, using the Fmr1 genotype, where excess S1 spikes have been reported under anesthesia (Zhang et al., 2014), but calcium imaging in awake mice suggests normal or even reduced whisker responses (He et al., 2017). We trained head-fixed Fmr1$^{-/y}$ and Fmr1$^{+/y}$ mice (n = 3 each) to perform a simple visual detection task while our standard whisker stimuli (defined above) were passively presented to individual whiskers every 0.2 s. Mice were task-engaged and licked for reward but did not whisk. We recorded single units using laminar polytrodes from C1-2 and D1-2 columns (n = 1–4 recording sessions and 10–32 L2/3 RS units per mouse). Spontaneous spiking of L2/3 RS units was unchanged between Fmr1$^{-/y}$ and Fmr1$^{+/y}$ mice (Figure 7C), but whisker-evoked spiking in the VRC was reduced (Figure 7D). The fraction of whisker-responsive units and tuning sharpness were normal (Figures 7E and 7F). These results closely mirror the findings in anesthetized mice and show that excess spiking was not observed among L2/3 RS units in awake Fmr1$^{-/y}$ mice.

3.4 Discussion

Common Increase in E-I Conductance Ratio

Despite its prominence, systematic tests of the E-I ratio hypothesis across different genetic forms of ASD are lacking. We provide a broad test in 4 genetically distinct ASD

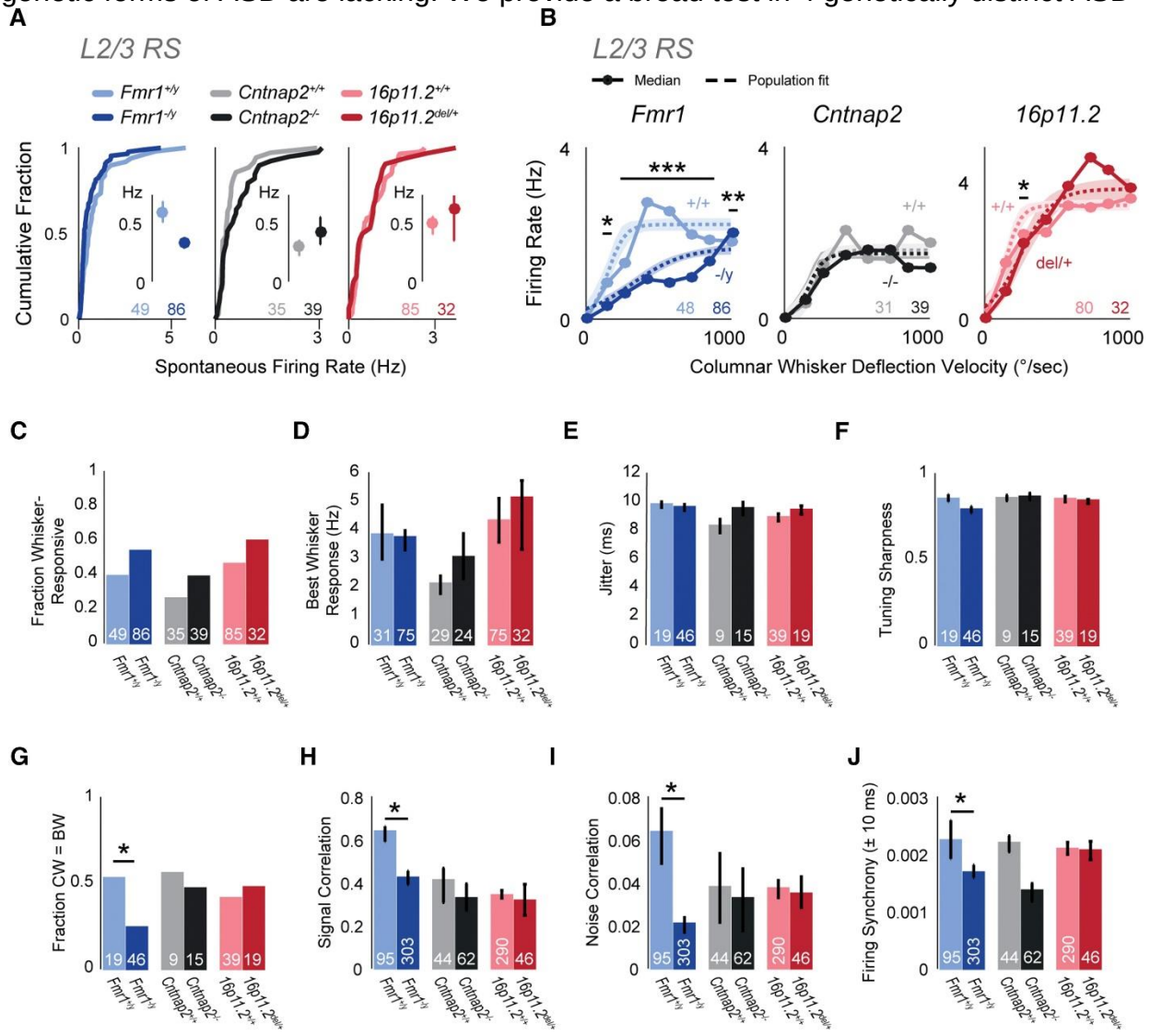

Figure 6. Firing of Excitatory L2/3 RS Units *In Vivo* Is Largely Normal in Autism Mutants (A) Spontaneous firing rate for L2/3 RS units, shown as cumulative distributions. Insets: bootstrapped medians with 68% CI. In all panels, numbers are units per genotype. (B) Velocity response curves for the L2/3 RS unit population, calculated after subtraction of spontaneous rate for each unit. Circles: bootstrapped population median. Dashed curve: sigmoid fit to population data. Shaded region is 68% CI. *p = 0.01, **p = 0.001, ***p ≪ 0.0001, t test. (C) Fraction of units that are whisker-responsive in each genotype. (D) Magnitude of best whisker-evoked response (bootstrapped median with nonparametric 68% CI). (E) Mean spike jitter for whisker-evoked responses, for whisker-responsive units. Bars are SEM. (F) Tuning sharpness of whisker-responsive units. Bars, bootstrapped

median. Error bars, 68% CI. (G) Fraction of whisker-responsive units whose best whisker (BW) is the columnar whisker (CW). *p = 0.0243, χ^2 test. (H) Signal correlation for pairs of L2/3 RS neurons. Bars, bootstrapped median. Error bars: 68% CI. *p < <0.0001, permutation test. N is cell pairs per genotype. (I) Noise correlation for pairs of L2/3 RS neurons. Bars, bootstrapped median. Error bars: 68% CI. *p = 0.0005, permutation test. (J) Raw firing synchrony for pairs of L2/3 RS neurons, calculated as mean over ± 10 ms in the cross-correlogram. Bars, bootstrapped median. Error bars: 68% CI. *p = 0.00027, permutation test.

models. We found a common phenotype of decreased L4-L2/3 feedforward inhibition and a smaller, variable decrease in feedforward excitation, yielding a common decrease in total synaptic conductance and increase in E-I conductance ratio in L2/3 PYR cells. mIPSCs were also generally reduced more than mEPSCs, suggesting a broad circuit phenotype of reduced inhibition. MeCP2-/y mice exhibit a qualitatively similar combination of strongly reduced inhibition and more modestly reduced excitation in L2/3 of visual cortex (Banerjee et al., 2016), and Ube3a$^{m-/+}$ have a similar phenotype (Wallace et al., 2012). Thus, at least 5, possibly 6 well-validated ASD mouse models share a similar loss of total synaptic conductance, loss of inhibition and increase in E-I conductance ratio in L2/3 of sensory cortex.

These results extend prior findings of reduced inhibition in Fmr1-/y mice from L4 (Gibson et al., 2008) to L2/3 and in Cntnap2-/- from hippocampus (Jurgensen and Castillo, 2015) to neocortex. It is also consistent with reduced inhibitory neuron number and PV expression in Fmr1-/y and Cntnap2-/- (Pen˜ agarikano et al., 2011, Selby et al., 2007, Vogt et al., 2018).

Synaptic Responses and Network Spiking Excitability Are Largely Preserved

Elevated E-I ratio did not cause excess synaptic depolarization or spiking in L2/3 PYR cells, contrary to the standard E-I ratio hypothesis. Single L4 stimuli evoked normal-magnitude PSPs from just-subthreshold Vm in all mutants. Responses to trains were also remarkably normal, except Cntnap2-/- where PSPs were reduced. Spiking to single L4 stimuli was normal in all mutants, and 3 of 4 mutant genotypes had normal spontaneous firing in active slices. In vivo, all 3 ASD mutants tested showed reduced whisker-evoked spiking of L2/3 FS units, consistent with reduced feedforward inhibition. However, spiking of L2/3 RS (presumed excitatory) units was normal in Cntnap2-/- and 16p11.2del/+ mice and was reduced in Fmr1-/y mice. Thus, increased E-I ratio in the L4-L2/3 projection was associated with remarkably normal evoked synaptic responses and spiking in L2/3 PYR cells, and even with reduced spiking in Fmr1-/y. Only Cntnap2-/- and Tsc+/- mutants showed any hint of increased spiking excitability, but this was not associated with altered feedforward synaptic depolarization.

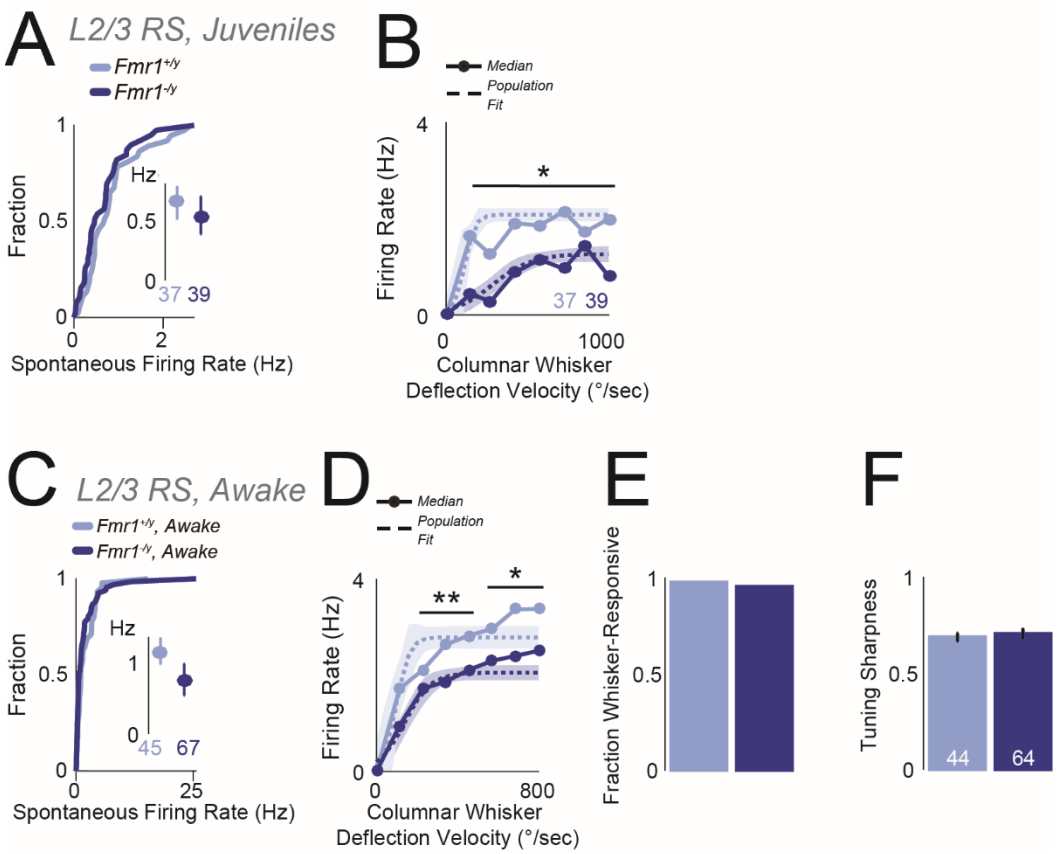

Figure 7. Firing of Excitatory L2/3 RS Units Is Reduced in Anesthetized Juvenile Mice and Awake Adult *Fmr1*$^{-/y}$ Mice (A) Spontaneous firing rate for L2/3 RS units in juvenile *Fmr1*$^{-/y}$ mice. Conventions as in Figure 6A. (B) Velocity response curves for juvenile *Fmr1*$^{+/y}$ and *Fmr1*$^{-/y}$ mice. Conventions as in Figure 6B. $^{*}p \ll 0.001$, t test. (C) Spontaneous firing rate of L2/3 RS units in awake, adult mice. Conventions as in (A). (D) Velocity response curves for the L2/3 RS unit population in awake, adult mice. Conventions as in (B). $^{*}p = 0.003$. $^{**}p < 0.003$, t test. (E) Fraction of L2/3 RS units that were whisker-responsive in awake, adult mice. (F) Tuning sharpness of whisker-responsive units.

Many prior in vivo studies in ASD mutants also show normal or reduced PYR firing rates. Spontaneous firing rate is normal in L2/3 of S1 and V1 in Fmr1-/y, Cntnap2-/-, Pten-/-, and Ube3a$^{m-/p+}$ mice (Garcia-Junco-Clemente et al., 2013, O'Donnell et al., 2017, Penagarikano et al., 2011, Wallace et al., 2017) and reduced in V1 of MeCP2$^{-/y}$ mice (Durand et al., 2012). Sensory-evoked spike rate and population activity are normal in L2-4 of S1 and V1 in Fmr1$^{-/y}$ and Ube3a$^{m-/p+}$ (Dolen et al., 2007, Berzhanskaya et al., 2016, He et al., 2017, Wallace et al., 2017; Goel et al., 2018), reduced in L2/3 of V1 in MeCP2$^{-/y}$ and Pten$^{-/-}$ (Banerjee et al., 2016, Durand et al., 2012, Garcia-Junco-Clemente et al., 2013) and slightly reduced in S1 in Nlgn4$^{-/-}$ mice (Unichenko et al., 2018). Increased sensory-evoked spiking has been observed in a small sample of hindpaw S1 neurons (Zhang et al., 2014) and in some studies in

auditory cortex (Rotschafer and Razak, 2013), all in Fmr1$^{-/y}$. Thus, increased cortical spiking is not broadly observed in ASD genotypes. Increased network excitability is instead usually suggested by subtler phenotypes, including elevated firing correlations and longer UP states in young Fmr1-/y mice (Goncalves et al., 2013, Hays et al., 2011, O'Donnell et al., 2017), increased intra-burst spike frequency in Shank3B$^{-/-}$ mice (Peixoto et al., 2016), and broader sensory tuning in MeCP2$^{-/y}$, Pten$^{-/-}$, Fmr1$^{-/y}$, and Ube3a$^{m-/p+}$ mice (Banerjee et al., 2016, Garcia-Junco-Clemente et al., 2013, Juczewski et al., 2016, Wallace et al., 2017; Goel et al., 2018). Fmr1$^{-/y}$ mice show faster or broader spread of sensory-evoked activity in S1, suggesting a blurred whisker map (Arnett et al., 2014; Zhang et al., 2014), which we also observed in the form of increased tuning heterogeneity in each S1 column.

E-I Ratio Is Coordinated to Stabilize Synaptic Responses near Spike Threshold

A simple synaptic conductance model explains why increased E-I conductance ratio does not generate stronger PSPs or more spiking in ASD mutants: in all 4 ASD genotypes, the decreases in inhibitory and excitatory conductances were precisely counterbalanced to maintain constant PSPs for V_m just below spike threshold. This V_m range is most relevant for naturally evoked spiking, as observed during active touch sequences in vivo (Yamashita et al., 2013). Because driving force is less for inhibition than excitation in this V_m range, the relatively large decrease in feedforward G_{in} (to 0.15–0.57 of WT, for the 4 ASD genotypes) and the smaller decrease in G_{ex} (to 0.35–0.92 of WT) predict equal, opposing reductions in IPSP and EPSP amplitude. Together, these preserve PSP peak in all 4 ASD mutants (Figure 4). Simulations defined a smooth contour of G_{in} and G_{ex} reductions that jointly stabilize feedforward PSP peak for just-subthreshold baseline V_m (Figure 4D). The mean G_{in} and G_{ex} reduction was close to this PSP stability contour in all 4 ASD mutants and predicted <0.5 mV change in PSP peak. Measurement confirmed that neither L4-evoked PSPs nor spikes were significantly increased in L2/3 PYR cells in ASD mutants despite the pronounced reduction in G_{ex} and G_{in} (Figure 4).

Thus, the common interpretation that increased E-I synaptic conductance ratio necessarily predicts increased spiking excitability in networks is incorrect. Instead, the specific increase in E-I conductance ratio offsets the decrease in total synaptic conductance in these 4 ASD genotypes to produce stable PSPs. Stable PSPs may also occur in MeCP2$_{-/y}$ mice, where visual-evoked G_{ex} and G_{in} are reduced to _0.60 and _0.45 of WT in L2/3 PYR cells (Banerjee et al., 2016), which is numerically similar to the 4 ASD mutants tested here. Thus, functionally matched changes in G_{ex} and G_{in} that alter E-I ratio but preserve PSP peak are a common theme across a diverse set of ASD genotypes.

These predictions do not account for active conductances, including NMDA receptors, shunting inhibition, or changes in $GABA_A$ reversal potential which occur in young Fmr1$_{-/y}$, MeCP2$_{-/y}$, and valproate models of ASD (Banerjee et al., 2016, He et al., 2014, Tyzio et al., 2014). Despite this, these predictions explain the largely stable firing rate in S1 in vivo and in active slices for 3 of 4 ASD mutants. Interestingly, Fmr1-/y was the only genotype to show a trend for weaker single feedforward PSPs in vitro (Figures 2 and 4), and this mouse also showed reduced whisker-evoked spiking in L2/3 in vivo (Figures 6 and 7). While the PSP peak remained stable in ASD mutants, the late IPSP

following the peak was generally weakened (Figure 4). This suggests that temporal summation may be altered under some circumstances, although responses to stimulus trains in S1 slices were again largely normal (Figure S4).

E-I Ratio and Synaptic Homeostasis in Autism

Our results show that an increased E-I conductance ratio is common across ASD genotypes but yields stable synaptic drive and largely stable spiking, at least in L2/3 of sensory cortex. How, then, is an elevated E-I ratio related to information processing deficits in ASD? Our results strongly suggest that E-I ratio changes are compensatory in autism (Nelson and Valakh, 2015). Both excitatory and inhibitory circuits exhibit robust homeostatic plasticity that adjusts E-I ratio to stabilize cortical firing rate (Gainey and Feldman, 2017, Turrigiano 2011). In S1, this E-I homeostasis is evident during brief whisker deprivation, which weakens L4-L2/3 inhibition more than excitation, increasing E-I ratio by a precise amount that maintains stable PSPs and spiking in L2/3 (Gainey et al., 2018, Li et al., 2014). This is virtually identical to the phenotype in ASD mutants (Figure S7). We propose that many ASD mutations alter cortical spiking activity, which secondarily engages E-I homeostasis to restore cortical firing rate. ASD symptoms may arise from imperfect homeostasis that largely normalizes firing rate but maladaptively compromises other aspects of population coding, like sensory tuning or firing synchrony (e.g., Goel et al., 2018; Gonc¸ alves et al., 2013). Elevated E-I ratios may also impair the capacity to compensate for future challenges or strong inputs (Ramocki and Zoghbi, 2008), as in audiogenic seizures (Rotschafer and Razak, 2013). This could occur in S1 with stronger or more complex tactile stimuli than were used here or during natural exploration or attention. E-I homeostasis may successfully preserve synaptic depolarization and spiking in sparsely active areas like S1 but may be insufficient in areas with denser input or less inhibition.

This compensatory model explains why diverse genetic mutations all alter E-I ratio, why firing rate is only modestly affected, and why Gex and Gin changes are coordinated to stabilize PSPs. Because E-I homeostasis is a natural response to network perturbation, E-I ratio changes are expected in numerous neurological disorders, as has been observed (Selten et al., 2018). This view predicts that enhancing inhibition may be insufficient to normalize ASD symptoms in cases or brain areas where effective E-I homeostasis (i.e., that normalizes cortical spike rate) has taken place.

3.5 Methods

ASD model mice were obtained from Jackson Labs ($Fmr1^{+/y}$: #004828, $Fmr1^{-/y}$: #004624; $Cntnap2^{+/-}$: #017482; 16p11.2 $^{del/+}$: #013128; $Tsc2^{+/-}$: #004686). Each strain was maintained on its own genetic background as purchased from Jackson: Fmr1 mice on a FVB background, Cntnap2 mice on C57BL/6J background, and 16p11.2 and Tsc2 mice on a mixed B6129S background. Genotyping was by PCR, using Jackson Lab protocols. Optogenetic tagging experiments were performed in PV-Cre::ChR2 mice, bred by crossing PV-Cre JAX #017320 with Ai32 JAX #024109. Mice were maintained on a 12:12-hr light-dark cycle. Mice were group-housed, and weaned at postnatal day (P) 21. Slice physiology experiments used male mice aged P17-P23. *In vivo* physiology

experiments used male mice aged P42-P92. All procedures were approved by the Institutional Animal Care and Use Committee at UC Berkeley.

Slice Preparation

S1 slices (350 μm thick) from P17-23 mice were cut using standard methods in the "across-row" plane oriented 35° toward coronal from midsagittal, which allows unambiguous identification of whisker barrel columns (House et al., 2011). Cutting solution contained (in mM): 85 NaCl, 75 sucrose, 25 D- (+)-glucose, 4 $MgSO_4$, 2.5 KCl, 1.25 NaH_2PO_4, 0.5 ascorbic acid, 25 $NaHCO_3$, 0.5 $CaCl_2$. Slices were then incubated at 32°C for 30 min in standard Ringer's solution (in mM: 119 NaCl, 2.5 KCl, 1.3 $MgSO_4$, 1 NaH_2PO_4, 26.2 $NaHCO_3$, 11 D-(+)-glucose and 2.5 $CaCl_2$; all solutions were pH 7.3, 300 mOsm, and bubbled with 95% O_2 and 5% CO_2). Slices were maintained at room temperature > 30 min before recording.

In Vitro Physiology

Synaptic physiology recordings were made at 30°C in standard Ringer's solution (2.5-3.0 mL/min). Spontaneous spiking was recorded at 35°C in Active Ringer's solution, which was identical to standard Ringer's except that it contained 3.5 mM KCl, 0.25 mM $MgSO_4$ and 1mM $CaCl_2$, ion concentrations that more closely resemble natural cerebrospinal fluid (Dani et al., 2005).

Whole-cell recordings were targeted using infrared DIC optics. L2/3 PYR cells were identified visually, and regular spiking was verified in current clamp. Recordings were made using 3–6 MΩ pipettes and a Multiclamp 700B amplifier (Molecular Devices, Sunnyvale, CA). Signals were low-pass filtered (2-6 kHz) and digitized (10-20 kHz).

For voltage clamp recordings, the internal contained (in mM): 108 D-gluconic acid, 108 CsOH, 20 HEPES, 5 tetraethylammonium-Cl, 2.8 NaCl, 0.4 EGTA, 4 MgATP, 0.3 NaGTP, 5 BAPTA, 5 QX314 bromide (adjusted to pH 7.2 with CsOH, 290 mOsm). For current clamp recordings, the internal contained: 116 K gluconate, 20 HEPES, 6 KCl, 2 NaCl, 0.5 EGTA, 4MgATP, 0.3 NaGTP, 105 Na phosphocreatine. Series resistance (*R*s) was required to be < 20 MΩ prior to compensation, and was compensated 60%–80% for voltage-clamp recording. Thus, initial *R*s was typically 13-19 MΩ prior to compensation, and 3-8 MΩ during recording. Bridge balance was used in current clamp. Input resistance (*R*in) and *R*s were monitored in each sweep. Cells were discarded if membrane potential (Vm) at break-in was > -60 mV, *R*in was < 75 MΩ, initial Rs was > 20 MΩ, or if *R*s or *R*in changed by > 20% during recording. Vm was corrected for a 12 mV liquid junction potential.

L4 was stimulated in the center of a barrel using a bipolar electrode (0.2 ms pulses). L2/3 PYR cells were recorded radially above the stimulus site. Eθ was defined as the minimal intensity that evoked an EPSC. The accuracy of Eθ determination in each cell was ± 2.4% (95% CI), based on repeated-measurements in 9 cells. Input-output curves were collected with 10 s isi, and 5-6 repetitions of each stimulus intensity. EPSCs and

IPSCs were quantified by area or peak, 3-23 ms post-stimulus. E-I ratio was calculated from EPSCs and IPSCs as E/(E+I). This is equal to the fraction of excitatory to total synaptic conductance, because EPSCs and IPSCs were measured with equal driving force, and scales with synaptic reversal potential. Mouse age did not correlate, over the age range tested, with evoked EPSC magnitude, IPSC magnitude or E/(E+I) in L2/3 pyramidal cells for any WT genotype, except for *Fmr1*$^{+/y}$ mice which showed a modest increase in E/(E+I) with age (data not shown). L4-evoked PSPs were measured from a pre-stimulus baseline Vm of −50 mV, using the "slow clamp" feature of the Multi-clamp (5 s tau). When calculating average PSP amplitude, stimulus trials containing a spike were replaced with the mean value of spike threshold for that cell. Similarly, when calculating average PSP waveform for a cell, stimulus trials containing a spike were replaced with the mean non-spike PSP for that cell, scaled to the cell's mean spike threshold.

mEPSCs and mIPSCs were recorded in TTX citrate (1 μM) and APV (100 μM), without QX-314 in the internal, holding at −72 and 0 mV respectively. In each cell, > 200 mEPSCs and > 200 mIPSCs were detected (criteria: > 5 pA amplitude, 10%–90% rise time and peak latency < 2.5 ms) and analyzed using TaroTools (Taro Ishikawa, Jikei University School of Medicine, Japan). Differences in mEPSC or mIPSC amplitude, frequency, and overall activity (quantified as amplitude × frequency within each cell) were evaluated using Mann-Whitney test ($\alpha = 0.05$). Cell-attached spiking was measured using loose-seal recordings in voltage clamp, with holding current at 0 pA. Intrinsic spiking excitability was measured in glutamate and GABA-A synaptic blockers (in μM: 100 APV, 10 NBQX, 3 gabazine). Rheobase was defined as the smallest positive current injection (500-ms duration) that elicited 1 or more spikes. F-I curves were measured using increasing current injections above each cell's individually determined rheobase.

Parallel conductance model

Synaptically evoked changes in V_m (ΔV_m) were predicted from L4-evoked EPSCs and IPSCs at 1.4 × Eθ using a parallel synaptic conductance model, implemented in MATLAB. For each cell, we first calculated the baseline-subtracted mean EPSC at −72 mV and mean IPSC at 0 mV. G_{ex} and G_{in} waveforms were calculated as $G = I/(V_{hold}-E_{rev})$, with $E_{ex} = 0$ mV and $E_{in} = -72$ mV. G_{ex} and G_{in} were constrained to be non-negative and were smoothed (Savitzky-Golay, 1-ms window). Next, we predicted ΔVm from G_{ex} and G_{in} using the parallel conductance equation (Wehr and Zador, 2003):

$$1)\ C(dV/dt)=G_{ex}(V_m-E_{ex})+G_{in}(V_m-E_{in})+G_{rest}(V_m-E_{rest})$$

C was 180 pF, which was the average membrane capacitance measured across our genotypes. G_{rest} was defined as $1 / R_{input}$, where R_{input} was the average input resistance measured for that genotype in current clamp recordings (Table S2). We simulated ΔVm for cells at $E_{rest} = -50$ mV, in order to estimate the effect of feedforward synaptic input on V_m as a cell approaches spike threshold. V_m was calculated by integrating Equation 1 from a starting value of $V_m = -50$ mV with 0.1 ms time resolution,

using Euler's method (House et al., 2011, Elstrott et al., 2014). Separate analysis was run using Erest = −70 mV.

In vivo recordings in anesthetized mice

Adult male mice were anaesthetized with urethane and chlorprothixene (1.3 g/kg and 0.02 mg in saline). Recording was not blind to genotype. A 2 mm craniotomy was made over S1. The mouse was fixed via a head post and the whiskers inserted into piezoelectric actuators. Body temperature was maintained at 36.5°C. Supplemental urethane was provided as needed. The C1, D1, C2 or D2 column was localized by intrinsic signal optical imaging or electrode mapping. A NeuroNexus recording probe (16 or 32 channels) was inserted radially via a small durotomy. The probe was advanced into L2/3, allowed to settle until stable activity was observed for 30 min, and L2/3 units were recorded. Then the probe was advanced to L4 and allowed to settle again before recording.

Recording location was confirmed either by (i) histological localization by DiI labeling in cytochrome oxidase stained flattened sections, which allow direct visualization of column boundaries, or (ii) by strong tuning for the columnar whisker in multi-unit recording in L4. L2/3 and L4 were defined by microdrive depth as 100 - 413 μm and 413-588 μm below the pia [58]. 1 recording site per layer was typically recorded. A median of 7 well-isolated single units were recorded in each animal. Recordings were typically made during the light phase of the mouse's light:dark cycle. Recording in juvenile mice (P18-22) used identical methods as for adults.
Whisker Stimuli: Calibrated piezo deflections were applied to the column-associated whisker (CW) and the 8 adjacent surround whiskers (SWs) in a 3 × 3 grid, using custom software in Igor Pro. Each whisker deflection was a ramp-hold-return (4 ms – 100 ms – 4 ms). 1.7° deflections were typically used for receptive field mapping. To measure velocity response curves, the CW was deflected at 0.6, 1.1, 1.7, 2.3, 2.9, 3.4, and 4°, with amplitude and velocity co-varying. 75-100 repetitions of each stimulus were presented at each recording site (2-2.5 s isi).
Analysis: Recordings were amplified and bandpass filtered (Plexon Instruments PBX2/16sp-G50, × 1,000 amplification, 0.3-8 kHz bandpass) and digitized at 31.25 kHz. Noise was reduced by common average referencing. Negative-going spikes were detected using an amplitude threshold (2.8-5 SD of background activity), followed by a shadow period of 0.66 ms after each threshold-crossing. 1.5-ms waveforms were clipped for spike sorting. Spike clustering used UltraMegaSort2000 (Hill et al., 2011) and was blind to genotype. Clusters were excluded if they had < 600 spikes, > 0.8% refractory period violations (inter-spike interval < 1.5 ms), or > 30% missed spikes (based on Gaussian fit of detected spike amplitudes relative to the detection threshold). FS and RS units were separated using a spike duration criterion of 0.55 ms peak-to-trough time.

Optogenetic identification of PV interneurons

To validate the spike duration criterion for FS units, we performed a separate series of experiments in which we optogenetically tagged PV interneurons *in vivo* and identified their spike waveform characteristics. These were performed in adult PV-Cre::ChR2 mice. Recording methods were exactly as described for the main *in vivo* experiments. Once the recording electrode was inserted into S1, we delivered 1-2 ms blue laser flashes (443 nm, 40 mW, CrystaLaser DL445) via an optical fiber (200 μm tip diameter) positioned in air 5 mm above the pial surface. Laser output power was adjusted for each recording site to achieve robust short-latency spiking responses from a subset of units. Units were identified as PV neurons if they exhibited light-evoked spiking at 2-5 ms latency after laser onset with a firing rate 10 standard deviations greater than their baseline firing rate.

In vivo recordings in awake mice

Mice were implanted with a lightweight chronic head post. A week later, mice began water regulation and trained operantly for water reward on the behavioral task. One behavioral session (~90 min, ~250 trials) took place each day, and mice were carefully monitored for general behavior, weight, and water consumption. At the start of each session, mice were transiently anesthetized (1.5% isoflurane), head-fixed, and the C1-3, D1-3, and E1-2 whiskers were placed in 8 piezo benders. In each 10 s trial, mice received interleaved whisker stimuli at 0.2 s ISI. Stimuli were the same as for the anesthetized experiment, except that a 5 ms caudal ramp, 0 ms hold, 5 ms return ramp was used. Most trials were 'NoGo' trials in which mice were not rewarded, and generally did not lick. A subset of trials were 'Go' trials in which a blue LED flashed at 8.5 s (after completion of the whisker stimuli for that trial) to indicate availability of water reward. Licks were monitored by infrared beam break and recorded. The fraction of 'Go' trials was adjusted daily to maximize total trial number the mouse would perform, and was typically ~50% in well-trained mice. Mice initiated trials by suppressing licking for 3 s. Mice were trained until they achieved a hit rate of ~85% (on 'Go' trials) and a false alarm rate of ~10% (licks on 'NoGo' trials). Training took ~2 weeks per mouse.

Once the behavioral criterion was obtained, C1-2 and D1-2 columns were localized by intrinsic signal imaging, and a craniotomy was performed. Spike recordings were made during behavior from L2/3 and L4 using laminar polytrodes (as above). Spikes were sampled (24.4144 kHz), and stored (TDT RZ5D). Neural signals were bandpass filtered offline (300-6000 Hz) and common average referenced using custom MATLAB code, and then spike sorted as for the anesthetized recordings. Epochs within ± 200 ms of a lick were excluded from analysis to avoid lick-related spiking in S1.

Data were analyzed from recordings whose L4 multi-unit tuning clearly matched the target whisker. RS and FS spikes were well-separated by a spike width criterion of 0.45 ms. Relatively high FS firing rates in awake mice prevented effective sorting and analysis of most FS single units, so only L2/3 RS units were analyzed.

Quantitative and Statistical Analysis

All phenotypes were evaluated by comparing each mutant genotype to its corresponding WT strain. Differences between the WTs strains reflect the different genetic backgrounds. For slice physiology data, statistical analyses were performed in Prism 7.0 (GraphPad). At least 2 mice and 2 separate litters were used for each measurement. Non-Gaussian data were either log-transformed for parametric testing, or nonparametric tests were applied, as specified in Results. 2-tailed tests were used, with$\alpha = 0.05$. Values in the text are mean ± SEM. Experiments were typically performed blind to genotype and conditions, except in a few cases where more animals of a specific genotype were required to balance the dataset. All data analysis was done blind to experimental conditions.

For conductance modeling, predicted PSP peak was quantified as maximum depolarization within 50 ms post-stimulus. Statistical tests are indicated in the figures, and used $\alpha = 0.05$. Hypothesized reductions in predicted EPSP or IPSP magnitude (strongly predicted by the voltage-clamp findings in Figure 1) were tested by 1-tailed KS test. Changes in total predicted PSP were tested by 2-tailed KS test, because no clear prior prediction was available.

For *in vivo* recordings, analysis was done in MATLAB. For anesthetized recordings, spontaneous firing rate was measured in each trial across multiple epochs beginning 0.7 s after stimulus offset, which is after whisker-evoked spiking or suppression has subsided. Whisker-evoked spiking was quantified during the epoch [4,50] ms after stimulus onset. For awake recordings, spontaneous firing rate was calculated from the epoch [-50,-4] ms before each whisker stimulus, and evoked firing rate from the epoch [4,50] ms following each stimulus. To determine whether a whisker evoked a significant response from a unit, we computed the probability that a Poisson process with that unit's mean spontaneous firing would generate the number of spikes measured after whisker deflection, using a binless method. For this test, we used $\alpha = 0.0056$ for each whisker ($\alpha = 0.05 / 9$ whiskers) for anesthetized experiments, and $\alpha = 0.00625$ ($\alpha = 0.05 / 8$ whiskers) for awake experiments. Units with significant response to at least 1 whisker were considered whisker-responsive. Whisker receptive field size was the total number of whiskers to which a unit was significantly responsive. The 'best whisker' (BW) was defined as the whisker evoking numerically the greatest number of spikes.

Tuning width, tuning accuracy and response latency were calculated only for whisker-responsive units. Response magnitude (e.g., in the velocity response curve) was computed across all single units, including those that were not significantly responsive. Latency was calculated from all combined spikes evoked by significant whiskers, as the earliest time bin at which evoked firing rate exceeded spontaneous firing rate modeled as a Poisson process ($\alpha = 0.05$). Jitter was calculated as the standard deviation of spike times 4-50 ms post-stimulus, measured across all whiskers within a unit's whisker receptive field. Tuning sharpness was defined as the firing rate evoked by the BW divided by the sum of the BW-evoked firing rate plus mean firing rate to all immediately adjacent whiskers. Response latency, jitter and unit depth were normally distributed and genotype differences were evaluated by 2-tailed t test ($\alpha = 0.05$). Velocity response curve data from all units of a given genotype were combined and fit to a sigmoid

function using nonlinear regression using the ‘fitnlm’ MATLAB function, using the cauchy robust weighting option. For VRC fits, statistical differences between genotypes in parameter values were determined by t test with $\alpha = 0.007$, reflecting Bonferroni correction of total $\alpha = 0.05$ across 7 different deflection velocities within the VRC. All other statistical comparisons were made by permutation test with $\alpha = 0.05$.

Signal correlation, noise correlation and spike synchrony were calculated from all pairs of simultaneously recorded L2/3 RS neurons located < 0.2 mm apart (location inferred from the recording pad at which spike amplitude was maximal for each unit). Signal and noise correlation were calculated using MATLAB’s corrcoef() function. Spike synchrony was calculated from cross-correlograms generated with MATLAB’s xcorr() function, using 0.5 ms bin size and ‘coeff’ normalization to remove effects of firing rate. Synchrony was calculated as the mean cross-correlation value over ± 10 ms, excluding 0 and ± 0.5 ms bins where the shadow period during spike detection prevented simultaneous spikes from being recorded.

3.6 References

Arnett, M.T., Herman, D.H., and McGee, A.W. (2014). Deficits in tactile learning in a mouse model of fragile X syndrome. PLoS ONE 9, e109116.

Banerjee, A., Rikhye, R.V., Breton-Provencher, V., Tang, X., Li, C., Li, K., Runyan, C.A., Fu, Z., Jaenisch, R., and Sur, M. (2016). Jointly reduced inhibition and excitation underlies circuit-wide changes in cortical processing in Rett syndrome. Proc. Natl. Acad. Sci. USA 113, E7287–E7296.

Berzhanskaya, J., Phillips, M.A., Shen, J., and Colonnese, M.T. (2016). Sensory hypo-excitability in a rat model of fetal development in Fragile X Syndrome. Sci. Rep. 6, 30769.

Chao, H.-T., Chen, H., Samaco, R.C., Xue, M., Chahrour, M., Yoo, J., Neul, J.L., Gong, S., Lu, H.-C., Heintz, N., et al. (2010). Dysfunction in GABA signaling mediates autism-like stereotypies and Rett syndrome phenotypes. Nature 468, 263–269.

Dani, V.S., Chang, Q., Maffei, A., Turrigiano, G.G., Jaenisch, R., and Nelson, S.B. (2005). Reduced cortical activity due to a shift in the balance between excitation and inhibition in a mouse model of Rett syndrome. Proc. Natl. Acad. Sci. USA 102, 12560–12565.

Delattre, V., La Mendola, D., Meystre, J., Markram, H., and Markram, K. (2013). Nlgn4 knockout induces network hypo-excitability in juvenile mouse somatosensory cortex in vitro. Sci. Rep. 3, 2897.

Deng, P.-Y., Rotman, Z., Blundon, J.A., Cho, Y., Cui, J., Cavalli, V., Zakharenko, S.S., and Klyachko, V.A. (2013). FMRP regulates neurotransmitter

release and synaptic information transmission by modulating action potential duration via BK channels. Neuron 77, 696–711.

Dhamne, S.C., Silverman, J.L., Super, C.E., Lammers, S.H.T., Hameed, M.Q., Modi, M.E., Copping, N.A., Pride, M.C., Smith, D.G., Rotenberg, A., et al. (2017). Replicable in vivo physiological and behavioral phenotypes of the Shank3B null mutant mouse model of autism. Mol. Autism 8, 26.

Dolen, G., Osterweil, E., Rao, B.S.S., Smith, G.B., Auerbach, B.D., Chattarji, S., and Bear, M.F. (2007). Correction of fragile X syndrome in mice. Neuron 56, 955–962.

Durand, S., Patrizi, A., Quast, K.B., Hachigian, L., Pavlyuk, R., Saxena, A., Carninci, P., Hensch, T.K., and Fagiolini, M. (2012). NMDA receptor regulation prevents regression of visual cortical function in the absence of Mecp2. Neuron 76, 1078–1090.

Elstrott, J., Clancy, K.B., Jafri, H., Akimenko, I., and Feldman, D.E. (2014). Cellular mechanisms for response heterogeneity among L2/3 pyramidal cells in whisker somatosensory cortex. J. Neurophysiol. 112, 233–248.

Gabernet, L., Jadhav, S.P., Feldman, D.E., Carandini, M., and Scanziani, M. (2005). Somatosensory integration controlled by dynamic thalamocortical feed-forward inhibition. Neuron 48, 315–327.

Gainey, M.A., and Feldman, D.E. (2017). Multiple shared mechanisms for homeostatic plasticity in rodent somatosensory and visual cortex. Philos. Trans. R. Soc. Lond. B Biol. Sci. 372, 372.

Gainey, M.A., Aman, J.W., and Feldman, D.E. (2018). Rapid disinhibition by adjustment of PV intrinsic excitability during whisker map plasticity in mouse S1. J. Neurosci. 38, 4749–4761.

Garcia-Junco-Clemente, P., Chow, D.K., Tring, E., Lazaro, M.T., Trachtenberg, J.T., and Golshani, P. (2013). Overexpression of calcium-activated potassium channels underlies cortical dysfunction in a model of PTEN-associated autism. Proc. Natl. Acad. Sci. USA 110, 18297–18302.

Geschwind, D.H. (2009). Advances in autism. Annu. Rev. Med. 60, 367–380.

Gibson, J.R., Bartley, A.F., Hays, S.A., and Huber, K.M. (2008). Imbalance of neocortical excitation and inhibition and altered UP states reflect network hyperexcitability in the mouse model of fragile X syndrome. J. Neurophysiol. 100, 2615–2626.

Goel, A., Cantu, D.A., Guilfoyle, J., Chaudhari, G.R., Newadkar, A., Todisco, B., de Alba, D., Kourdougli, N., Schmitt, L.M., Pedapati, E., et al. (2018).

Impaired perceptual learning in a mouse model of Fragile X syndrome is mediated by parvalbumin neuron dysfunction and is reversible. Nat. Neurosci. 21, 1404–1411.

Gonc¸ alves, J.T., Anstey, J.E., Golshani, P., and Portera-Cailliau, C. (2013). Circuit level defects in the developing neocortex of Fragile X mice. Nat. Neurosci. 16, 903–909.

Goorden, S.M.I., van Woerden, G.M., van der Weerd, L., Cheadle, J.P., and Elgersma, Y. (2007). Cognitive deficits in Tsc1+/- mice in the absence of cerebral lesions and seizures. Ann. Neurol. 62, 648–655.

Han, S., Tai, C., Westenbroek, R.E., Yu, F.H., Cheah, C.S., Potter, G.B., Rubenstein, J.L., Scheuer, T., de la Iglesia, H.O., and Catterall, W.A. (2012). Autistic-like behaviour in Scn1a+/- mice and rescue by enhanced GABA-mediated neurotransmission. Nature 489, 385–390.

Harrington, A.J., Raissi, A., Rajkovich, K., Berto, S., Kumar, J., Molinaro, G., Raduazzo, J., Guo, Y., Loerwald, K., Konopka, G., et al. (2016). MEF2C regulates cortical inhibitory and excitatory synapses and behaviors relevant to neurodevelopmental disorders. eLife 5, 5.

Hays, S.A., Huber, K.M., and Gibson, J.R. (2011). Altered neocortical rhythmic activity states in Fmr1 KO mice are due to enhanced mGluR5 signaling and involve changes in excitatory circuitry. J. Neurosci. 31, 14223–14234.

He, L.J., Liu, N., Cheng, T.L., Chen, X.J., Li, Y.D., Shu, Y.S., Qiu, Z.L., and Zhang, X.H. (2014). Conditional deletion of Mecp2 in parvalbumin-expressing GABAergic cells results in the absence of critical period plasticity. Nat. Commun. 5, 5036.

He, C.X., Cantu, D.A., Mantri, S.S., Zeiger, W.A., Goel, A., and Portera-Cailliau, C. (2017). Tactile defensiveness and impaired adaptation of neuronal activity in the Fmr1 knock-out mouse model of autism. J. Neurosci. 37, 6475–6487.

Hill, D.N., Mehta, S.B., and Kleinfeld, D. (2011). Quality metrics to accompany spike sorting of extracellular signals. J. Neurosci. 31, 8699–8705.
House, D.R.C., Elstrott, J., Koh, E., Chung, J., and Feldman, D.E. (2011). Parallel regulation of feedforward inhibition and excitation during whisker map plasticity. Neuron 72, 819–831.

Juczewski, K., von Richthofen, H., Bagni, C., Celikel, T., Fisone, G., and Krieger, P. (2016). Somatosensory map expansion and altered processing of tactile inputs in a mouse model of fragile X syndrome. Neurobiol. Dis. 96, 201–215.

Jurgensen, S., and Castillo, P.E. (2015). Selective dysregulation of hippocampal inhibition in the mouse lacking autism candidate gene CNTNAP2. J. Neurosci. 35, 14681–14687.

Li, L., Gainey, M.A., Goldbeck, J.E., and Feldman, D.E. (2014). Rapid homeostasis by disinhibition during whisker map plasticity. Proc. Natl. Acad. Sci. USA 111, 1616–1621.

Liang, J., Xu, W., Hsu, Y.T., Yee, A.X., Chen, L., and S€udhof, T.C. (2015). Conditional knockout of Nlgn2 in the adult medial prefrontal cortex (mPFC) induces delayed loss of inhibitory synapses. Mol. Psychiatry 20, 793.

Mao, W., Watanabe, T., Cho, S., Frost, J.L., Truong, T., Zhao, X., and Futai, K. (2015). Shank1 regulates excitatory synaptic transmission in mouse hippocampal parvalbumin-expressing inhibitory interneurons. Eur. J. Neurosci. 41, 1025–1035.

McGuire, L.M., Telian, G., Laboy-Jua´ rez, K.J., Miyashita, T., Lee, D.J., Smith, K.A., and Feldman, D.E. (2016). Short time-scale sensory coding in S1 during discrimination of whisker vibrotactile sequences. PLoS Biol. 14, e1002549.

Nelson, S.B., and Valakh, V. (2015). Excitatory/inhibitory balance and circuit homeostasis in autism spectrum disorders. Neuron 87, 684–698.

O'Donnell, C., Gonc¸ alves, J.T., Portera-Cailliau, C., and Sejnowski, T.J. (2017). Beyond excitation/inhibition imbalance in multidimensional models of neural circuit changes in brain disorders. eLife 6, 6.

Peixoto, R.T., Wang, W., Croney, D.M., Kozorovitskiy, Y., and Sabatini, B.L. (2016). Early hyperactivity and precocious maturation of corticostriatal circuits in Shank3B(-/-) mice. Nat. Neurosci. 19, 716–724.

Penagarikano, O., Abrahams, B.S., Herman, E.I., Winden, K.D., Gdalyahu, A., Dong, H., Sonnenblick, L.I., Gruver, R., Almajano, J., Bragin, A., et al. (2011). Absence of CNTNAP2 leads to epilepsy, neuronal migration abnormalities, and core autism-related deficits. Cell 147, 235–246.

Ramocki, M.B., and Zoghbi, H.Y. (2008). Failure of neuronal homeostasis results in common neuropsychiatric phenotypes. Nature 455, 912–918.

Robertson, C.E., and Baron-Cohen, S. (2017). Sensory perception in autism. Nat. Rev. Neurosci. 18, 671–684.

Rotschafer, S., and Razak, K. (2013). Altered auditory processing in a mouse model of fragile X syndrome. Brain Res. 1506, 12–24.

Rubenstein, J.L.R., and Merzenich, M.M. (2003). Model of autism: increased ratio of excitation/inhibition in key neural systems. Genes Brain Behav. 2, 255–267.

Samra, N.M., Abdel Ghaffar, H.M., El Awady, H.A., Soltan, M.R., and Moktader, R.M.A. (2017). Epilepsy and EEG Findings in Children with Autism Spectrum Disorders. Autism Open Access 07.

Selby, L., Zhang, C., and Sun, Q.-Q. (2007). Major defects in neocortical GABAergic inhibitory circuits in mice lacking the fragile X mental retardation protein. Neurosci. Lett. 412, 227–232.

Selimbeyoglu, A., Kim, C.K., Inoue, M., Lee, S.Y., Hong, A.S.O., Kauvar, I., Ramakrishnan, C., Fenno, L.E., Davidson, T.J., Wright, M., and Deisseroth, K. (2017). Modulation of prefrontal cortex excitation/inhibition balance rescues social behavior in CNTNAP2-deficient mice. Sci. Transl. Med. 9, 9.

Selten, M., van Bokhoven, H., and Nadif Kasri, N. (2018). Inhibitory control of the excitatory/inhibitory balance in psychiatric disorders. F1000Res. 7, 23. Tabuchi, K., Blundell, J., Etherton, M.R., Hammer, R.E., Liu, X., Powell, C.M., and S€udhof, T.C. (2007). A neuroligin-3 mutation implicated in autism increases inhibitory synaptic transmission in mice. Science 318, 71–76.

Tuchman, R., Cuccaro, M., and Alessandri, M. (2010). Autism and epilepsy: historical perspective. Brain Dev. 32, 709–718.

Turrigiano, G. (2011). Too many cooks? Intrinsic and synaptic homeostatic mechanisms in cortical circuit refinement. Annu. Rev. Neurosci. 34, 89–103.

Tyzio, R., Nardou, R., Ferrari, D.C., Tsintsadze, T., Shahrokhi, A., Eftekhari, S., Khalilov, I., Tsintsadze, V., Brouchoud, C., Chazal, G., et al. (2014). Oxytocin-mediated GABA inhibition during delivery attenuates autism pathogenesis in rodent offspring. Science 343, 675–679.

Unichenko, P., Yang, J.W., Kirischuk, S., Kolbaev, S., Kilb, W., Hammer, M., Krueger-Burg, D., Brose, N., and Luhmann, H.J. (2018). Autism related Neuroligin-4 knockout impairs intracortical processing but not sensory inputs in mouse barrel cortex. Cereb. Cortex 28, 2873–2886.

Vogt, D., Cho, K.K.A., Shelton, S.M., Paul, A., Huang, Z.J., Sohal, V.S., and Rubenstein, J.L.R. (2018). Mouse Cntnap2 and Human CNTNAP2 ASD Alleles Cell Autonomously Regulate PV+ Cortical Interneurons. Cereb. Cortex 28, 3868–3879.

Wallace, M.L., Burette, A.C., Weinberg, R.J., and Philpot, B.D. (2012). Maternal loss of Ube3a produces an excitatory/inhibitory imbalance through neuron type-specific synaptic defects. Neuron 74, 793–800.

Wallace, M.L., van Woerden, G.M., Elgersma, Y., Smith, S.L., and Philpot, B.D. (2017). Ube3a loss increases excitability and blunts orientation tuning in the visual cortex of Angelman syndrome model mice. J. Neurophysiol. 118, 634–646.

Wehr, M., and Zador, A.M. (2003). Balanced inhibition underlies tuning and sharpens spike timing in auditory cortex. Nature 426, 442–446.

Wood, L., and Shepherd, G.M.G. (2010). Synaptic circuit abnormalities of motor-frontal layer 2/3 pyramidal neurons in a mutant mouse model of Rett syndrome. Neurobiol. Dis. 38, 281–287.

Yamashita, T., Pala, A., Pedrido, L., Kremer, Y., Welker, E., and Petersen, C.C.H. (2013). Membrane potential dynamics of neocortical projection neurons driving target-specific signals. Neuron 80, 1477–1490.

Yizhar, O., Fenno, L.E., Prigge, M., Schneider, F., Davidson, T.J., O'Shea, D.J., Sohal, V.S., Goshen, I., Finkelstein, J., Paz, J.T., et al. (2011). Neocortical excitation/inhibition balance in information processing and social dysfunction. Nature 477, 171–178.

Zhang, Y., Bonnan, A., Bony, G., Ferezou, I., Pietropaolo, S., Ginger, M., Sans, N., Rossier, J., Oostra, B., LeMasson, G., and Frick, A. (2014). Dendritic channelopathies contribute to neocortical and sensory hyperexcitability in Fmr1(-/y) mice. Nat. Neurosci. 17, 1701–1709.

3.7 Supplementary Figures and Tables

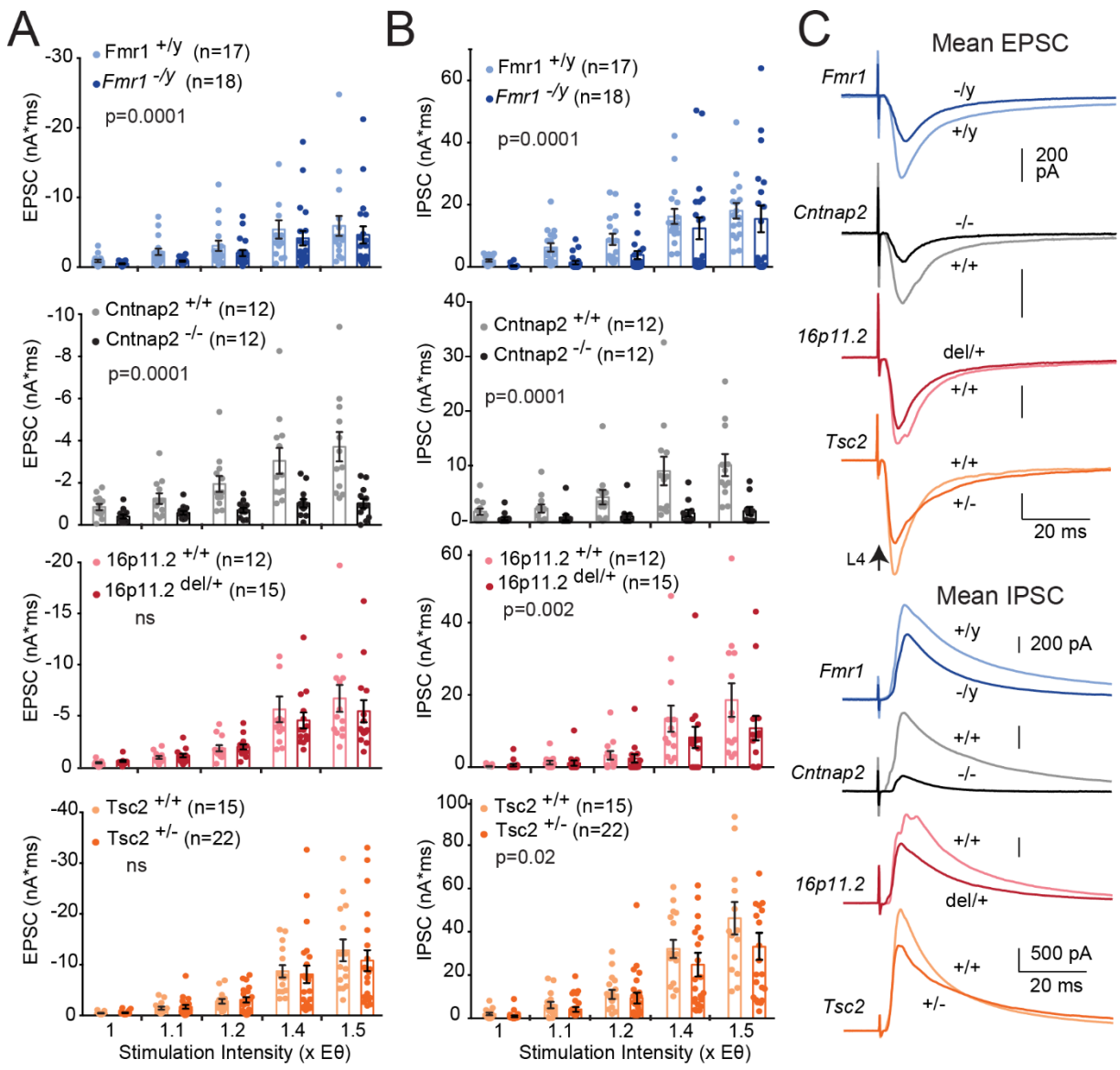

Figure S1. Individual cell data points and mean EPSC and IPSC waveforms for the input-output curve experiment in Figure 1. Related to Figure 1. (A) Input-output curves for EPSCs. Each point is a cell. Bars show mean ± SEM. P-values are for genotype factor in a 2-way ANOVA on log-transformed data. N are number of cells. (B) Input-output curves for IPSCs. (C) Mean EPSC and IPC waveforms at 1.4x Eθ, across all cells in (A) and (B).

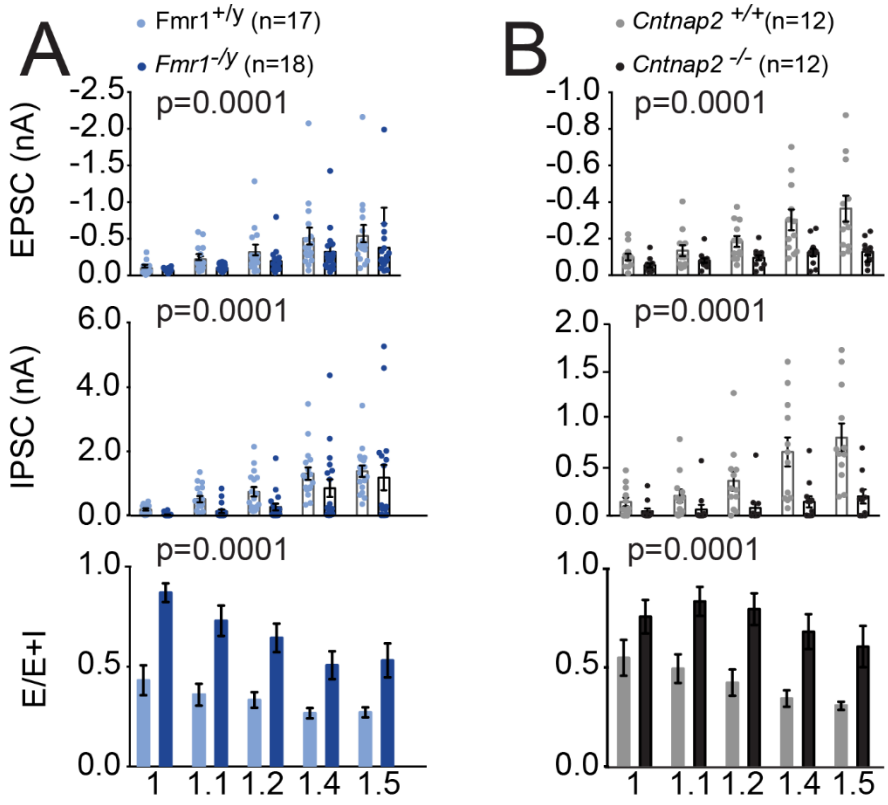
A
Fmr1+/y (n=17)
Fmr1-/y (n=18)
EPSC (nA)
p=0.0001
IPSC (nA)
p=0.0001
E/E+I
p=0.0001
1 1.1 1.2 1.4 1.5
B
Cntnap2 +/+(n=12)
Cntnap2 -/- (n=12)
p=0.0001
p=0.0001
p=0.0001
1 1.1 1.2 1.4 1.5

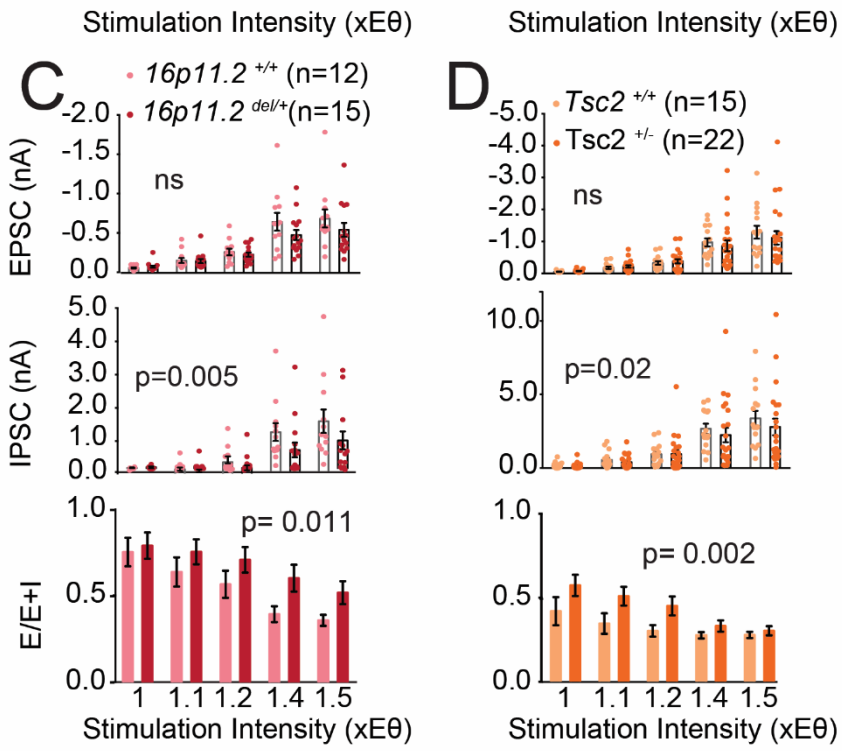

Figure S2. EPSC, IPSC and E-I ratio for the cells in Figure 1 analyzed by peak current amplitude. Related to Figure 1. (A) Reanalysis of Figure 1 input-output curves for L4-evoked EPSCs, IPSCs, and E-I ratio in Fmr1$^{-/y}$ and Fmr1$^{+/y}$ mice, analyzed by peak current amplitude. Conventions as in Figure S1. P-values are for genotype factor in 2-way ANOVA on log-transformed data. (B-D) Same analysis for Cntnap2$^{-/-}$, 16p11.2$^{del/+}$, and Tsc2$^{+/-}$ and corresponding wild types.

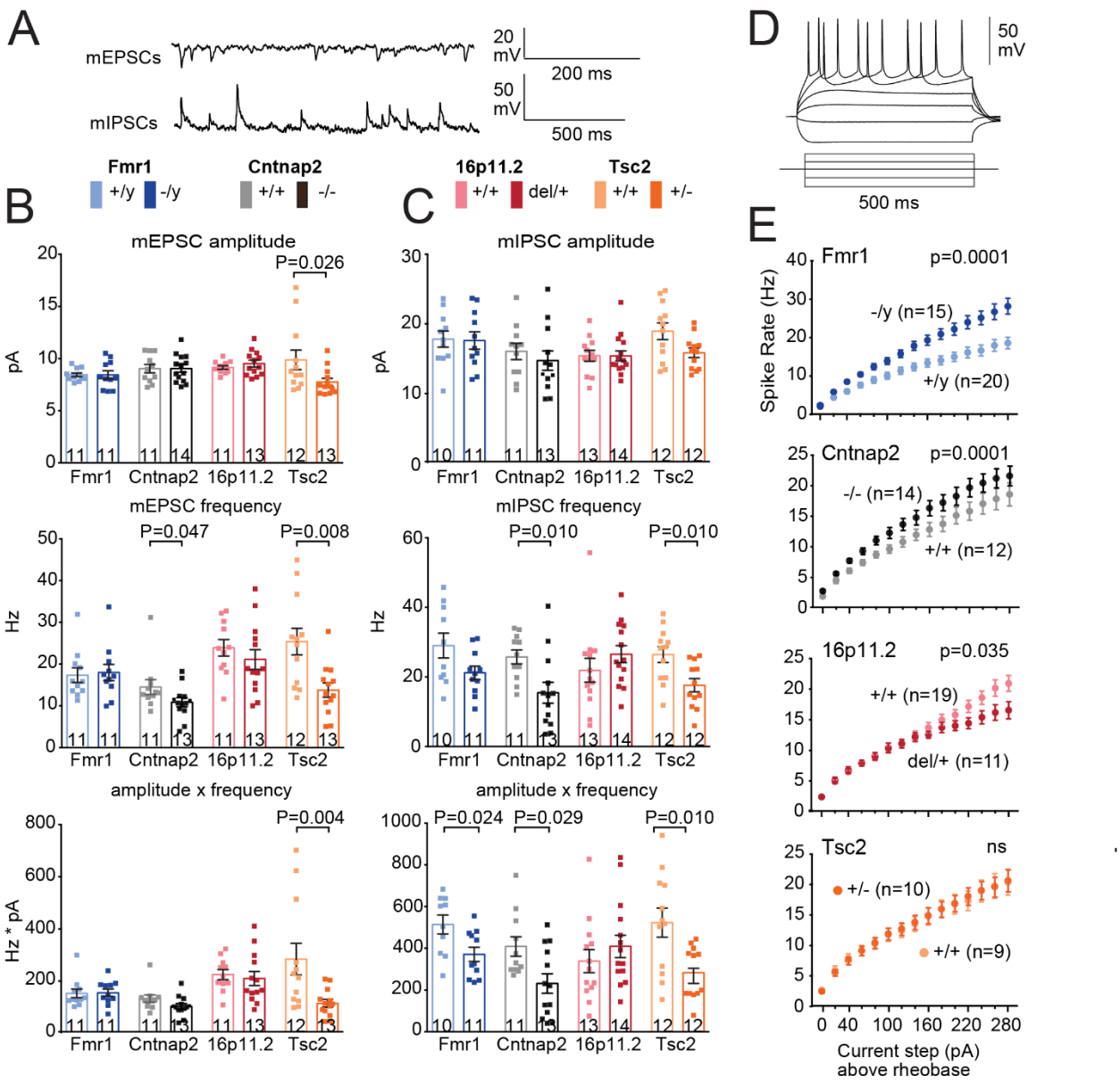

Figure S3. Miniature synaptic currents and intrinsic excitability in L2/3 PYR cells. Related to Figure 1. (A) Example mEPSCs and mIPSCs traces. (B) mEPSC amplitude, frequency and overall activity (product of amplitude x frequency within each cell). Each dot is one cell. Bars, mean ± SEM. Numbers are cell n. (C) mIPSC amplitude, frequency and overall activity. P-values from Mann-Whitney test between ASD mutant and corresponding wild type. Overall mIPSC activity was reduced 3 strains ($Fmr1^{-/y}$, $Cntnap2^{-/-}$ and $Tsc2^{+/-}$) relative to wild type. mEPSC activity was normal in 3 strains, but was reduced in $Tsc2^{+/-}$. 5 (D) F-I curve protocol showing current injection (500 ms) and evoked spiking in one L2/3 PYR cell. (E) Quantification of evoked spiking for F-I curves across all cells (9-20 cells per genotype). Points show mean ± SEM. p-values report genotype effect in 2-factor ANOVA on log-transformed data. $Fmr1^{-/y}$ and $Cntnap2^{-/-}$ exhibited increased spiking relative to wild type, while $16p11.2^{del/+}$ showed reduced spiking.

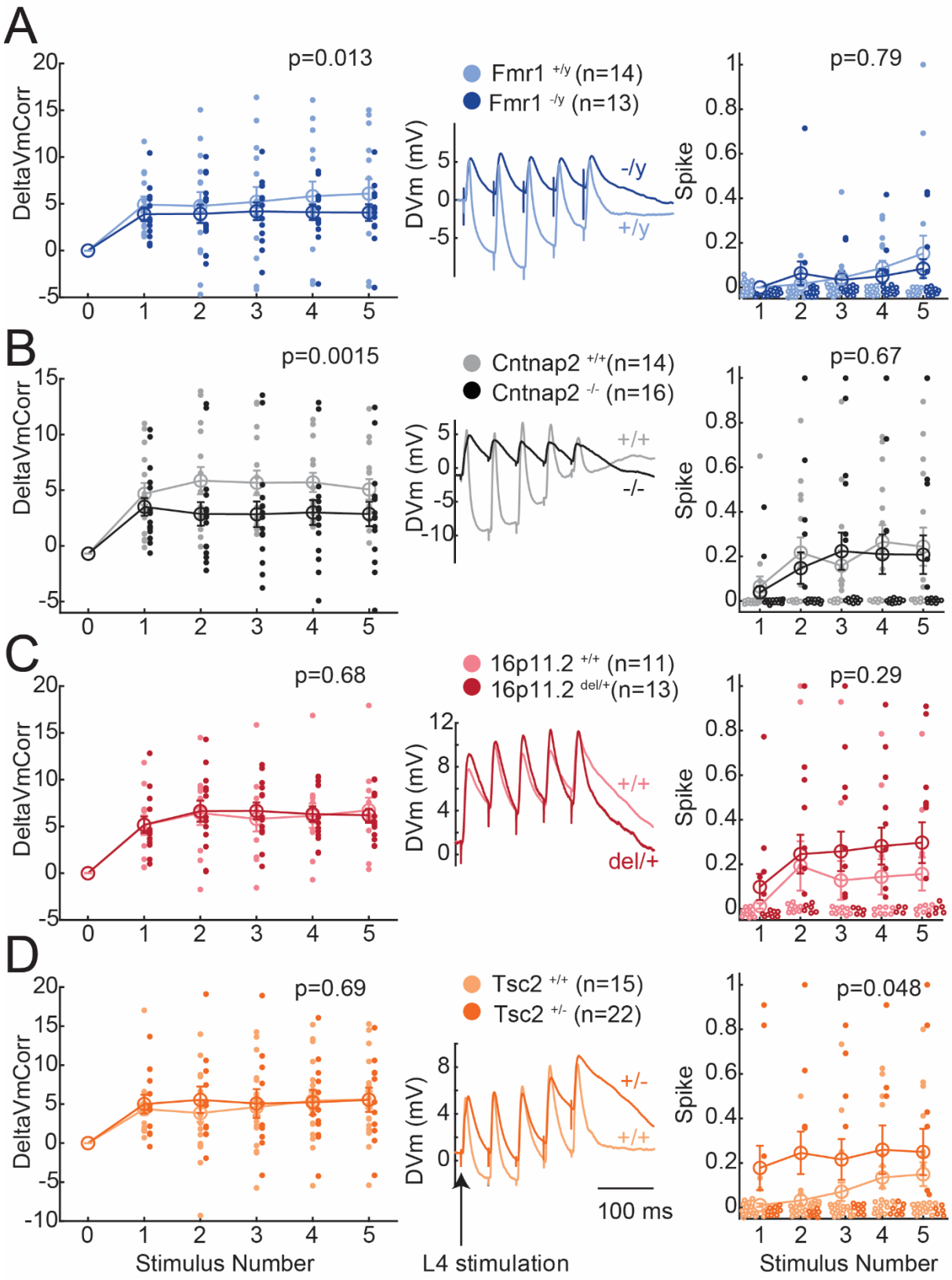
A
p=0.013
DeltaVmCorr
Fmr1 +/y (n=14)
Fmr1 -/y (n=13)
DVm (mV)
-/y
+/y
p=0.79
Spike
B
p=0.0015
DeltaVmCorr
Cntnap2 +/+(n=14)
Cntnap2 -/- (n=16)
DVm (mV)
+/+
-/-
p=0.67
Spike
C
p=0.68
DeltaVmCorr
16p11.2 +/+ (n=11)
16p11.2 del/+(n=13)
DVm (mV)
+/+
del/+
p=0.29
Spike
D
p=0.69
DeltaVmCorr
Tsc2 +/+ (n=15)
Tsc2 +/- (n=22)
DVm (mV)
+/-
+/+
100 ms
L4 stimulation
p=0.048
Spike
Stimulus Number
Stimulus Number

Figure S4. L4 train-evoked PSPs and spikes in L2/3 PYR cells. Related to Figure 2. (A) Amplitude of PSPs evoked by L4 stimulus trains (5 pulses at 20 Hz) from baseline V_m of -50 mV. L4 stimulation was at 1.4 x Eθ. Amplitude of each PSP was calculated relative to pre-train baseline V_m. Each small point is one cell, open points and error bars are mean ± SEM for the cell population. p-values are for genotype factor within a 2-factor ANOVA. 7 (B) PSP waveforms for example cells for the experiment in (A). In the y-axis, V_m is relative to pre-stimulus baseline (mV). (C) Train-evoked spike probability for the same experiment. P-values are from permutation test on total number of evoked spikes in the train (α=0.05). Points at y=0 are spread out to allow visualization.

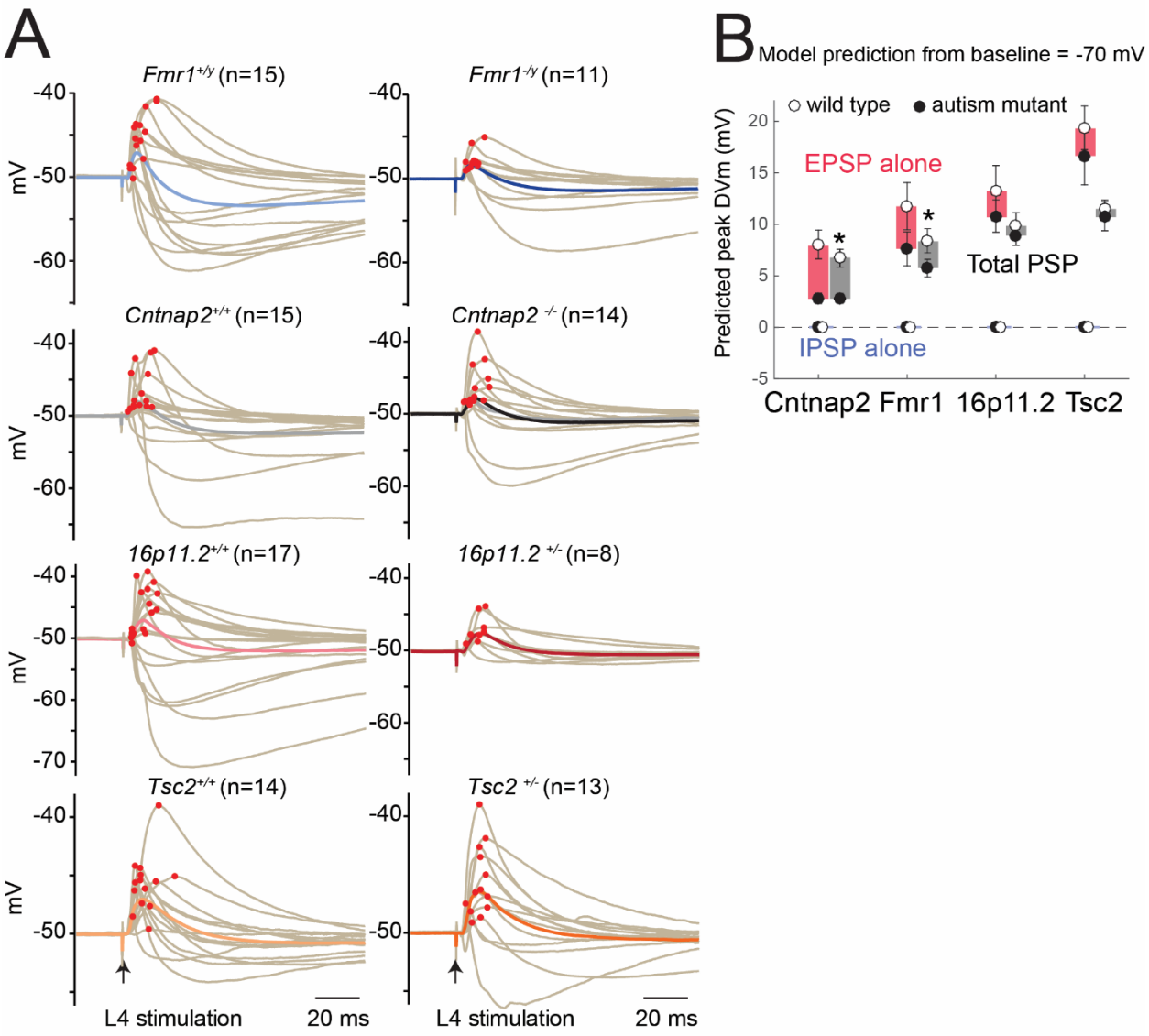

Figure S5. Validation of model results by measuring L4-evoked PSPs with NMDA currents blocked, and model results from baseline V_m of -70 mV. Related to Figure 4. (A) Validation of model results by measuring L4-evoked PSPs with NMDA currents blocked. Measurements were from baseline V_m of -50 mV,

with L4 stimulation at 1.4 x Eθ. Each trace is one cell (mean of 16 sweeps). APV was present to block NMDA currents, in order to better match the conditions of parallel conductance model, which lacks voltage-activated conductances. Dots show the peak depolarization for each cell. Bold traces show mean PSP. (B) Model predictions of PSPs from baseline V_m of -70 mV. Circles show mean predicted EPSP, IPSP, and total PSP peak for each genotype. Results show a predicted decrease in evoked PSP peak. Stars, p<0.05, KS test.

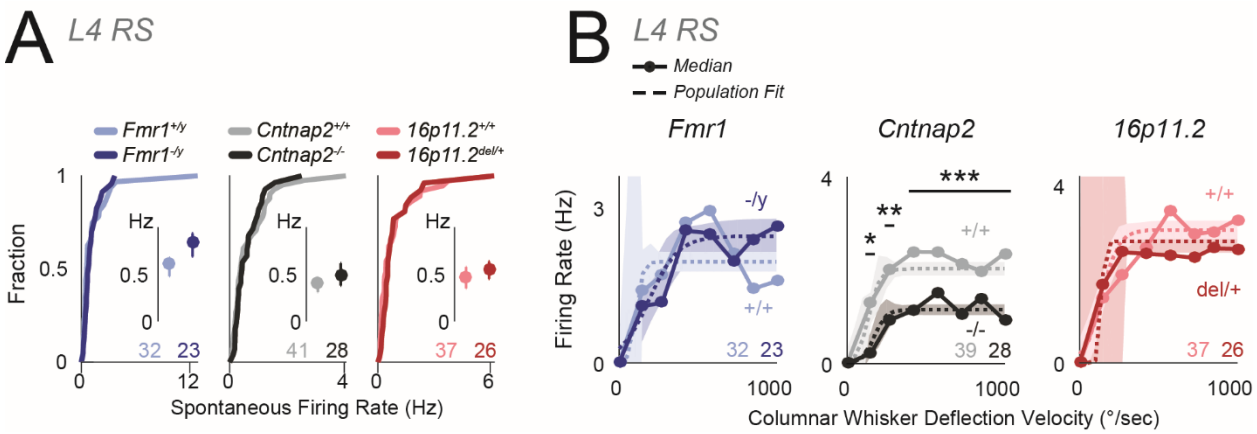

Figure S6. Firing of L4 RS units is largely normal in anesthetized mice in vivo. Related to Figure 6. (A) Spontaneous firing rate for L4 RS units, shown as cumulative distributions. Insets: Bootstrapped medians with 68% CI. In all panels, numbers are units per genotype. (B) Velocity response curves. Conventions as in Figures 5-6. * p=0.04, ** p=0.004, *** p<0.0001 t-test. CI for $Fmr1^{+/y}$ and $16p11.2^{+/+}$ are truncated at axis limit

		Fmr1		*Cntnap2*		*16p11.2*		*Tsc2*	
Figure		**N mice**	**Age (days)**	**N mice**	**Age (days)**	**N mice**	**Age (days)**	**N mice**	**Age (days)**
1	wt	5	19.3±0.3	4	17.9±0.2	5	19.7±0.5	3	18.5±0.4
	mut	5	19.6±0.4	5	18.8±0.4	5	19.3±0.7	5	18.3±0.4
2C	wt	5	20.8±0.8	4	21.0±1.4	5	19.4±0.7	6	18.7±0.7
	mut	5	19.6±0.7	4	22.2±0.5	5	20.2±0.9	5	19.0±0.7
2E-F	wt	5	21.2±0.3	3	19.9±0.3	3	19.4±0.2	8	19.2±0.3
	mut	5	20.4±0.4	3	21.4±0.4	4	21.4±0.3	3	22.2±0.3
4E-F	wt	3	20.3±0.1	3	22.5±0.1	2	18.2±0.3	4	20.6±0.4
	mut	3	21.5±0.1	3	21.4±0.5	4	20.0±0.0	3	20.8±0.6
S3A-C	wt	3	21.1±0.3	5	20.3±0.5	3	19.8±0.4	3	22.4±0.1
	mut	3	21.0±0.3	4	18.9±0.5	3	20.6±0.4	4	21.8±0.6
S4	wt	5	20.9±0.3	6	19.8±0.3	6	18.8±0.3	12	19.3±0.3
	mut	7	19.1±0.5	6	20.1±0.4	7	20.1±0.6	4	21.4±0.7
S3D	wt	4	21.7±0.5	3	22.3±0.2	6	20.3±0.5	3	18.3±0.2
	mut	4	19.7±0.3	3	21.9±0.2	3	20.2±0.6	5	21.5±0.4

Table S1. Number and age of mice for in vitro experiments. Age is shown as mean ± SEM. Related to Figures 1, 2 and 4.

	Fmr1$^{+/y}$ Fmr1$^{-/y}$	*Cntnap2*$^{+/+}$ *Cntnap2*$^{-/-}$	*16p11.2*$^{+/+}$ *16p11.2*$^{del/+}$	*Tsc2*$^{+/+}$ *Tsc2*$^{+/-}$
EPSC amplitude at Eθ (nA)	-0.098 ± 0.02 -0.064 ± 0.01	-0.099 ± 0.02 -0.054 ± 0.01	-0.054 ± 0.01 -0.070 ± 0.01	-0.050 ± 0.01 -0.070 ± 0.01
Stimulus intensity at Eθ (μA)	6.6 ± 0.9 5.4 ± 0.6	6.5 ± 0.6 5.5 ± 0.8	5.8 ± 0.9 4.1 ± 0.2	3.5 ± 0.1 4.4 ± 0.5
V_{rest} (mV)	-78.0 ± 1.1 -78.6 ± 1.0	-76.7 ± 1.0 -77.9 ± 1.0	-79.7 ± 1.6 -79.5 ± 1.3	-82.3 ± 1.2 -81.6 ± 1.1
C_m (pF)	171.1 ± 17.3 183.6 ± 18.3	149.6 ± 17.3 115.9 ± 21.6	215.7 ± 12.5 209.7 ± 17.3	192.6 ± 11.4 213.1 ± 12.4
R_{input} (MΩ)	325.3 ± 37.7 316.9 ± 18.8	298.2 ± 41.6 324.2 ± 38.1	250.2 ± 40.6 243.9 ± 37.3	349.5 ± 29.0 267.6 ± 23.6*
EPSC onset latency (ms)	2.6 ± 0.1 2.9 ± 0.2	2.6 ± 0.2 2.5 ± 0.1	2.8 ± 0.1 2.4 ± 0.2	2.2 ± 0.1 2.4 ± 0.1
IPSC onset latency (ms)	4.2 ± 0.3 4.3 ± 0.3	5.0 ± 0.5 5.3 ± 0.3	4.0 ± 0.1 4.1 ± 0.3	3.3 ± 0.3 3.4 ± 0.1
EPSC peak latency (ms)	7.6 ± 0.3 6.6 ± 0.4	8.0 ± 0.3 7.0 ± 0.5	6.8 ± 0.4 6.3 ± 0.5	5.7 ± 0.2 6.3 ± 0.4
IPSC peak latency (ms)	9.5 ± 0.7 8.1 ± 0.5	9.4 ± 0.9 7.5 ± 0.5	7.8 ± 0.7 8.3 ± 0.8	6.5 ± 0.2 7.6 ± 0.8
IPSC-EPSC peak latency (ms)	1.9 ± 0.6 1.0 ± 0.5	1.5 ± 0.7 0.8 ± 0.7	0.9 ± 0.5 1.8 ± 0.7	0.8 ± 0.3 1.2 ± 0.5

Table S2. Cellular properties of L2/3 PYR neurons for Figure 1 experiments. Related to Figure 1.

	Fmr1$^{+/y}$ *Fmr1*$^{-/y}$	*Cntnap2*$^{+/+}$ *Cntnap2*$^{-/-}$	*16p11.2*$^{+/+}$ *16p11.2*$^{del/+}$	*Tsc2*$^{+/+}$ *Tsc2*$^{+/-}$
General passive and spiking properties				
Membrane time constant (τ_{mem}) (ms)	32.4 ± 2.9 34.1 ± 4.0	35.9 ± 3.5 40.7 ± 4.4	37.5 ± 2.0 41.7 ± 3.3	35.3 ± 4.8 35.0 ± 5.6
R_{input} (MΩ)	92.8 ± 6.6 98.2 ± 5.8	117.0 ± 9.8 102.6 ± 11.3	99.9 ± 9.0 111.3 ± 20	126.1 ± 16.8 112.0 ± 14.5
V_{rest} (mV)	-81.6 ± 1.0 -82.6 ± 0.8	-83.3 ± 1.1 -83.6 ± 1.5	-85.1 ± 1.0 -81.3 ± 1.8	-82.0 ± 1.2 -75.0 ± 1.3
Spike threshold (mV)	-43.4 ± 1.5 -46.9 ± 1.3	-44.5 ± 1.2 -45.1 ± 1.0	-45.2 ± 1.0 -43.9 ± 1.2	-47.2 ± 1.1 -45.6 ± 1.5
Rheobase (pA)	248.6 ± 17.1 222.4 ± 17.9	19.4 ± 17.8 220.3 ± 15.9	244.7 ± 16.4 211.0 ± 21.7	205.0±29.9 227.4±28.8
Numeric values for L4-evoked spiking (Panel 2F)				

Num. evoked spikes (mean ± SEM)	0.41 ± 0.3 0.27 ± 0.2	1.46 ± 0.6 0.23 ± 0.2	0.23 ± 0.2 1.67 ± 0.9	0.53 ± 0.2 2.20 ± 1.5
Mann-Whitney test	p=0.94	p=0.09	p=0.22	p=0.64
% of cells with L4-evoked spiking	2/17 (11.8%) 2/11 (18.2%)	6/13 (46.1%) 2/13 (15.4%)	2/13 (15.4%) 6/18 (33.3%)	7/19 (36.8%) 2/10 (20.0%)
Fisher's exact test	p=0.99	p=0.20	p=0.41	p=0.43

Table S3. Cellular properties of L2/3 PYR neurons for Figure 2D-F experiments. Related to Figure 2.

	Fmr1 +/y	*Fmr1 -/y*	*Cntnap2 +/+*	*Cntnap2 -/-*	*16p11.2 +/+*	*16p11.2 del/+*
L2/3 recordings, anesthetized mice (Figures 5 & 6)						
Total mice	11	9	7	9	12	6
Age (Mean±SEM)	69.2±1.1	65.5±1.3	64.4±1.3	61.2±1.4	52.2±0.6	48.8±1.1
L2/3 FS units, anesthetized mice (Figure 5)						
Total FS units	17	32	18	25	30	19
Spontaneous firing Units (mice)	17 (6)	32 (8)	18 (7)	25 (9)	30 (10)	19 (5)
VRC[1] Units (mice)	17 (6)	32 (8)	17 (6)	25 (9)	30 (10)	19 (5)
L2/3 RS units, anesthetized mice (Figure 6)						
Total RS Units	49	86	35	39	85	32
Spontaneous firing Units (mice)	49 (11)	86 (9)	35 (7)	39 (9)	85 (12)	32 (6)
VRC[1] Units (mice)	48 (10)	86 (9)	31 (6)	39 (9)	80 (11)	32 (6)
Best whisker firing[2] Units (mice)	31 (8)	75 (7)	29 (5)	24 (7)	75 (10)	32 (6)
Jitter, CW tuning, tuning sharpness[3] Units (mice)	19 (10)	46 (8)	9 (6)	15 (6)	38 (9)	19 (6)
Correlations and synchrony[4]. Pairs (units, mice)	95 (42,7)	303 (82,8)	44 (30,7)	62 (32,6)	290 (78,10)	46 (28,5)
L4 RS units, anesthetized mice (Figure S6)						
Total mice	8	5	8	9	9	6
Total RS units	32	23	41	28	37	26
Spontaneous firing Units (mice)	32 (8)	23 (5)	41 (8)	28 (9)	37 (9)	26 (6)
VRC[1] Units (mice)	32 (8)	23 (5)	39 (7)	28 (9)	37 (9)	26 (6)

1 Velocity response curve (VRC) was quantified for all units for which the VRC stimulus protocol was applied to the unit's columnar whisker.

2 Best whisker (BW)-evoked firing rate was quantified for all units whose columnar whisker was at the center of the 3x3 piezo array. This criterion ensures the greatest accuracy for identifying the BW.

3 Jitter, columnar whisker (CW) tuning, and tuning sharpness were quantified for all whisker-responsive units.

4 Signal and noise correlations and firing synchrony were calculated across all pairs of simultaneously recorded L2/3 RS units located < 0.2 mm apart.

Table S4. Sample sizes and ages for *in vivo* anesthetized experiments. Related to Figures 5 and 6.

Chapter 4

Reduced multi-whisker responses in *Fmr1 KO* mice reflect reduced spiking to single columnar whisker deflections

Tomer Langberg and Daniel E. Feldman

4.1 Summary

It is commonly believed that Fragile X Syndrome is caused by reduced synaptic inhibition that leads to increased spiking in cortex. However, while inhibition is reduced in S1 of the *Fmr1 KO* mouse, excitatory neurons show reduced spiking to single whisker deflections. We investigated whether excess spiking occurs instead in response to deflections of multi-whisker sequences, which drive more spiking than single whisker deflections and may engage excitatory and inhibitory circuitry differently. We discovered that spiking was reduced in response to both whisker sequences and single whisker deflections. Deficits to multi-whisker tuning may simply reflect reduced responsiveness to the anatomically corresponding columnar whisker and increased tuning heterogeneity within each cortical column.

4.2 Introduction

Hyperarousal to sensory stimuli and increased seizure comorbidity in Fragile X Syndrome (FXS) suggest that neural circuits in FXS are hyperexcitable (Lewine et al., 1999, Gilllberg & Billstedt, 2000, Hagerman et al., 2017, Hagerman & Stafstrom, 2009). Inhibition is weak in sensory cortex of *Fragile X Mental Retardation 1* (*Fmr1*) *KO* mice (Gibson et al., 2008, Goel et al., 2018, Antoine et al., 2019), which parallels findings in several additional genetic mouse models of autism spectrum behaviors (Wallace et al., 2012, Banerjee et al., 2016, Antoine et al., 2019, Chen et al., 2020). This supports the hypothesis that loss of feedforward inhibition increases sensory-evoked firing of excitatory neurons in FXS. However, we recently discovered that excitatory neurons in

S1 of *Fmr1 KO* mice spike less than in wildtype mice in response to sparse activation of cortex by single whisker deflections (Antoine et al., 2019). This suggests that inhibition may not be required to stabilize firing to single whisker deflections as it does during dense activation (Pouille et al., 2009, Moore et al., 2018).

Multi-whisker sequences drive more spiking in S1 than single-whisker deflections (Laboy-Juarez et al., 2019), and may resemble denser activation of S1 during natural whisking (Sachdev et al., 2001). Sharpened tuning of single neurons to specific whisker-sequences likely involves temporal patterns of synaptic excitation and inhibition that are not engaged during single whisker deflections (Higley & Contreras, 2005, Laboy-Juarez et al., 2019). We hypothesized that excitatory neurons in S1 of awake *Fmr1* KO mice express sensory tuning abnormalities or spiking hyperexcitability in response to dense stimulation with whisker sequences. We found that spiking to whisker sequences was reduced in *Fmr1 KO* mice. We observed modest reductions to both suppression and facilitation of responses to specific sequences, which might reflect previously observed reductions to synaptic inhibition and excitation (Antoine et al., 2019). However, the dominant effect of excitability and sensory tuning to multi-whisker sequences primarily reflects reduced responsiveness to single deflections of the anatomically-corresponding "columnar-whisker" (CW).

4.3 Results

We tested for abnormal spiking in S1 of awake adult male *Fmr1 KO* mice as compared to *FVB* controls in response to deflections of single whiskers and whisker sequences. We recorded single units using laminar polytrodes in layers 2-5 of functionally identified "barrel" columns while interleaving deflections of a 3 x 3 array of whiskers centered on the CW (Figure 1A-C). Stimuli comprising either single whisker deflections, deflections of 2 whiskers in sequence ($\Delta t = 0, \pm 40$ ms interstimulus interval), or blanks (no deflection), occurred every 300 ms during each 10 s trial. Mice performed a head-fixed visually-cued classical conditioning task which ensured they were awake, but did not require attention to whisker stimuli (Figure 1B,D). In total, 268 units were recorded in 2 *FVB* and 2 *Fmr1 KO* mice across 16 recordings (3-5 recordings on separate days per mouse). The following analyses comprise only regular-spiking, putative excitatory units in L2/3 that were statistically-responsive to single whisker deflections (See methods).

For each unit, we measured a spatial receptive field based on single-whisker deflections and identified a "Best Whisker" (BW) that evoked the most spikes. Single-whisker receptive fields for a representative example wildtype and mutant unit are shown in Figure 2, centered on each unit's CW. In both of these example units, the CW is also the BW as it evokes the most spiking, but the mutant neuron in Figure 2C,D is more broadly tuned across the array of whiskers than the wildtype neuron in Figure 2A,B. We also analyzed tuning for each unit to 2-whisker sequences. We calculated for each unit the mean response to each columnar whisker-surround whisker (CW-SW) combination at each Δt interval. Units were often tuned to a particular CW-SW combination at a particular Δt, confirming results from Laboy-Juarez et al., 2019. The Δt interval containing the maximal response was identified as the "best" Δt, and the CW-SW sequence evoking that maximal response was identified as the "optimal" sequence. Representative multi-whisker receptive fields for an *FVB* and a *Fmr1 KO* unit are shown in Figure 3. The example *FVB* unit in Figure 3A-B is sharply tuned to the D1-C2

sequence at its best Δt, and several of its suboptimal CW-SW sequences at its best Δt evoke responses less than CW-only deflections, indicating cross-whisker suppression.

We ranked each unit's single-whisker receptive field from the BW to the whisker that evoked the least spiking, and compared tuning between *Fmr1 KO* and *FVB* control units. *Fmr1 KO* units fired fewer spikes in response to single deflections of their BW compared to *FVB* controls (Figure 4A) and were more broadly tuned across their best 3 whiskers (n = 24 *FVB*, 28 *Fmr1 KO* units) (Figure 4B). Each column in S1 contains neurons tuned for the CW and other nearby whiskers (Clancy et al. 2015; LeMessurier et al. 2019), and we also analyzed tuning relative to the CW. Consistent with a more heterogeneous whisker map in *Fmr1 KO* mice (Arnett et al., 2014, Zhang et al. 2014, Juczewski et al. 2016, Antoine et al. 2019), *Fmr1 KO* units fired less to single CW deflections, were less often tuned to the CW, and more often had spiking responses to surround whiskers (SWs) that were significantly above baseline activity (Figure 4C-F). In contrast to weak responses to the CW, spike rates to single SW deflections were normal (Figure 4C). Responses to the BW, CW, and best SW are described in median peri-stimulus time histograms in Figure 4F. Thus, matching our earlier findings in anesthetized and awake mice (Antoine et al. 2019), *Fmr1 KO* units are hypo-excitable to single whisker deflections. This effect is driven by reduced spiking to single CW deflections.

We next asked whether hyperexcitability or altered tuning might arise in response to sequences of whisker deflections, which drive denser firing in S1 (Laboy-Juarez et al. 2019). Nearly all units in both genotypes fired more spikes in response to their optimal CW-SW sequence compared to their BW alone (Figure 5A), consistent with previous findings (Laboy-Juarez et al. 2019). Both the optimal CW-SW sequence response and the BW response were reduced in mutant compared to wildtype units (Figure 5A-B). In general, units that spiked more to a single CW deflection "gained" more spikes in response to their optimal CW-SW sequence, and there was no difference in the distribution of this gain between mutant and wildtype units (Figure 5B). For each unit, we identified which Δt interval contained the optimal CW-SW sequence that evoked the maximal response, and ranked all 8 CW-SW combinations at that best Δt (Figure 5C). This revealed reduced spiking to CW-SW sequences in *Fmr1 KO* units that predominantly reflected a negative "DC" shift compared to wildtype with no change in tuning sharpness (Figure 5C-F). Median multi-whisker tuning for *FVB* and *Fmr1 KO* populations is shown in Figure 5D, aligned to each unit's optimal sequence. Spiking to SW-SW sequences was normal (Figure 5G), suggesting a specific deficit to CW-containing sequences. Thus, reduced spiking to CW-SW sequences in Fmr1 KO mice parallels reduced spiking to CW-only deflections.

We next quantified aspects of multi-whisker tuning that may reflect cross-whisker suppression or amplification. Measured responses to each optimal and suboptimal CW-SW combination at each unit's best Δt were compared to a linear prediction formed from their component single whisker responses (Figure 6A-B). As reported previously in C57BL/6 mice (Laboy-Juarez et al. 2019), responses to each wildtype unit's optimal sequence was well-modelled by this linear prediction, while suboptimal stimuli typically evoked sublinear responses (Figure 6A-B). In both wildtype and KO units, optimal sequences evoked on average a more linear response than suboptimal stimuli (Figure 6C). This was not a trivial effect of optimal sequences evoking more spiking than

suboptimal, as shown by a shuffling procedure where measured responses and their corresponding linear predictions were shuffled across all units in each genotype (Figure 6D). Firing to optimal sequences was more sublinear in *Fmr1 KO* units, though the difference was not significant (Figure 6F; p=0.0754, permutation test).

We next examined median tuning plots for CW-SW sequences at each unit's best Δt, normalized to the optimal measured response (Figure 6E, left). This revealed that suboptimal CW-SW sequences evoked on average fewer spikes than the CW alone in wildtype units, a direct demonstration of cross-whisker suppression. This suppression appears absent in *KO* units (Figure 6E, right). Interestingly, both suppression of CW-evoked firing by suboptimal SWs, and sublinear firing by optimal stimuli, are indicative of units whose best whisker is not the CW (Laboy Juarez et al. 2019). We thus quantified how much each SW suppressed CW-evoked firing during sequences where the SW preceded the CW, and ranked each SW based on this cross-whisker suppression (Figure 7A). Maximal cross-whisker suppression was reduced in *Fmr1 KO* mice (Figure 7A-B). While this is consistent with reduced inhibition, it is strongly predicted by reduced firing to single CW deflections (Figure 7C).

4.4 Discussion

We tested for abnormal spiking responses to deflections of multi-whisker sequences in S1 of *Fmr1 KO* mice, which activate cortex more densely than single-whisker deflections. Spiking to sequences was reduced in *Fmr1 KO* mice, which also expressed reduced cross-whisker suppression of CW-evoked firing and a trend for more sublinear responses to optimal sequences. These multi-whisker phenomena in *Fmr1 KO* mice might be explained by their observed single-whisker tuning: (1) Both effects are indicative of units whose best single whisker is a surround whisker (Laboy-Juarez et al. 2019) and (2) Reduced cross-whisker suppression in *Fmr1 KO* units is well-explained by a "basement" effect due to reduced firing to single CW deflections (Figure 7C). Thus, the most parsimonious explanation for the multi-whisker sensory encoding deficits we have observed in S1 of *Fmr1 KO* units is reduced CW-evoked firing and more heterogeneous single-whisker tuning (Fewer units tuned to the CW).

We have now shown that genetic deletion of *Fmr1* causes reduced spiking in "sparse" (Chapter 4) and "dense" (Chapter 5) conditions, arguing strongly against the common notion of excess sensory-evoked firing in these mice. However, our experiments were conducted in head-fixed, stationary mice whose whiskers were deflected by calibrated piezo movements. This poorly models any natural behavior. Hyperexcitability may still occur during natural behavior, or during a tactile task that requires attending to whisker touch.

This study should promote a paradigm shift in our common hypotheses for neural circuit dysfunction in Fragile X Syndrome. Scientific attention has narrowly focused on reduced inhibition, or increased "excitation-to-inhibition ratio" in these *Fmr1 KO* mice because these mechanisms have intuitively related to increased spiking. Perhaps now scientific attention should focus on how general weakening at both excitatory and inhibitory synapses leads to weak and heterogeneous tuning, and how this may explain FXS phenotypes. Evidence for weak or broader tuning of single neurons and blurred population tuning in whisker S1 of *Fmr1 KO* mice is now strong (Arnett et al., 2014, Zhang et al., 2014, Juczewski et al., 2016, Antoine et al., 2019). Broader tuning has

also been found in V1, but firing rates were otherwise normal (Goel et al. 2018). Broader tuning has also been reported in auditory cortex of *Fmr1 KO* mice (Rotschafer and Razak, 2013). Interestingly, in Rotschafer and Razak, 2013, evoked spiking within 50 ms after a 10 ms auditory stimulus onset was normal, but spiking was increased 50-200 ms after the stimulus onset. This might suggest stable feedforward excitation, but hyperexcitable recurrent circuitry that sustains excess activity late after the onset of sensory stimuli. A careful analysis of excitability of recurrent circuits in S1 of the *Fmr1 KO* mice will be important. In contrast to our findings, increased sensory-evoked spiking has been shown in the hindpaw region of S1 (Zhang et al., 2014). Together, these studies suggest that while the genetic effect on firing rate may be dependent on cortical region, the effect on tuning is largely pervasive. Further investigations into the neural circuit mechanisms underlying map blurring and broad or heterogeneous tuning (eg., Bureau et al. 2008) will be insightful.

Sensory maps in cortex are plastic (LeMessurier & Feldman, 2018). Environmental enrichment has been shown to strengthen tuning of S1 populations towards their anatomically corresponding columnar whisker (LeMessurier et al. 2019). If pathology of Fragile X Syndrome is rooted in weak or blurred sensory maps, then similar developmental interventions that strengthen these maps may be therapeutically beneficial.

Note: Final experiments were cut short due to COVID-19 but will continue in the lab.

4.5 Methods

FXS model mice and corresponding wildtypes were obtained from Jackson Labs ($Fmr1^{+/y}$: #004828, $Fmr1^{-/y}$: #004624. Mice were group-housed and weaned at postnatal day (P) 21. Experimental methods were as in the awake recording methods of Laboy-Juarez et al., 2019, unless noted otherwise, and are described below.

Surgery and Behavioral Training

During adulthood, mice were switched to single-housing and were implanted with a lightweight chronic head-post and intrinsic signal imaging was performed to locate the C1, C2, D1, and D2 whisker columns. After imaging, the skull over S1 was covered with dental cement, and further fortified with a cover slip. After 1 week when mice recovered to normal pre-surgical weight and looked otherwise healthy, they began water regulation and trained operantly to lick for water reward while head-fixed on the behavioral rig. Behavioral training took place daily, and general behavior, weight, and water consumption were monitored carefully to ensure mouse health. Mice were typically at 85% of their pre- water regulation weight during training and recording. At the start of each behavioral session, mice were transiently anesthetized with 1.5% isoflurane, head-fixed, and whiskers were placed in a 3x3 piezoelectric actuator array positioned 2.5 mm from the whisker pad, centered on the C1, C2, D1, or D2 whiskers. Isoflurane was then halted.

Each behavioral trial consisted of a 10 second period of whisker stimulation, during which a new whisker stimulus was presented every 300 ms (33 stimuli per trial). Each stimulus comprised either a deflection of a single whisker, a deflection of a 2 whisker sequence (0, +40, or -40 inter-deflection interval), or a blank stimulus (no deflection) used to quantify spontaneous firing rate. Deflection waveforms are as described in Laboy-Juarez et al., 2019. In brief, each waveform was rostrocaudal, triphasic, 40 ms in duration, and 160 µm in peak amplitude (caudal direction). In a fraction of trials (30-50%), a blue light was flashed after the 10 s whisker stimulation epoch to reveal the 2 second reward window during which a mouse could lick for water reward. Licks were detected by infrared beam break. The fraction of Go trials was adjusted to maximize the number of trials performed. Mice were alert, did not visibly whisk, and licked only occasionally outside Go trial response windows.

After several weeks of training, mice typically performed the behavior with >80% lick rate on Go trials and close to 0% spontaneous licking. The mouse was then anesthetized with 1.5% isoflurane, the dental cement over S1 drilled away, the skull thinned, and intrinsic signal imaging performed again for the C1, C2, D1, and D2 columns.

Extracellular Recordings

The next day, the mouse returned to the training rig for a neural recording. Just prior to recording, the mouse was put under light isoflurane anesthesia, the cranial window covered in a saline bath, and a small craniotomy (<500 µm) was performed over an identified whisker column (C1, C2, D1, or D2), chosen based on the quality of the imaging result and to minimize obstruction of the penetration site by the vasculature. A ground electrode was connected to the saline bath. A 3 x 3 array of whiskers were attached with rubber cement to piezos centered on the whisker corresponding to the targeted cortical column. A laminar polytrode (NeuroNexus A1x16-Poly2-5mm-50s-177-A16) was micromanipulated to the brain surface. The electrode was manipulated 50-100 µm over a ~5 minute period while the brain surface was examined for dimpling. If there was dimpling, the electrode was removed, a duratomy carefully performed, and the electrode reinserted to a depth of 50-100 µm. The saline covering the cranial window was then sealed with a layer of Kwik-Cast sealant to prevent evaporation and to stabilize the electrode in position, and the isoflurane anesthesia was removed. The electrode was then further manipulated into the targeted column in S1 to a radial depth of 640 µm over a 20-30 minute period, during which the mouse would wake and begin to perform the classical conditioning task. During this time, single whisker stimuli were played and evoked spiking was examined live to confirm correct targeting of the cortical column. The electrode typically rested at its final depth for 15 minutes before the aforementioned behavioral trials and recording began. After the recording, the electrode was removed over a 15 minute period, the mouse was returned to 1.5% isoflurane anesthesia, the saline suctioned out, the ground electrode removed, and the exposed brain and thinned skull was resealed with a thin layer of Kwik-Cast sealant, which was then fortified with a cover slip. The mouse then returned for a repeat craniotomy and recording in a new whisker column (C1, C2, D1, or D2) each successive day. Mice

underwent 3-5 recordings on separate days. On rare occasions, the same column was recorded in twice in the same mouse over these recording days.

Voltage signals were digitized (24.4144 kHz) and stored using a TDT RZ5D system. Spikes were isolated by off-line band-pass filtering (0.3-6 kHz) and common average referenced using custom Matlab code. Spikes were collected using a template-matching procedure as described in Laboy-Juarez et al. 2019. Units were clustered using the semi-automated UltraMegaSort 2000 software. Layer boundaries were defined by micromanipulator depth as such (Layer (L) 4-5 boundary: 588 µm, L3-4: 413 µm, L1-2: 100 µm). In total, 268 units were recorded across 2 *FVB* and 2 *Fmr1 KO* mice. Trough-to-peak times of the total recorded population showed a clear bimodal distribution. Regular-spiking, putative excitatory neurons and fast-spiking units amongst the total population of recorded cells were readily separable using a 0.475 ms trough-to-peak time cut-off.

Data Analysis

Stimuli within ±200 ms of a lick were excluded to avoid contamination by lick-related movements and lick-related spiking. Data were analyzed from recordings whose L4 multi-unit tuning clearly matched the target whisker column, defined as mean spiking -1 sem evoked by the center whisker in the piezo array being >1 sem more than any other whisker +1 sem.

1 mouse was excluded from analysis due to an obvious brain deformity.

All analysis was performed using custom Matlab functions, and was performed only on regular-spiking units in L2/3. Spiking responses for single-whisker and multi-whisker stimuli were quantified as the average number of spikes within 125 ms after each stimulus onset, except in calculations of cross-whisker suppression (Figure 7) where an 85 ms window after CW-deflection onset was used. Units that showed statistically significant responses to single deflections of any of the 9 whiskers were classified as whisker-responsive. To determine statistical significance of a response, we computed the probability that a Poisson process with that unit's mean spontaneous firing would generate the number of spikes measured after whisker deflection using a binless method. We used $p = 0.001/9 = 1.11e\text{-}4$ as threshold for significance. For both single-whisker and multi-whisker receptive fields, tuning sharpness was calculated as the best response divided by the sum of the best 3 responses. Permutation tests were performed to determine statistically-significant comparisons ($p<0.05$) in all firing rate comparisons. Comparisons of linearity and tuning width used a 2-tailed t-test.

4.6 Figures

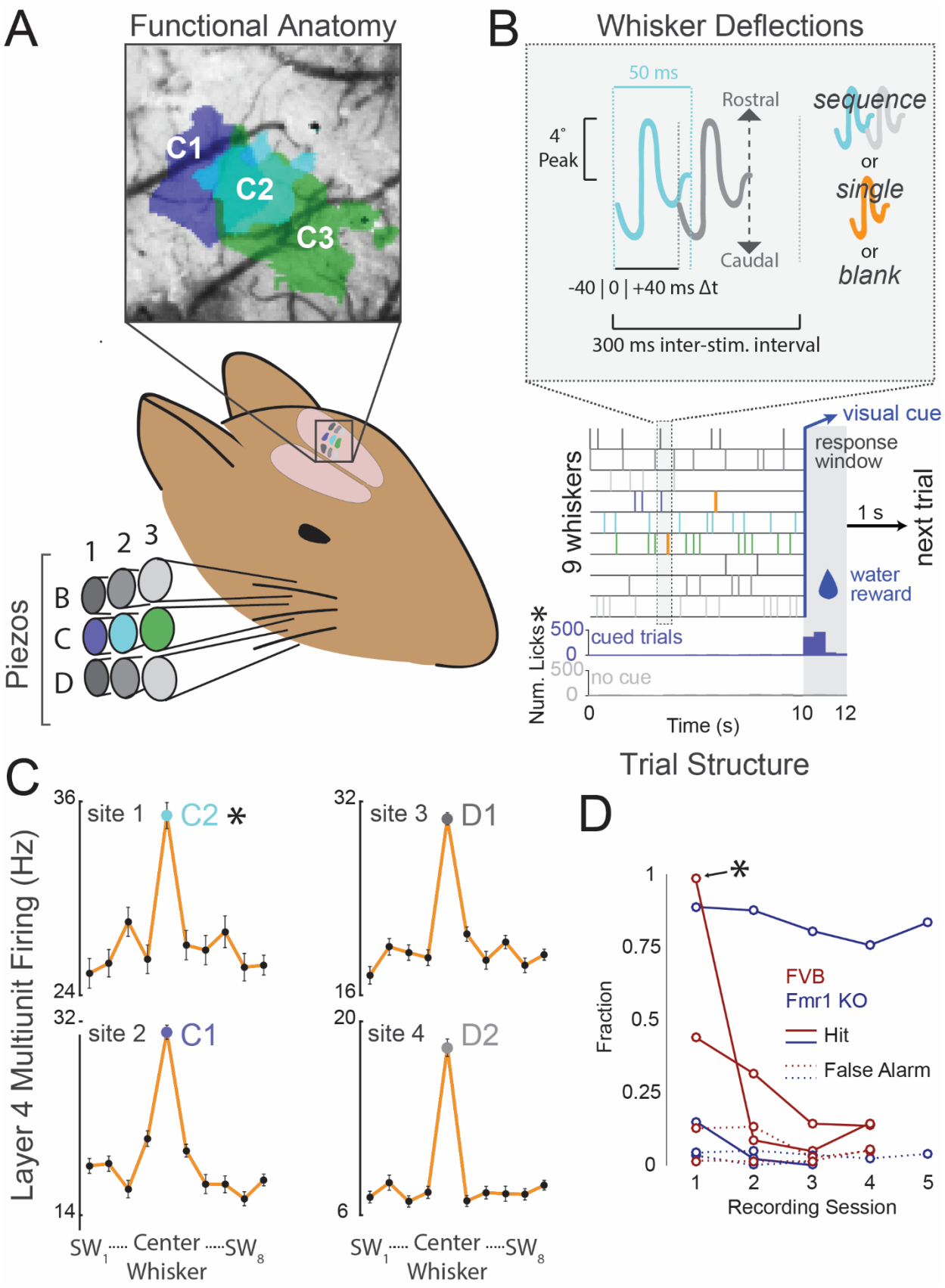
A
Functional Anatomy
C1
C2
C3
Piezos
1 2 3
B
C
D
B
Whisker Deflections
50 ms
Rostral
Caudal
4°
Peak
-40 | 0 | +40 ms Δt
300 ms inter-stim. interval
sequence
or
single
or
blank
visual cue
response window
1 s
next trial
9 whiskers
water reward
Num. Licks
500
0
cued trials
500
0
no cue
0
10
12
Time (s)
Trial Structure
C
Layer 4 Multiunit Firing (Hz)
36
site 1
C2 *
24
32
site 2
C1
14
SW1 ..... Center SW8
Whisker
32
site 3
D1
16
20
site 4
D2
6
SW1 ..... Center SW8
Whisker
D
1
0.75
0.5
0.25
0
Fraction
FVB
Fmr1 KO
Hit
False Alarm
1 2 3 4 5
Recording Session

Figure 1. Experimental Procedure. (A) Intrinsic signal imaging results for an example mouse with example piezo array. (B) Top: Amplified details of each individual stimulus, zoomed in from bottom. Bottom: Schematic of the trial structure with behavioral results from an example recording. Asterisk indicates where this exact recording presents in (C,D). (C) Example multi-unit tuning from layer 4 across 4 separate recording sites from 1 mouse. Values are mean ±sem. (D) Behavior summary for each recording day from each of the 4 mice in this study.

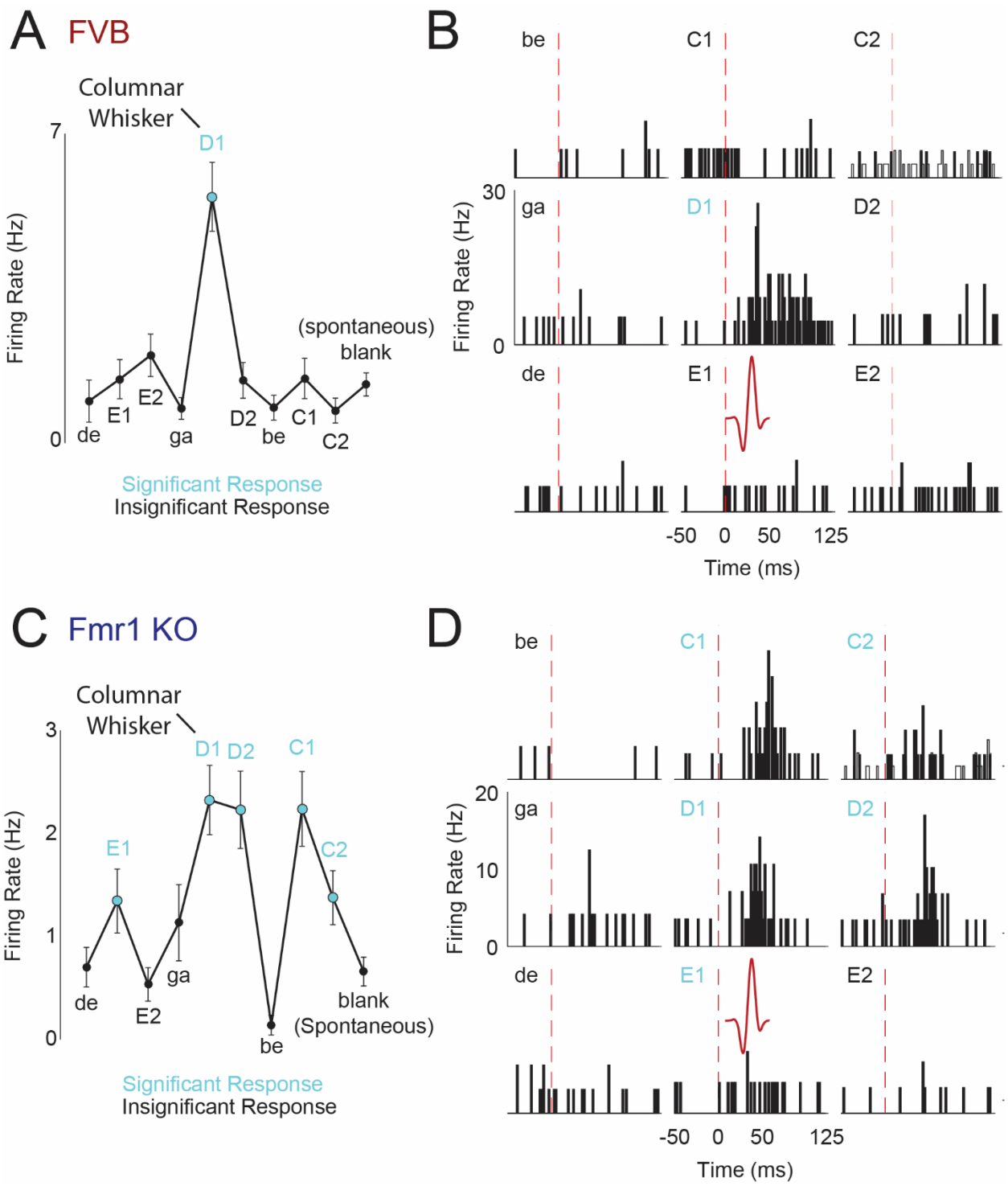

Figure 2. Example single-whisker receptive fields. (A) Example single whisker receptive field from an *FVB* unit. Light blue labels represent stimuli that evoked a significant response. Values are mean±sem. Whisker identities are written near each corresponding value. (B) Peri-stimulus time histograms for the example unit

in (A) Red waveform indicates the waveform delivered by each piezo. Dashed red line indicates onset of stimulus. (C-D) same as (A-B) but for an *Fmr1 KO* unit.

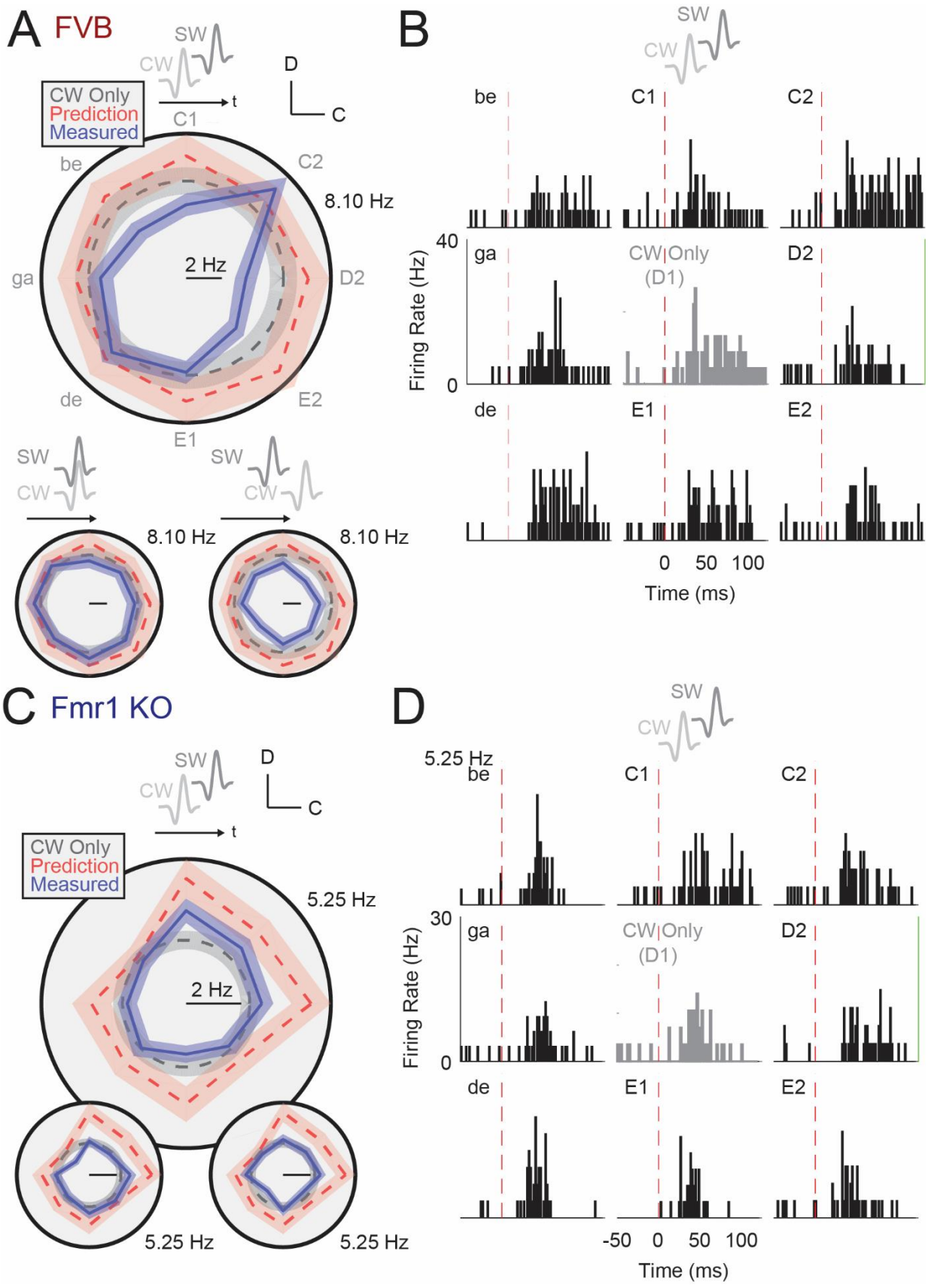
A FVB
SW
CW
t
D
C
CW Only
Prediction
Measured
C1
be
C2
8.10 Hz
ga
2 Hz
D2
de
E2
E1
SW
CW
SW
CW
8.10 Hz
8.10 Hz
B
SW
CW
be
C1
C2
40
ga
CW Only
(D1)
D2
Firing Rate (Hz)
0
de
E1
E2
0
50
100
Time (ms)
C Fmr1 KO
SW
CW
D
C
t
CW Only
Prediction
Measured
5.25 Hz
2 Hz
5.25 Hz
5.25 Hz
D
SW
CW
5.25 Hz
be
C1
C2
30
ga
CW Only
(D1)
D2
Firing Rate (Hz)
0
de
E1
E2
-50
0
50
100
Time (ms)

Figure 3. Example multi-whisker receptive fields. (A-B) Multi-whisker tuning for the example *FVB* unit shown in Figure 2A-B. (A) Polar plot of Mean multi-whisker receptive field for an example *FVB* unit. Blue line indicates mean measured response, red dashed line indicates mean linear prediction, and grey dashed line indicates the mean CW-only response. Shaded regions indicate mean±sem. Top: mean multi-whisker receptive field for this *FVB* unit at its best Δt (CW precedes SW by 40 ms). Corresponding SW identities are listed in grey at each polar position, and correspond to the positions of the SW identities in (B). Bottom: mean multi-whisker receptive fields at the other Δt's for the same unit. Bottom Left: SW and CW deflection are simultaneous. Bottom Right: SW deflection precedes CW. Scale bar value for Top corresponds also to scales in bottom plots. Value outside of circles indicates scale of the circle radius. (B) Peri-stimulus time histograms for the stimuli and unit shown in (A). SW identity is listed in each histogram. Center, grey histogram shows response to a single CW deflection. (C-D) Same as (A-B) except for the same example *Fmr1 KO* unit shown in Figure 2C-D.

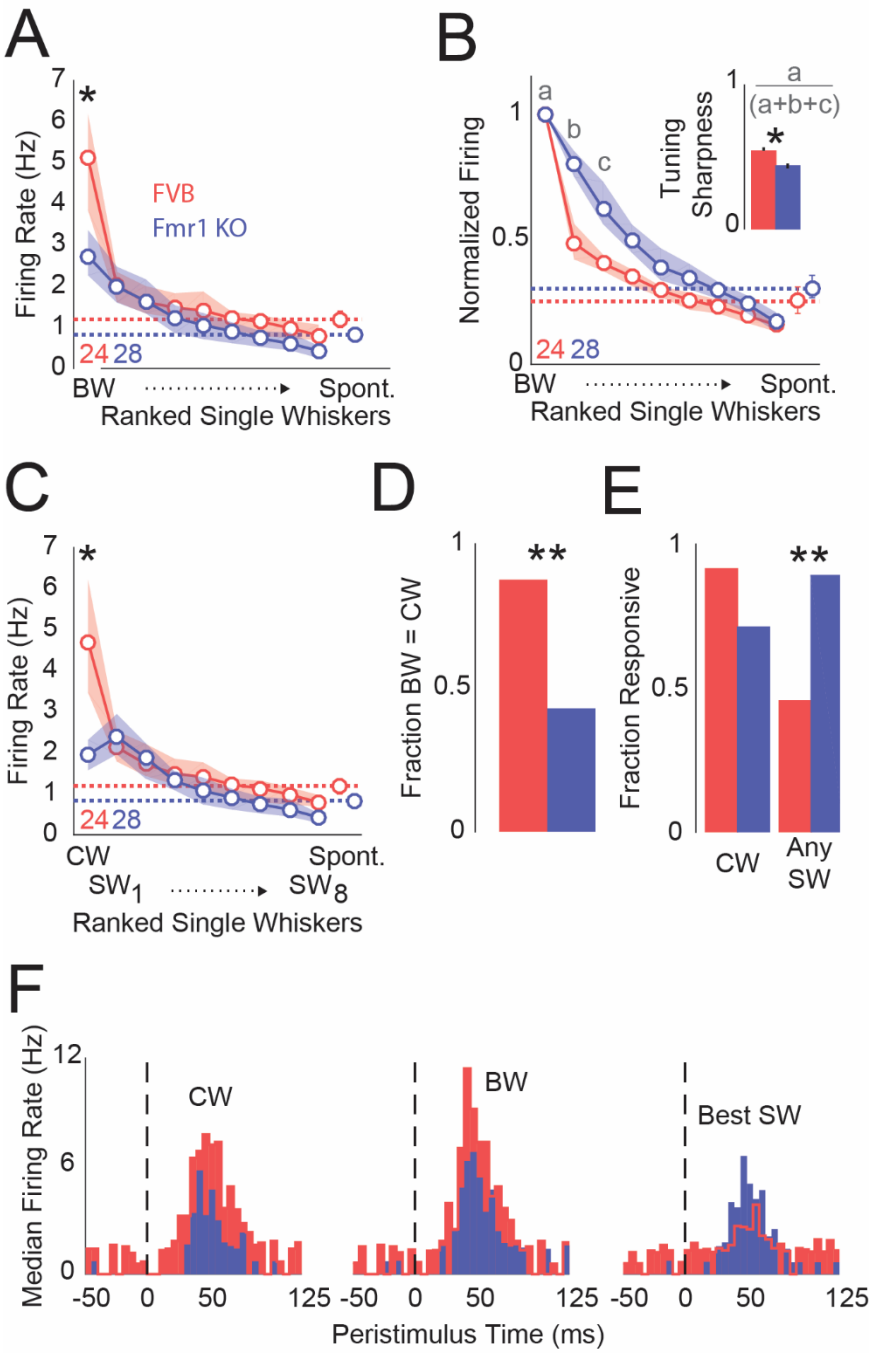

Figure 4. Reduced firing to single CW and BW deflections in *Fmr1 KO* units. (A-F) Red represents *FVB* units, Blue represents *Fmr1 KO* units. (A) Single whisker receptive fields for *FVB* and *Fmr1 KO* units. Whiskers are ranked from the best whisker to the whisker evoking the least spiking, following by spontaneous epochs (blanks). (B) Single-whisker receptive fields normalized to each unit's best whisker. Inset: Mean Tuning sharpness, calculated as the best whisker response divided by the sum of the responses to the best 3 whiskers. Error bars are sem. (A-C) Values indicate bootstrapped medians. Shaded regions are nonparametric 68% confidence intervals. (D) Fraction of units whose best whisker is the columnar

whisker (E) Fraction of units statistically responsive to the CW or to any SW. (F) Mean peristimulus time histograms to single whisker stimuli. Left: CW deflections. Middle: BW deflections. Right: Deflections of the Best SW. Dashed line indicates stimulus onset. * p<0.05 permutation test. ** p< 0.05 chi2 test.

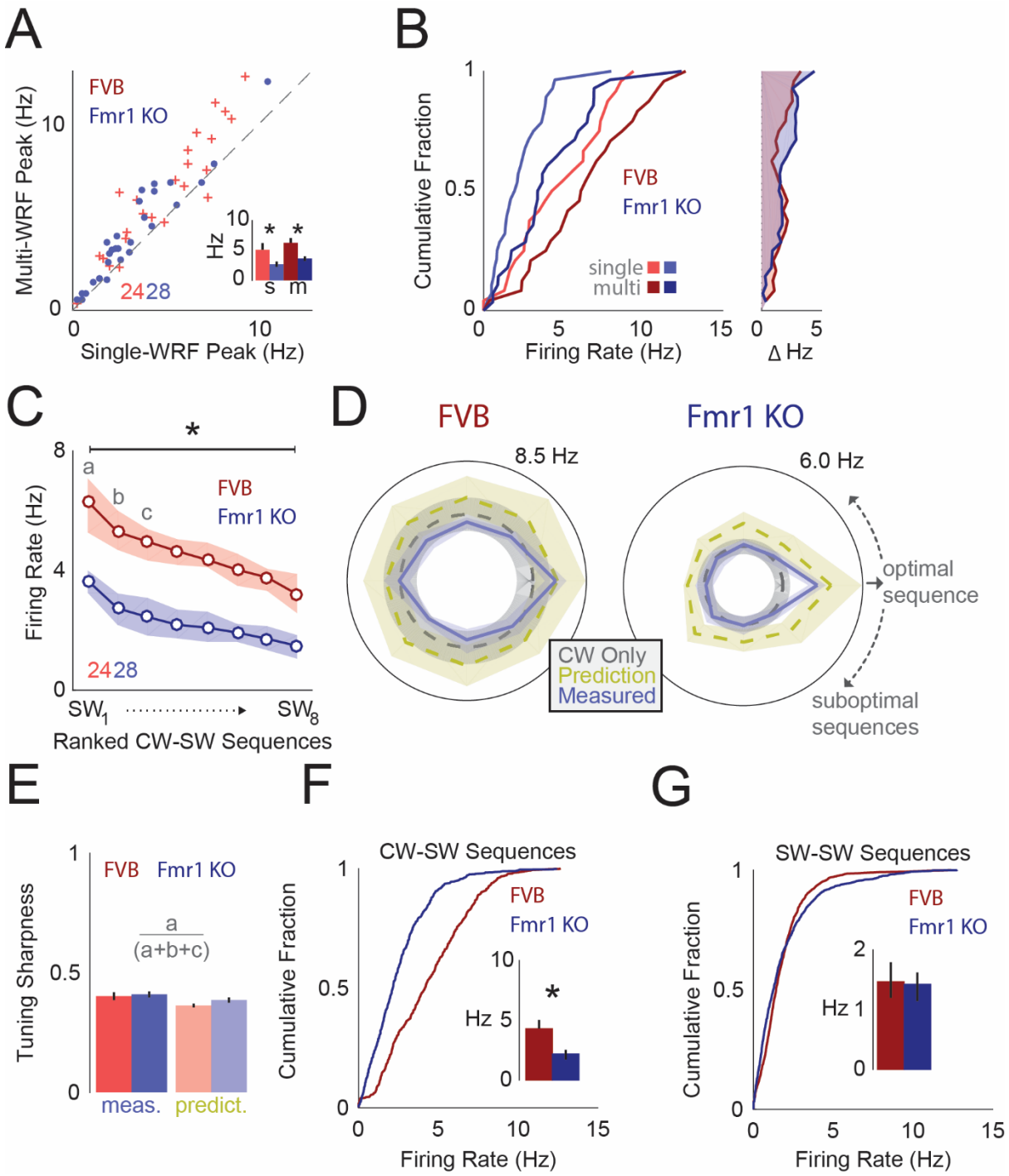

Figure 5. Reduced firing to CW-SW sequences in *Fmr1 KO* units. (A-C,E-G) Red represents *FVB* units. Blue represents *Fmr1 KO* units. (A) Single-WRF Peak

(BW response) plotted against the multi-WRF peak (optimal CW-SW sequence response). Numbers indicate sample sizes. Inset shows bootstrapped median responses to single (s) or multi (m) whisker receptive field peaks with nonparametric 68% confidence intervals. (B) Left: Cumulative fraction of CW-only evoked responses (light colors) and optimal CW-SW combination (dark colors). Right: Difference in firing rate between each unit's CW-only and optimal CW-SW sequence response, ordered by the unit's CW responses in the left plot. (C) Bootstrapped median multi-whisker receptive field at each unit's best Δt, ranked by firing rate from the optimal CW-SW sequence (SW1) to the sequence evoking the least spiking (SW8). Shaded region indicates nonparametric 68% confidence interval. * p<0.05, permutation test for integrated receptive field. (D). Polar plots for population receptive fields for *FVB* (left) and *Fmr1 KO* (Right) units. Lines indicate bootstrapped medians, shaded regions indicate nonparametric 68% confidence intervals. Each unit's receptive field is rotated so that the optimal sequence points to the right. Grey dashed lines indicate CW-only responses, yellow dashed lines indicate linear predictions, and blue solid line indicates measured responses. Values indicate scale of each circle's radius. (E) Mean Tuning sharpness±sem, calculated as the optimal sequence response divided by the sum of the responses to the best 3 sequences. (F) Cumulative distribution of each unit's mean response to all CW-SW sequences at all Δt's. Inset: Bootstrapped median values with 68% nonparametric confidence intervals. * p<0.05, permutation test. (G) Same as (F) but for all SW-SW combinations.

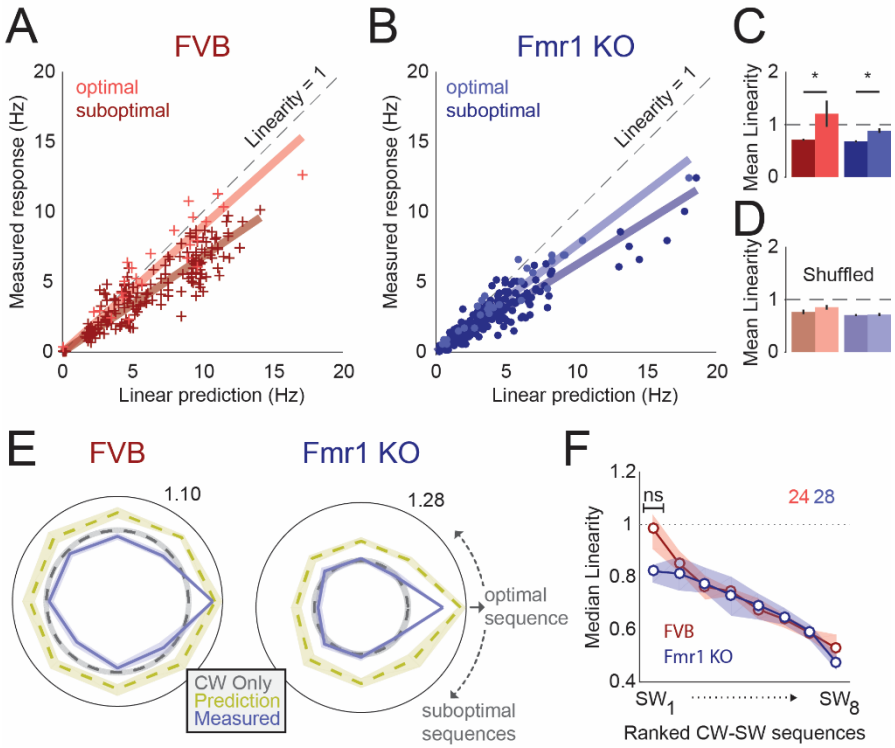

Figure 6. Trend for reduced linearity to optimal stimuli in Fmr1 KO units. (A-D, F) Red represents *FVB* units, Blue represents *Fmr1 KO* units. (A-B) Measured response plotted against linear prediction for each sequence at each unit's best Δt. Lighter color represents optimal stimuli, darker color represents suboptimal stimuli. Shaded line indicates corresponding linear fits. Left: *FVB* units. Right: *Fmr1 KO* units. (C) Linearity of measured responses to optimal and suboptimal stimuli. (D) Linearity of measured responses to optimal and suboptimal stimuli from shuffled data. (C-D) Lighter shade represents optimal stimulus response, darker shade is response to suboptimal stimuli. Bars indicate means. Error lines indicate standard error. (E) Polar plots for population multi-whisker tuning at each unit's best Δt, normalized to the optimal sequence response. Each unit's receptive field is rotated so that the optimal sequence points to the right. Lines represent bootstrapped medians, shaded regions represent nonparametric 68% confidence intervals. Blue line is measured response, grey dashed line is the CW-only response, and yellow dashed line is the linear prediction. (F) Linearity of each CW-SW combination at the best Δt, ranked from the optimal sequence (SW1) to the sequence evoking the least spikes (SW8). Values indicate bootstrapped medians, shaded regions are nonparametric 68% confidence intervals. 'ns', not significant (p=0.0754, permutation test).

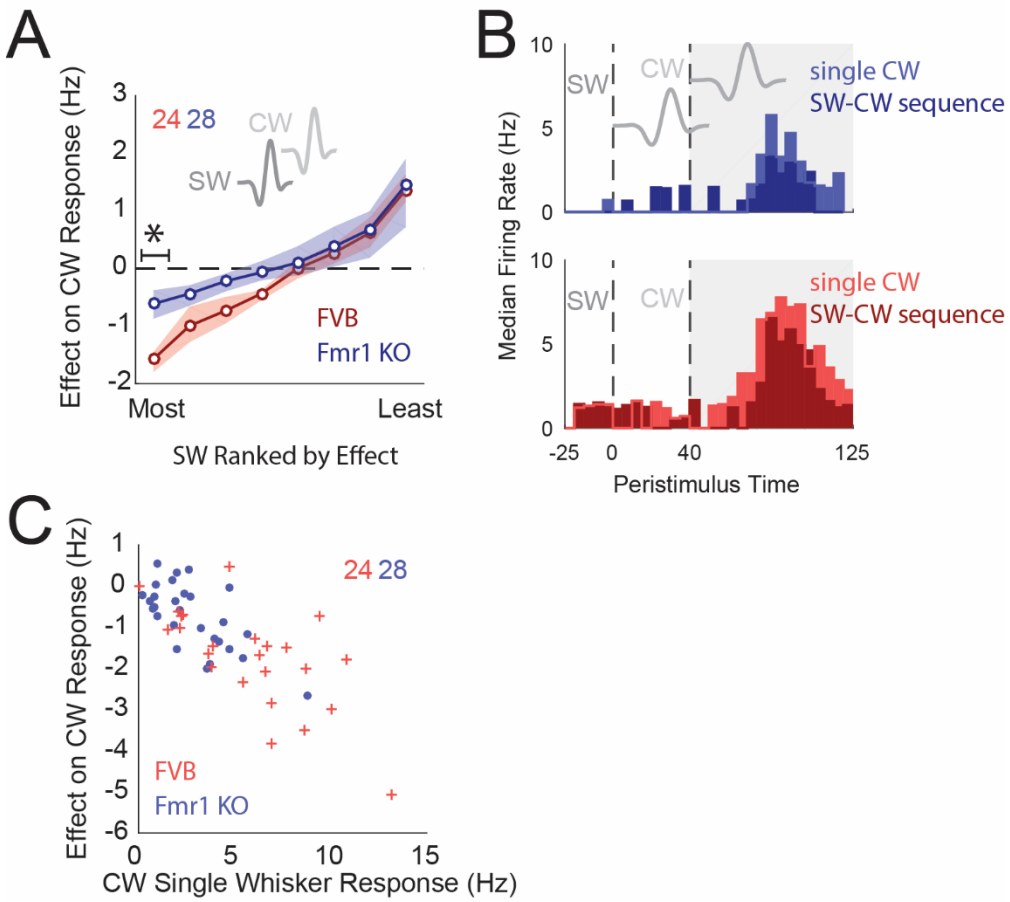

Figure 7. Reduced cross-whisker suppression in *Fmr1 KO* units. (A-C) Red represents *FVB* units, Blue represents *Fmr1 KO* units. (A) Effect of SW deflection on response to CW deflection in sequences where the SW precedes the CW. Values are ranked by most suppression evoked to least suppression/most amplification evoked. *p<0.05, permutation test at SW evoking the most suppression. (B) Median peristimulus-time histograms for each unit's response to its CW-SW sequence expressing maximal suppression (Left-most points in A). Dashed lines indicate onset of SW and CW deflections. Grey shaded region indicates the window where spikes were analyzed. Light bars indicate responses to single CW deflections, dark bars indicate responses to the SW-CW combinations. Top: *Fmr1 KO* units, Bottom: *FVB* units. (C) Correlation between the response to a single CW deflection, and the maximal suppression of this CW response when preceded by the SW in sequence (response to CW deflection in sequence minus the single CW deflection response). Each point is a unit.

4.7 References

Antoine, M. W., Langberg, T., Schnepel, P., & Feldman, D. E. (2019). Increased excitation-inhibition ratio stabilizes synapse and circuit excitability in four autism mouse models. *Neuron*, *101*(4), 648-661.

Arnett, M. T., Herman, D. H., & McGee, A. W. (2014). Deficits in tactile learning in a mouse model of fragile X syndrome. *PloS one*, *9*(10).

Banerjee, A., Rikhye, R. V., Breton-Provencher, V., Tang, X., Li, C., Li, K., ... & Sur, M. (2016). Jointly reduced inhibition and excitation underlies circuit-wide changes in cortical processing in Rett syndrome. *Proceedings of the National Academy of Sciences*, *113*(46), E7287-E7296.

Bureau, I., Shepherd, G. M., & Svoboda, K. (2008). Circuit and plasticity defects in the developing somatosensory cortex of FMR1 knock-out mice. *Journal of Neuroscience*, *28*(20), 5178-5188.

Chen, Q., Deister, C. A., Gao, X., Guo, B., Lynn-Jones, T., Chen, N., ... & Feng, S. (2020). Dysfunction of cortical GABAergic neurons leads to sensory hyper-reactivity in a Shank3 mouse model of ASD. *Nature Neuroscience*, 1-13.

Clancy, K. B., Schnepel, P., Rao, A. T., & Feldman, D. E. (2015). Structure of a single whisker representation in layer 2 of mouse somatosensory cortex. *Journal of Neuroscience*, *35*(9), 3946-3958.

Gibson, J. R., Bartley, A. F., Hays, S. A., & Huber, K. M. (2008). Imbalance of neocortical excitation and inhibition and altered UP states reflect network hyperexcitability in the mouse model of fragile X syndrome. *Journal of neurophysiology*, *100*(5), 2615-2626.

Gillberg and, C., & Billstedt, E. (2000). Autism and Asperger syndrome: coexistence with other clinical disorders. *Acta Psychiatrica Scandinavica*, *102*(5), 321-330.

Goel, A., Cantu, D. A., Guilfoyle, J., Chaudhari, G. R., Newadkar, A., Todisco, B., ... & Erickson, C. A. (2018). Impaired perceptual learning in a mouse model of Fragile X syndrome is mediated by parvalbumin neuron dysfunction and is reversible. *Nature neuroscience*, *21*(10), 1404-1411.

Hagerman, P. J., & Stafstrom, C. E. (2009). Origins of epilepsy in fragile X syndrome. *Epilepsy Currents*, *9*(4), 108-112.

Hagerman, R. J., Berry-Kravis, E., Hazlett, H. C., Bailey, D. B., Moine, H., Kooy, R. F., ... & Hagerman, P. J. (2017). Fragile X syndrome. *Nature reviews Disease primers*, *3*(1), 1-19.

Higley, M. J., & Contreras, D. (2005). Integration of synaptic responses to neighboring whiskers in rat barrel cortex in vivo. *Journal of neurophysiology*, *93*(4), 1920-1934.

Juczewski, K., von Richthofen, H., Bagni, C., Celikel, T., Fisone, G., & Krieger, P. (2016). Somatosensory map expansion and altered processing of tactile inputs in a mouse model of fragile X syndrome. *Neurobiology of disease*, *96*, 201-215.

Laboy-Juárez, K. J., Langberg, T., Ahn, S., & Feldman, D. E. (2019). Elementary motion sequence detectors in whisker somatosensory cortex. *Nature neuroscience*, *22*(9), 1438-1449.

LeMessurier, A. M., & Feldman, D. E. (2018). Plasticity of population coding in primary sensory cortex. *Current opinion in neurobiology*, *53*, 50-56.

LeMessurier, A. M., Laboy-Juarez, K. J., McClain, K., Chen, S., Nguyen, T., & Feldman, D. E. (2019). Enrichment drives emergence of functional columns and improves sensory coding in the whisker map in L2/3 of mouse S1. *eLife*, *8*.

Lewine, J. D., Andrews, R., Chez, M., Patil, A. A., Devinsky, O., Smith, M., ... & Chong, B. (1999). Magnetoencephalographic patterns of epileptiform activity in children with regressive autism spectrum disorders. *Pediatrics*, *104*(3), 405-418.

Moore, A. K., Weible, A. P., Balmer, T. S., Trussell, L. O., & Wehr, M. (2018). Rapid rebalancing of excitation and inhibition by cortical circuitry. *Neuron*, *97*(6), 1341-1355.

NS Sachdev, Heike Sellien, Ford Ebner, R. (2001). Temporal organization of multi-whisker contact in rats. *Somatosensory & motor research*, *18*(2), 91-100.

Pouille, F., Marin-Burgin, A., Adesnik, H., Atallah, B. V., & Scanziani, M. (2009). Input normalization by global feedforward inhibition expands cortical dynamic range. *Nature neuroscience*, *12*(12), 1577.

Wallace, M.L., Burette, A.C., Weinberg, R.J., and Philpot, B.D. (2012). Maternal loss of Ube3a produces an excitatory/inhibitory imbalance through neuron type-specific synaptic defects. Neuron 74, 793–800.

Zhang, Y., Bonnan, A., Bony, G., Ferezou, I., Pietropaolo, S., Ginger, M., ... & Frick, A. (2014). Dendritic channelopathies contribute to neocortical and sensory hyperexcitability in Fmr1−/y mice. *Nature neuroscience*, *17*(12), 1701-1709.

Chapter 5

Conclusion

Tomer Langberg

This thesis deconstructs the classic hypothesis that genetic mutations cause Fragile X Syndrome (FXS) and Autism Spectrum Disorders (ASDs) by reducing synaptic inhibition in cortex. This reduced inhibition is theorized to cause increased spiking, which disrupts normal processing and causes hyperexcitability phenotypes such as seizures and heightened sensory arousal. Testing this hypothesis begins with an understanding of how excitatory and inhibitory synapses are wired in cortical circuit motifs (Chapter 1). In Chapter 2, we warmed up with a discussion of how different inhibitory neuron subtypes are engaged by patterns of synaptic inputs. In Chapter 3, we formally tested the synaptic "excitation-to-inhibition ratio hypothesis" across distinct mouse models of ASDs, ultimately concluding that while inhibition is weak in these models, spiking is normal or reduced. In Chapter 4, we tested for hyperexcitability in the *Fmr1 KO* mouse model of FXS under an additional set of sensory conditions, and concluded that their primary phenotype is weak and blurred sensory maps.

Sensory systems are clearly disrupted in the *Fmr1 KO* mouse, just not necessarily in a consistent way across brain regions and sensory modalities. *In vitro* measurements of synaptic activity and intrinsic excitability show many abnormalities (Contractor et al., 2015), but translating these results to a physiological or behavioral phenotype *in vivo* has not been successful. On one side, there is weak evidence for increased spiking in S1 (Zhang et al. 2014), while heightened neural responses are more evident in the auditory system from brainstem (Garcia-Pino et al., 2017, Rotschafer et al., 2015) to cortex (Rotschafer & Razak, 2013). On the other hand, spike rate was observed to be normal in visual cortex (Goel et al., 2018) and reduced in whisker S1 (Antoine et al., 2019, Chapter 4 of this thesis). When considering studies from other mouse models of autism spectrum behaviors, results become even more variable. While scientifically attractive, there may be no consistent phenotype across

different circuits. Sensory abnormalities in these human conditions are, anyhow, known to be heterogeneous, and there is no canonical or essential sensory dysfunction that is agreed upon across human ASD cases (Rogers & Ozonoff, 2005).

So far, studies on sensory-evoked responses in cortex of the *Fmr1 KO* mouse can be rudimentally summarized by weaker sensory tuning and blurred sensory maps (Zhang et al., 2014, Arnett et al., 2014, Rotschafer & Razak, 2013, Juczewski et al., 2016, Goel et al., 2018, Antoine et al., 2019, Chapter 4 of this thesis). To make progress on a neural circuit mechanism, we must begin to bridge this theme with known non-sensory phenotypes, such as seizures. Seizure comorbidity is common in FXS and ASDs, and mechanisms that underlie seizure initiation and propagation (de Curtis & Avoli, 2015) might have many effects on sensory encoding. How might weak or blurred sensory maps relate to seizure mechanisms? Answering this question may provide a necessary paradigm shift in the field. Perhaps diffuse connectivity (Bureau et al. 2008) helps to propagate seizures, but also disrupt sensory maps and cognitive functions.

The ultimate evidence for a difference in cortical excitability in these mouse strains will be from recordings in freely- moving and behaving mice. Neural activity and behavior regulate each other bidirectionally. Restricted experimental conditions (e.g., head fixing, single-housing, artificial sensory stimuli) sever this feedback, absolve the richness of natural behavior, and likely obscure real phenotypes. Perhaps it is the case that increased spiking does occur in these mouse models, as compared to wildtypes during matched volitional behavioral states. Changes to firing in mouse models of neurodevelopmental disorders might, however, be inextricably linked to differences in free behavior. Increased spiking may occur only during abnormal hyperactivity, such as excessive sensory exploration or running. Deciphering the developmental feedback between free behavior and neural activity will be critical to answering whether the genetic mutations implicated in FXS and ASDs cause neurons to spike more

References

Arnett, M. T., Herman, D. H., & McGee, A. W. (2014). Deficits in tactile learning in a mouse model of fragile X syndrome. *PloS one*, *9*(10).

Bureau, I., Shepherd, G. M., & Svoboda, K. (2008). Circuit and plasticity defects in the developing somatosensory cortex of FMR1 knock-out mice. *Journal of Neuroscience*, *28*(20), 5178-5188.

de Curtis, M., & Avoli, M. (2015). Initiation, propagation, and termination of partial (focal) seizures. *Cold Spring Harbor perspectives in medicine*, *5*(7), a022368.

Contractor, A., Klyachko, V. A., & Portera-Cailliau, C. (2015). Altered neuronal and circuit excitability in fragile X syndrome. *Neuron*, *87*(4), 699-715.

Garcia-Pino, E., Gessele, N., & Koch, U. (2017). Enhanced excitatory connectivity and disturbed sound processing in the auditory brainstem of fragile X mice. *Journal of Neuroscience*, *37*(31), 7403-7419.

Goel, A., Cantu, D. A., Guilfoyle, J., Chaudhari, G. R., Newadkar, A., Todisco, B., ... & Erickson, C. A. (2018). Impaired perceptual learning in a mouse model of Fragile X syndrome is mediated by parvalbumin neuron dysfunction and is reversible. *Nature neuroscience*, *21*(10), 1404-1411.

Juczewski, K., von Richthofen, H., Bagni, C., Celikel, T., Fisone, G., & Krieger, P. (2016). Somatosensory map expansion and altered processing of tactile inputs in a mouse model of fragile X syndrome. *Neurobiology of disease*, *96*, 201-215.

Rogers, S. J., & Ozonoff, S. (2005). Annotation: What do we know about sensory dysfunction in autism? A critical review of the empirical evidence. *Journal of Child Psychology and Psychiatry*, *46*(12), 1255-1268.

Rotschafer, S., & Razak, K. (2013). Altered auditory processing in a mouse model of fragile X syndrome. *Brain research*, *1506*, 12-24.

Zhang, Y., Bonnan, A., Bony, G., Ferezou, I., Pietropaolo, S., Ginger, M., ... & Frick, A. (2014). Dendritic channelopathies contribute to neocortical and sensory hyperexcitability in Fmr1−/y mice. *Nature neuroscience*, *17*(12), 1701-1709.